Microscopic modeling of multiferroic bulk systems, thin films and nanostructures

D i s s e r t a t i o n

zur Erlangung des akademischen Grades

Doctor rerum naturalium (Dr. rer. nat.)

vorgelegt von

Master of Science (Festkörperphysik)

Safa Golrokh Bahoosh

geboren am 13.06.1983 in Sabzevar-Iran

angefertigt am

Institut für Physik

Naturwissenschaftliche Fakultät II

Martin-Luther-Universität Halle-Wittenberg

Halle (Saale), den 02.Juli 2013

1. Gutachter: Prof. Dr. Steffen Trimper
2. Gutachter: Prof. Dr. Ingrid Mertig
3. Gutachter: Prof. Dr. Johannes Richter

Abgabe der Dissertation: 02. Juli 2013
Öffentliche Verteidigung: 12. December 2013

This thesis is dedicated to
my mother, who taught me to be patient,
my father, who encouraged me in my endeavors,
and
Julia, who gave me more confidence in my own ability.

Contents

List of abbreviations and symbols

BTO	barium titanate
STO	strontium titanate
KDP	potassium dihydrogen phosphate
PTO	lead titanate
BNMO	Bi_2NiMnO_6
LNO	Lithium niobate
KTO	Potassium tantalate
Fe	iron
Ga	gallium
Co	cobalt
Zn	zink
Mg	Magnesium
TIM	Ising model in a transverse field
RPA	random phase approximation
MFA	mean field approximation
CM	commensurate
ICM	incommensurate
XRD	X-ray diffraction
DFT	density functional theory
DMI	Dzyaloshinskii-Moriya interaction
ME	magnetoelectric
MEC	magnetoelectric coupling
FE	ferroelectric
FM	ferromagnetic
AFM	antiferromagnetic
M	magnetization
P	polarization
Ω	transverse field
NP	nanoparticle
NN	nearest neighbor
NNN	next nearest neighbor

List of Figures

1. Introduction

Multiferroics, defined as materials with at least two coexisting ferroic orders like ferroelectric, ferroelastic, ferromagnetic and ferrotoriodic orders, have recently attracted enormous research activities [1, 2]. In most cases, the term multiferroic refers to the materials that display cross-correlations between magnetic and electric properties. In particular, the coexistence of (anti)ferroelectricity and (anti)ferromagnetism in a single phase is of interest for memory and logic device applications. Hence, both magnetization and polarization can independently encode information in a single multiferroic bit. Moreover, the magnetic order can be triggered by an applied electric field while ferroelectric order is changed by an external magnetic field. The appearance of ferroelectric and magnetic properties in a single phase poses a challenge for a theoretical description because one has to include the coupling between the corresponding order parameters or their microscopic counterparts, respectively.

In such systems, long-range magnetic order takes place as a result of interactions between magnetic moments in the crystal lattice where ferroelectricity is commonly originated from a structural change of the underlying lattice itself and/or the interaction of electric dipole moments. In fact, ferroelectricity occurs due to a lack of inversion symmetry within the crystal structure. Ferroelectric materials are characterized by a spontaneous polarization that can be reversed or reoriented by applying an electric field, and a ferromagnet has a spontaneous and switchable magnetization. The spontaneous polarization and magnetization are the order parameters which become nonzero when the material is cooled below the related phase transition temperatures. In narrower sense, the magnetoelectric effect is the phenomenon inducing magnetization (polarization) by applying an external electric (magnetic) field.

Impressive sign of the interest in the multiferroic and magnetoelectric field of research has been observed in the online database ISI Web of knowledge [3] by the rapid increase in publications as depicted in Fig. 1.1.

In spite of the great progress in studying multiferroic materials experimentally, there is a current debate on adequate theoretical descriptions. The illustration of magnetism, ferroelectricity and their coupling using many body approaches and quantum or classical statistical analysis are promising ways in understanding the macroscopic properties such as the temperature-dependent order parameters based on the microscopic behavior included in the elementary excitations and their damping.

Although ab-initio approaches have significantly contributed to the recent progress in this area, the applicability is limited to the zero temperature behavior and hence to the ground state properties. The method of thermodynamic Green's function is an appropriate analytical tool to study complex many body systems at finite temperature. This method allows us to find the dispersion relation of the elementary excitations of the underlying quantum model, and moreover the temperature-dependent macroscopic quantities like magnetization and polarization. Notably, the poles of the
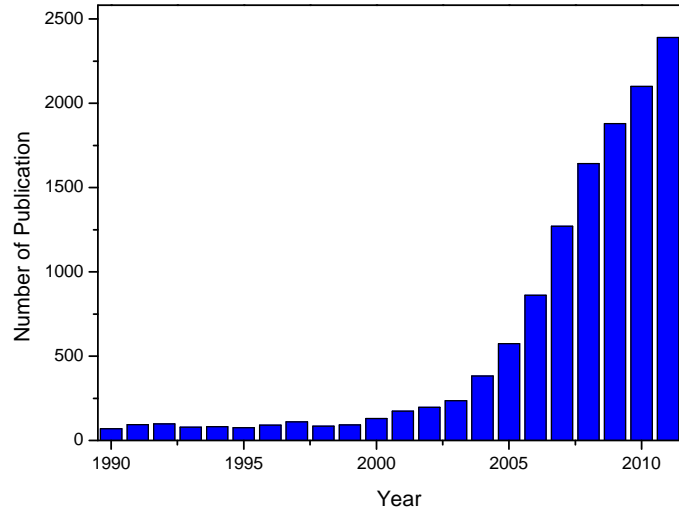
Figure 1.1. – Publications per year indexed in the ISI Web of knowledge database with 'Multiferroic' and 'Magnetoelectric' as a keyword [3] from 1990-2012.

Green's function are identified with the spectrum of the excitations.

Since ferromagnetism and ferroelectricity in reduced dimensions provide a drastic increase of the storage density of random access memories (RAM), nanoscale materials have attracted extensive attentions. The anticipated benefit depends on whether the phase transition and the polarized low temperature state still exist when the system is scaled down up to less than 100 nm. The challenge in low dimensional finite structures concerns the synthesis, the experimental characterization of their size-dependent properties as well as the theoretical description. In regard to this, multiferroicity at the nanoscale emerged as a vital research field. In such multifunctional materials, the manner in which the properties scale with the structure size as well as the coupling behavior with size reduction, are especially considerable for any potential application and their theoretical studies are of high importance. The main objective of the present thesis is the theoretical description of multiferroic materials by emphasizing the different mechanism in bulk systems compared to thin films and nanostructures. This thesis consists of three main parts. The first part is dealing with the introduction of fundamental concepts of ferroelectricity, magnetism, and their coupling in multiferroic materials. In addition, the method of Green's function will be presented as a basis for the subsequent chapters.

The second part describes the multiferroicity in bulk materials. The Hamiltonian of a typical system consists of two subsystems that are coupled to each other through a coupling term which can be determined based on symmetry arguments. The classes of models studied are the Heisenberg model and the Ising model in a transverse field under inclusion of anharmonic lattice interactions. Based on quantum models we are interested in the statistical and thermodynamic behavior of multiferroic systems. Using the Green's function technique, the dispersion relation of the elementary excitation of the underlying quantum model, their damping and moreover,

the temperature-dependent macroscopic quantities such as magnetization and polarization, will be calculated. Especially, the influence of spin-phonon interaction, the single-ion anisotropy and the ion doping effect as well as external magnetic and electric fields on the spin-wave dispersion relation and the related phonon modes are studied in detail.

In the third part, the behavior of nanosized multiferroic systems is analyzed. In particular, we explain the origin of multiferroicity in those materials which do not show this property at their bulk state. The final chapter of the thesis contains the summary of the current work as well as outlooks.

2. Basics

2.1. Ferroelectricity

The ferroelectric effect was discovered in 1920 by Joseph Valasek, who obtained hysteresis curves for Rochelle salt analogous to the hysteresis curves of ferromagnetism [4]. In March 1935 potassium dihydrogen phosphate (KDP), KH_2PO_4 was found to be ferroelectric with a critical temperature of about 123 K by Busch and Scherrer [5] where its isomorphs also contains the properties of ferroelectricity. The first phenomenological theory was proposed in 1940 by Müller to describe the relations between piezoelectric, anomalous dielectric and elastic behaviors of Rochelle salt [6–9]. In 1941, Slater introduced the first significant microscopic theory of phase transitions based on the model of hydrogen bonds to explain the behavior of KH_2PO_4 [10]. After 1941, the third major ferroelectric substance, barium titanate $BaTiO_3$, was discovered [11]. Barium titanate was the first man-made perovskite ferroelectric material in ceramic form. In the following years several isomorphs of $BaTiO_3$ were found to behave also as ferroelectrics. In 1949, Devonshire published a theory on the phase transition mechanism of $BaTiO_3$ [12]. His theory has deepened the understanding on the behavior of $BaTiO_3$ and has initiated the thermodynamic theory in ferroelectricity. A major breakthrough in the study of ferroelectricity came from Cochran [13] and Anderson [14] via the soft modes description of ferroelectricity in the perovskite. The development of the ferroelectric soft mode theory occupied the duration from 1959 to 1970. From 1980 until now, many ferroelectrics have been discovered and research activity has rapidly increased.

Typically, materials demonstrate ferroelectricity below the Curie temperature, T_C, and are paraelectric above this phase transition temperature. Ferroelectric (FE) materials are characterized by a reversible spontaneous macroscopic polarization which is the electric dipole moment per unit volume. By applying an external electric field the direction of the polarization can be reversed.

The most prominent features of ferroelectric properties are hysteresis and nonlinearity in the relation between the polarization P and the applied electric field E. Dielectric materials exhibit a linear relationship between polarization and electric field. On the other hand, paraelectric materials, show a more enhanced non-linear dependence. In this case, the slope of the polarization curve which represents the electric permittivity is not constant as in dielectrics but is a function of the external electric field. These features are shown in Fig. 2.1. In addition to the switchable polarization, these materials exhibit other functional properties, including piezoelectricity, pyroelectricity, and non-linear dielectric behavior. Due to the unique combination of these properties researchers and engineers have been focusing on ferroelectric materials application in electronic devices such as sensors, infrared detectors, microwave phase filters and,
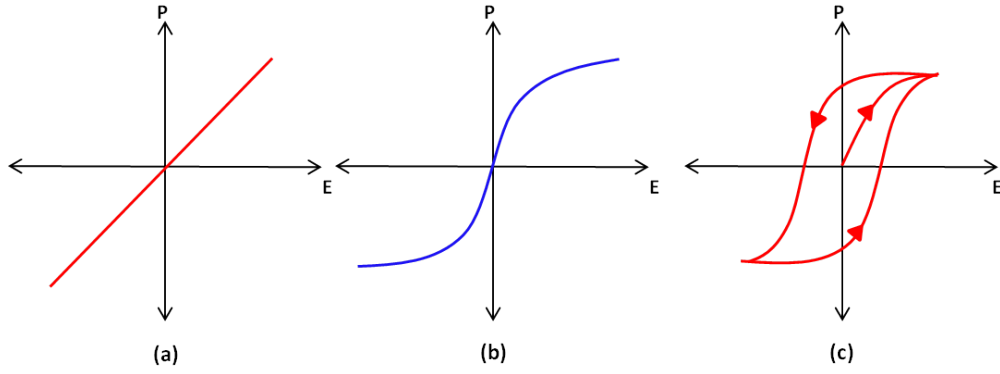
Figure 2.1. – Schematic hysteresis loop of the electric field dependency of the (a) Dielectric polarization, (b) Paraelectric polarization, (c) Ferroelectric polarization.

ultimately, non-volatile memories [15].

2.1.1. Ferroelectric materials and their properties

Ferroelectric crystals often show several transition temperatures and domain structure hysteresis, as much as ferromagnetic crystals. The phase transition of ferroelectrics is generally a structural phase transition which involves the displacement of ions so that crystals or crystallites exhibiting ferroelectric phenomena must be non-centrosymmetric. By performing the symmetry operations, crystals can be classified into 32 point groups. Among these 32 point groups, 11 of them possess a center of symmetry, and the remaining 21 are non-centrosymmetric. 20 of these 21 point groups are piezoelectric crystal classes. It is discovered that only 10 out of the 20 piezoelectric crystal classes have a unique polar axis and exhibit spontaneous polarization. One can conclude that all ferroelectric crystals are piezoelectrics, but the opposite is not true.

Above the Curie temperature, T_C the system is in its centrosymmetric paraelectric phase. As the temperature decreases, the material undergoes either a first or a second order phase transition and becomes ferroelectric. The spontaneous polarization is the order parameter of ferroelectric materials which appears below the transition temperature. The most important feature of first order phase transition is that the order parameter jumps discontinuously to zero at T_C. In case of a second order transition, the polarization exhibits a continuous change from one phase to another one. Fig. 2.2 shows typical cases of the variation of spontaneous polarization with temperature for the first and second order phase transition at zero field.

When the temperature is in the vicinity of the Curie point, the ferroelectric materials show anomalies in the dielectric, elastic, thermal and other thermodynamic properties [16] and is accompanied with changes in the shape of the crystal unit cell [17]. For example, the dielectric constant in most ferroelectric crystals has an abnormally large value (up to $104 \sim 105$) near T_C [18]. This phenomenon is usually called dielectric anomaly and is considered to be the basic feature of ferroelectric materials. Fig. 2.3 schematically shows the temperature variation of the dielectric constant of $BaTiO_3$. The Curie temperature for $BaTiO_3$ is 393.15 K. The nature of the paraelectric-
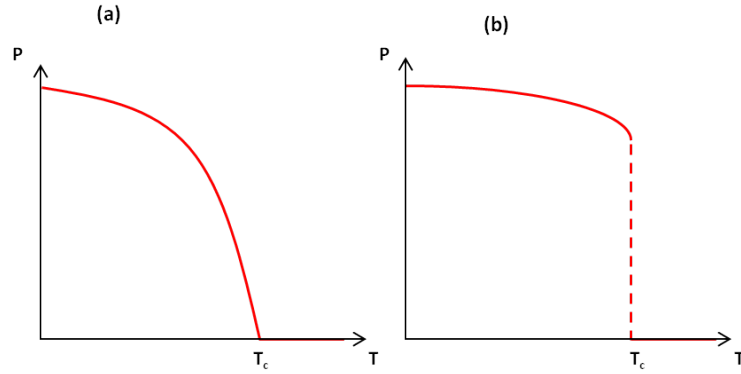
Figure 2.2. – The change of spontaneous polarization, P with temperature T for (a) Second order and (b) First order phase transition.
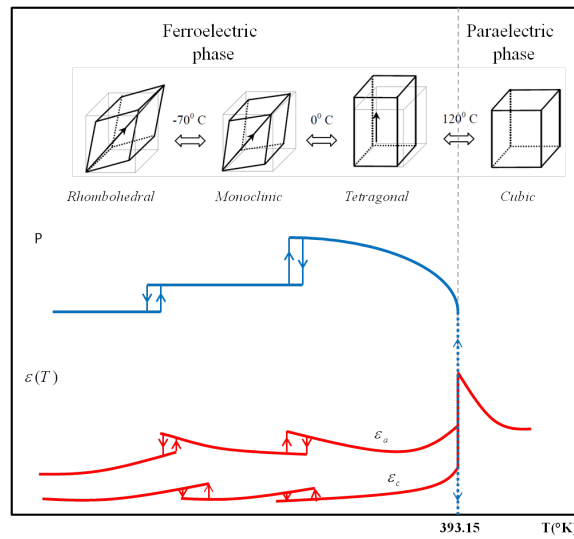
Figure 2.3. – The spontaneous polarization and dielectric constant $\varepsilon(T)$ of BaTiO$_3$ crystal. ε_c is the dielectric constant along the polar axis and ε_a is perpendicular to the axis. Adapted from [19, 20].

ferroelectric transition and whether the polarization at $T < T_C$ develops continuously or discontinuously is well explained based on Landau-Devonshire Theory. Further information can be found in related text books [16, 21].

2.1.2. Different type of ferroelectrics

Ferroelectrics can be divided into two main groups, displacive and order-disorder ones according to the phenomenological behavior of the crystals. This way of classifying ferroelectric materials is discussed in details by Lines and Glass [16]. Displacive ferroelectrics exhibits the polarization due to the ionic displacements of certain atoms in the crystal lattice which leads to a change in crystal symmetry. The most typical displacive ferroelectric is perovskite type, with a general chemical formula ABX$_3$. This structure is adopted by many oxides as ABO$_3$. A perovskite has a cubic crystal structure in a high-temperature phase. 'A' site cation occupies the cubic corner po-

sitions, 'B' atoms reside at the body center, while oxygen atoms are located at the face centers. The whole structure is formed by linking the vertices of the oxygen octahedral. The cavities are mainly occupied by the 'A' atoms. The oxygen octahedron has three four-fold axes, four three-fold axes and six two-fold axes. The polarization occurs when 'B' is displaced from the cubic center along any of these symmetry axes. For example, $SrTiO_3$ undergoes a displacive phase transition where the TiO_6 octahedra make a small rotation about [001] axis. Similarly, in $CaTiO_3$ and $MgSiO_3$, the octahedra tilt by different amounts about all three axes. Another type of displacive phase transition is seen in $PbTiO_3$. In paraelectric phase, Pb, O and Ti atoms occupy corners, face centered and body centered sites of cubic, respectively. At room temperature, the tetragonal crystal structure has the ionic displacement which is parallel in the polar phase of the oxygen octahedral during para-ferro phase transition [22]. During the phase transition, the oxygen atoms and Ti^{4+} cations in $PbTiO_3$ shift in the same direction relative to the Pb^{2+} cations. Pb atoms possess larger size compared to Ti atoms in the octahedral interstitial position, so Ti ions have small range of stability. Thus, the minimum energy can only be reached if Ti ion position is off-centered in surrounding of six oxygen ions as illustrated in Fig. 2.4. The random position of Ti ion in one of these six possible minimum energy sites will result in the spontaneous polarization.
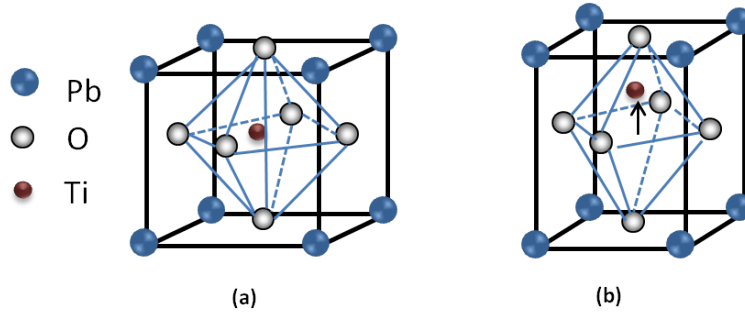
Figure 2.4. – Perovskite structure $PbTiO_3$ (a) in its centrosymmetric phase and (b) its possible ferroelectric phase.

In comparison with the displacive one, the mechanism of the order-disorder ferroelectrics is more complex. The prototype order-disorder class of ferroelectrics includes crystals in which the spontaneous polarization results from the ordering of the ion's proton in the structure. There are two major groups of order-disorder ferroelectrics. The first one consists of elements, such as phosphates, sulphates, cyanides, where the spontaneous polarization appears as a result of the ordering of protons in the hydrogen bonds. They are known as hydrogen-bonded ferroelectrics. The second group consists of tartrates, potassium nitrate, sodium nitrate, where spontaneous polarization is caused by the arbitrary ordering of radicals, which takes place from hindered rotation.

The typical examples of order-disorder ferroelectrics are sodium nitrite $NaNO_2$, triglicine sulphate (TGS) $(CH_2NH_2COOH)_3 \cdot H_2SO_4$ and potassium dihydrogen phosphate KH_2PO_4 (KDP). KDP is tetragonal above 124 K with a non-centrosymmetric space group $1\bar{4}2d$. Below 124 K it is in orthorhombic ferroelectric phase with space

group Fdd2 . The crystal structure consists of K^+ ions and tetrahedral PO_4^{3-} groups. The P^{5+} ions are located at the centers of these tetrahedral groups. The key part of the crystal structure is the three dimensional network of PO_4^{3-} groups linked by the O-H...O hydrogen bonds to the adjacent PO_4^{3-} group. Two upper atoms of one PO_4^{3-} tetrahedron are joined to the lower oxygen atoms of two other tetrahedrons, while two lower oxygen atoms of the tetrahedron are joined to the upper oxygen atoms of another two tetrahedrons [16, 20, 23]. The schematic representation of KDP is shown in Fig. 2.5. The ordering of the protons on the hydrogen bonds in the KDP does not
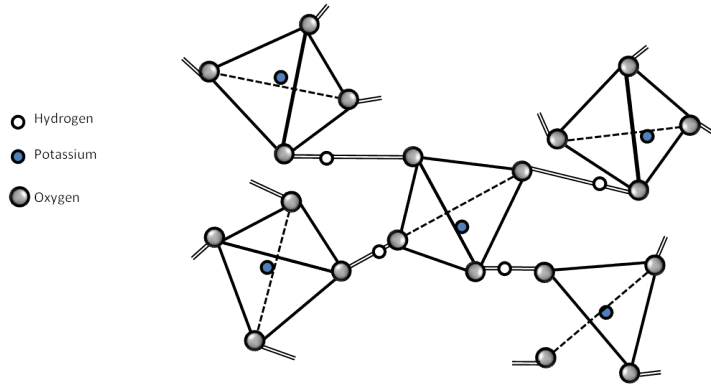
Figure 2.5. – Schematic diagram of the hydrogen bond system in KH_2PO_4 (KDP) crystals. The PO_4^{3-} groups with hydrogen bonds link to the nearest PO_4^{3-} groups adapted from [24].

directly contribute to the spontaneous polarization of the crystal, but the interaction of protons with K^+ and P^{5+} ions causes the displacement of the K^+ and P^{5+} ions that induces the spontaneous polarization.

Although two limiting cases of ferroelectric materials are introduced, it is not always easy to draw a line between them. In 1963 de Gennes suggested that one can use Cochran's theory to characterized these two special ferroelectric cases by the occurrence of a soft mode behavior [25]. To investigate the soft mode dynamics of these systems it is only necessary to consider the rearrangements of a few atoms in the unit cell and treat the rest of the crystal lattice as a heat bath. We are not going into details and will just assume that the model Hamiltonian describing the structural phase transition will consists of a sum of single-particle contributions and an interaction part

$$H = \sum_i \left[\frac{1}{2} \frac{P_i^2}{2m} + V(Q_i) \right] - \frac{1}{2} \sum_{i,j} v_{ij} Q_i Q_j. \qquad (2.1)$$

The properties of the system described by this model Hamiltonian depend on the shape of the single-particle potential V(Q). The potential field in the order-disorder ferroelectrics, is anharmonic. It has a maximum at Q=0 indicating that this position is unstable. We assume that V(Q) is a double-well potential. Such situations are often found in a hydrogen-bonded systems where the proton can move between two equilibrium sites in the hydrogen bond potential. The proton sits in one of the wells and the bonding energy is the same in either way. Above T_C, the proton distribution in the potential wells is disordered and random between the two equilibrium positions

along the bond length. Below T_C, the potential barrier is too high compared to the interaction between neighbors. As a result, the atoms prefer to remain near to the minima of the wells and the distribution becomes ordered. There will be a larger fraction of protons in one side of the well than in the other one. When the spontaneous polarization increases with the degree of ordering of these protons, the hydrogen ion does not contribute to the spontaneous polarization because the displacement in hydrogen bond is perpendicular to the ferroelectric axis. However, the ordered state of proton induces displacements of KDP along the c-axis that causes the dipole moment.

order-disorder limit   Displacive limit
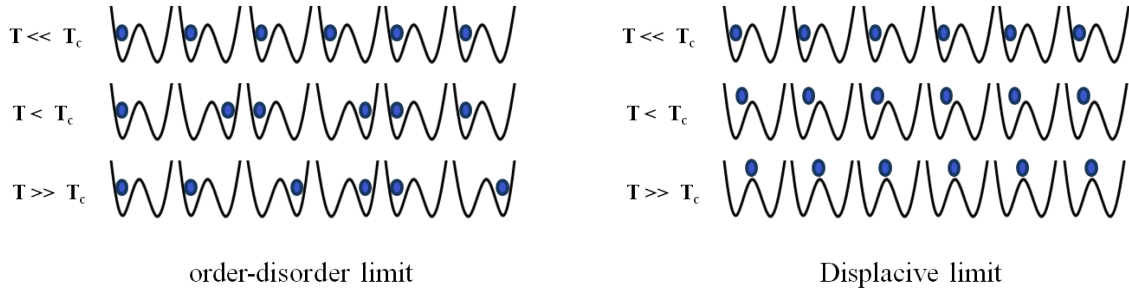
Figure 2.6. – Ordering sequence in the displacive and order-disorder limit.

Although in displacive ferroelectrics the potential in which the nuclei moves is slightly anharmonic, one can use a double-well potential representation as well to interpret the system. Due to the harmonicity, V(Q) has a single minimum. It can be considered as if the atoms spend more time on the same side of the origin. If the interactions between neighboring state are strong enough they can lead to a destabilization of the position at Q=0 which means that particles are able to vibrate about the origin. These two cases are sketched in Fig. 2.6.

The underlying model for this two-level system is the Ising model in a transverse field (TIM). This model is explained in more detail in the following.

2.1.3. Transverse Ising model. A microscopic model for ferroelectrics

We are interested in a qualitative understanding of the physics governing the behavior of ferroelectric materials. To this aim, we present a model which allows a microscopical description for the ferroelectric materials. The analogy between ferromagnetism and ferroelectricity has long been recognized. It was first pointed out by de Gennes [25], and Blinc [26] that the spin-like description of hydrogen-bonded (KDP-type) ferroelectrics can be introduced based on the tunneling model, known as the Ising model in a transverse field (TIM). The transverse field represents the proton tunneling between the two equilibrium positions of the protons within the O-H-O bonds.

For every two-level system, all particle operators can be expressed in terms of spin-$\frac{1}{2}$ operators known as Pauli operators. Considering the polarization direction along the z-axis, states with $B^z = \pm\frac{1}{2}$ are described by pseudospins which refer to a mapping of the two equivalent positions in the well and the interchange between both positions onto spin-$\frac{1}{2}$ operators and have nothing to do with a real spin. In the field

of ferroelectrics, this pseudospin theory has been widely applied to the theoretical studies on ferroelectric films and superlattices in order to explain theoretically the experimentally observed transition properties. Furthermore, the TIM is also applied to displacive type FE such as $BaTiO_3$ [27, 28]. In the case of a very small tunneling frequency with respect to the interaction constant, one may use the TIM as a model for order-disorder FE without tunneling motion (e.g. for $NaNO_2$, TGS). Therefore the TIM can be applied to describe the electric polarization in many types of ferroelectrics. The Hamilton of the Ising model in a transverse field in real space reads [25, 26, 29]

$$H = -2\Omega \sum_i B_i^x - \frac{1}{2} \sum_{i,j} J'_{ij} B_i^z B_j^z. \qquad (2.2)$$

B^z and B^x are the pseudospins operators. B^x is the tunneling operator which represents a jump into the other well of the bond. Ω is the tunneling frequency between the two wells. It describes the dynamic strength of the system. The z-components of pseudospins at neighboring lattice sites i and j interact via the interaction parameter J'_{ij} which depends on the distance between them. The interaction strength is determined by the lattice parameters, the lattice symmetry and the number of nearest neighbors.

The sum is performed over all lattice points of the infinite extended bulk material. For light ions and especially for protons in H-bonded materials, tunneling probability can be quite large. For a very deep double-well there are only two degenerate states near the bottom of each well. This degeneracy is lifted by the quantum mechanical tunneling between the minima.

The expectation value $\langle B^z \rangle$ measures the difference between the occupation of the left and right equilibrium site. The difference in the occupation between the symmetric and antisymmetric energy state is given by $\langle B^x \rangle$. The better understanding of the ferroelectric materials is obtained by including higher order terms in Eq. (2.2) [30, 31]. Although the transverse Ising model is one of the simplest quantum models, the straightforward exact treatment of the transverse Ising model with the space dimension greater than one is very demanding. The Ising model has been applied to various physical systems such as cooperative Jahn-Teller systems and strongly anisotropic magnetic materials in the transverse field. More details about possible applications of this model can be found in reviews by Blinc and Zeks [26] and Stinchcombe [32].

2.1.4. Ferroelectrics at nanoscale

Recent advances in science and technology of ferroelectrics result in the development of micro- and nanoscale ferroelectric structures. As structure dimensions are getting smaller, ferroelectric materials exhibit a pronounced size effect manifesting itself in a significant deviation of the properties of nanoscaled structures from the bulk properties. In this sense, surface energy cannot be neglected in small volumes and long-range dipole interaction is significantly modified in confined geometries. It also depends on whether a ferroelectric is confined in one-, two-, or all three-dimensional structures. In 1944, Onsager [33] showed that in the two-dimensional lattice described

by the Ising model a monolayer of non-oriented dipoles became oriented as a result of the first order phase transition. Many years later, experimental studies [34] confirmed the conclusion that ferroelectricity might still exist in ferroelectric films with the thickness equal to just several unit cells. The size effect in ferroelectrics manifests itself with the reduction in the sample geometrical dimensions by a decrease in the remanent polarization, dielectric permittivity and phase transition temperature, increase in the coercive field, changes in the domain structure and other properties. In addition, noticeable size effect should be also taken in to account since for example transition temperature and spontaneous polarization decrease upon the reduction in the physical dimensions of ferroelectric structures [35].

Parameter which plays an important role in the estimation of the range where the size effects are expected to be significant is the correlation length which describes the width of the domain wall. Although the continuum theories are expected to be valid only at the scales much larger than the lattice constant, many of the size effects down to the nanoscale can be explained by thermodynamic approach using Landau-Ginzburg-Devonshire (LGD) formalism with proper boundary conditions.

2.2. Magnetism

2.2.1. Magnetic order

Magnetic properties are exhibited by many substances. The magnetic moment of the electrons determine the magnetic nature of the material. These moments are originated from the spin of electrons and electron orbital angular momentum. A change in the moments is induced by an applied magnetic field. Magnetic moment per unit volume is known as magnetization. Based on their magnetic properties, these materials are classified into weakly magnetic (paramagnetism (PM) and diamagnetism (DM)) and strongly magnetic (ferromagnetism (FM); antiferromagnetism (AFM) and ferrimagnetism (FIM)). Our treatment will deal with the theoretical problems involving the latter case.

The occurrence of magnetism in transition metal oxides is mainly due to the magnetic moments of the electrons in the partially filled shells. The non-zero spin angular momentum associated with an unpaired electron, an electron that occupies an orbital of an atom singly rather than as part of an electron pair, gives rises to a magnetic moment. Ferromagnetic materials like transition metals, exhibit parallel alignment of magnetic moments to one another giving net spontaneous magnetization even in the zero magnetic field. In an antiferromagnet, equal magnetic spins are aligned antiparallel, as a result the material shows no net magnetic moment. Transition metal oxides are a good examples of AFM materials. Ferrimagnetism is a special case of antiferromagnetism, consisting antiparallel unequal moments, resulting in a non-zero net magnetization. This behavior is observed in complex salts of the transition elements like MnO or Fe_2O_3.

Antiferromagnetic materials can be found in two different phases, commensurate phase in which the periodicity of the spins is linked to the crystal structure, or incommensurate phase where a magnetic periodicity is not a rational divisor of the interatomic spacing. Examples of commensurate antiferromagnetic order for simple cubic crystal is shown in Fig. 2.7. These collinear structures are known as A-type, describing antiferromagnetically coupled ferromagnetic ab-planes, the Neel antiferromagnetic G-type order, or C-type with antiferromagnetically coupled ferromagnetic chain along the c-axis. There is also an unusual E-type antiferromagnetic structure where the material behaves as quasi-two-dimensional antiferromagnet within ab-plane and exhibits ferromagnetic correlations along the c-direction [36]. In addition, there are incommensurate spin structures where non-collinear spin configurations may occur due to competing exchange interactions or by applying external magnetic fields. The first incommensurate phases were discovered in magnetic systems where the magnetic order has a helical structure with a pitch that does not have a rational relation to the underlying lattice. More examples of incommensurate antiferromagnetic order are sinusoidally modulated spin density waves, and cycloidal order, in which the spins change orientation along the propagation direction inside a circular or ellipsoidal envelope (Fig. 2.8).
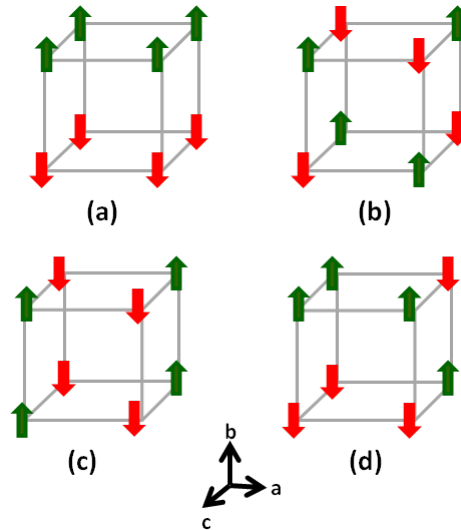
Figure 2.7. – (a) A-type, (b) G-type, (c) C-type and (d) E-type commensurate anti-
ferromagnetic order.
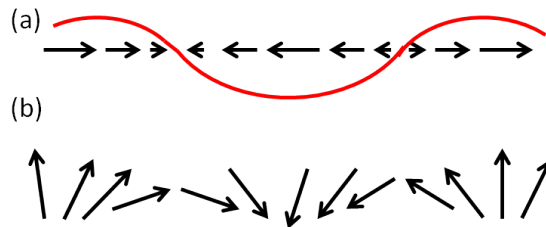
Figure 2.8. – (a) Sinusoidal and (b) Cycloidal incommensurate antiferromagnetic
order.

2.2.2. Magnetic frustration

In a square lattice, the system can easily find an ordered structure of spins to satisfy
antiferromagnetism. In some other materials, where the free spins are arranged in
a triangular or tetrahedral pattern, there is no way to simultaneously satisfy all of
the magnetic interactions. In these materials, magnetic order is said to be frustrated.
Frustration occurs when there is no possible spin configuration that can satisfy a
number of competing exchange interactions and minimize the ground state energy.
A simple 2D example of triangular lattice is shown in Fig. 2.9. Only two out of the
three spins can align antiparallel, the third spin lacks a preferred direction along which
to point because of competing interactions with its neighbors. Unlike the cases of
ferromagnetism and antiferromagnetism, in frustrated materials, the minimum-energy
state may be composed of magnetic moments arranged in a more complex pattern,
such as repeating spirals (helimagnetism), frozen into random orientations with no
long-range order as in spin glasses, or form an incommensurate order. Alternatively,
there may be an enormous number of equally favorable ground states, so that no

particular state stabilizes and the magnetic moments freely fluctuate down to the temperatures available in the laboratory (spin liquid). It also could be the case that magnetic order only achieved at extremely low temperatures due to some symmetry-breaking transition as in spin ice.
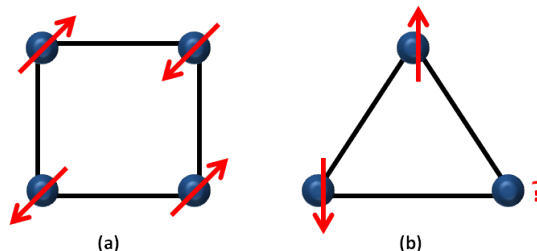
Figure 2.9. – (a) Antiparallel alignment of the magnetic moments in a square lattice and (b) Frustration of magnetic order in triangular lattice.

2.2.3. Exchange interactions

The interaction between magnetic moments is of two types; exchange interaction and dipolar interaction. Ferromagnetism requires a strong force to create the atomic moments and to stabilize the parallel orientation of neighboring moments. A ferromagnetic order established by magnetostatic dipole interaction would be destroyed by temperatures of the order of one Kelvin. The strong force which is responsible for creating and stabilizing spontaneous magnetization is the exchange interaction. The origin of exchange interaction can not be explained classically. It is a pure quantum mechanical phenomena, also it is purely electrostatic in nature. It is a direct consequence of the Pauli's principle, which forbids fermions to occupy the same quantum state. So, double occupancy of an orbital is possible for antiparallel spins ($\uparrow\downarrow$) but forbidden for parallel spins ($\uparrow\uparrow$). As a result, the average separation of electrons, r, will be larger for parallel spins than antiparallel spins. The inter-electron Coulomb repulsion energy ($\frac{e^2}{4\pi\epsilon_0 r}$) is smaller for parallel than antiparallel spins. Hence the parallel alignment is favored by Coulomb interaction. Depending on the system under consideration, this quantum mechanical coupling responsible for cooperative magnetism is described in different ways. A direct overlap of electronic wave functions of the magnetic neighboring atoms is called a direct exchange interaction, which requires different symmetry properties from the spatial and spin parts of the electronic wave function. The direct exchange is a short-range coupling, and the overlap of the neighboring magnetic ions orbitals is rarely sufficient to produce a robust long-range magnetic order.

In many substances the atoms which strongly interact magnetically are quite definitely separated from each other by intervening non-magnetic ions. Such indirect exchange interaction is called superexchange and first suggested by Hendrik Kramers in 1934 [37]. It originates from admixture of excited states of cations with a ground state of an anion. This is best illustrated by the insulating magnetic MnO crystal

which strongly coupled Mn^{2+} ions are separated by a non-magnetic O^{2-} ion directly between them. It is reasonable to allow a considerable admixture of the state in which at least one p electron from oxygen has gone into an s or d state on Mn^{2+}, thus the oxygen is paramagnetic and can enter into magnetic interactions.

In the case of a parallel orientation of the magnetic moments located at the metal centers, no delocalization occurs, which makes the antiferromagnetic alignment energetically favorable. However, hopping requires a nonzero overlap between the involved atomic orbitals. For p and d orbitals, the hopping depends on the bond angles. Based on a symmetry relations and electron occupancy of the overlapping atomic orbitals in the presence of the Pauli exclusion principle, a set of semi-empirical principles were developed which is known as the Goodenough-Kanamori rules [38, 39]. It states that superexchange interactions are antiferromagnetic between overlapping orbitals of magnetic ions that are each half-filled, but they are ferromagnetic when the electron transfer is from a half-filled cation to another cation with empty orbital or from a filled to a half-filled orbital. The other mechanism proposed by Clarence Zener
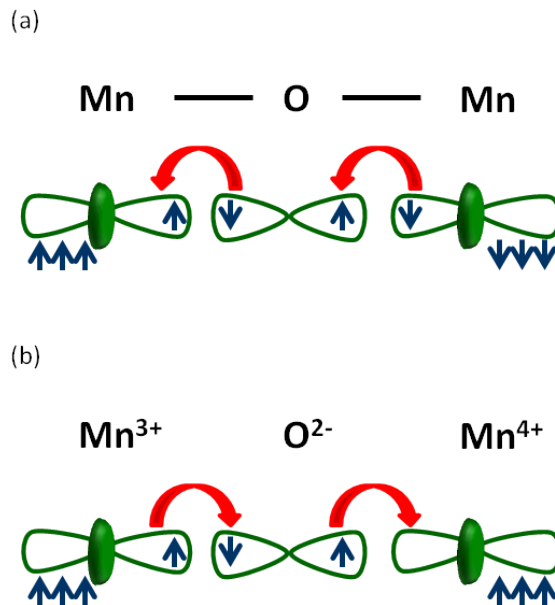
Figure 2.10. – Sketched mechanism for (a) Superexchange illustrated for MnO. The interaction between the magnetic Mn atoms is mediated by the diamagnetic oxygen though the overlap of the metal's 3d and oxygen's 2p orbitals. (b) Double exchange in mixed-valence manganites. Two electrons are transferred simultaneously, one from a bridging O^{2-} anion to the Mn^{4+} center and one from a Mn^{3+} center to the O^{2-} anion. Adapted from [40].

[41], is a type of a magnetic exchange that may arise in an environment containing ions of more than one oxidation state. For example in case of manganites, the mixed valence, Mn^{3+} and Mn^{4+}, leads to ferromagnetic double exchange. Electrons on each Mn ion are aligned according to Hund's rules. Due to hybridization with the oxygen electrons, the spin-up electron jumps from Mn^{3+} to O^{2-} and from O^{2-} to Mn^{4+}. At the end of the hopping process, an electron has moved between the neighboring metal

ions, retaining its spin. Both donating and receiving ions have to be ferromagnetically aligned. Otherwise, the hopping is impossible due to the Pauli exclusion principle. The ability to hop reduces the kinetic energy. Hence the overall energy saving can lead to ferromagnetic alignment of neighboring ions. This model seems to be similar to superexchange. However, in superexchange, a ferromagnetic or antiferromagnetic alignment occurs between two atoms with the same valence (number of electrons); while in double exchange, the interaction occurs only when one atom has an extra electron compared to the other.

Another domain of exchange interactions is antisymmetric superexchange known as Dzyaloshinskii-Moriya exchange interaction which can occur whenever the site symmetry of the interacting ions is uniaxial. It should be mentioned that other exchange mechanisms exist apart from those described above which can be found in literature [42].

2.2.4. Hamiltonian model

Insulating magnetic material is described as assemblies of spins located at crystal lattice sites [43]. The interaction between the localized magnetic moments at different sites is given by the exchange interaction J_{ij}. In case of short range interaction the coupling is restricted to nearest neighbors. For more complicated spin alignments we discuss in this thesis other exchange couplings, see chapter 3. Whereas the exchange coupling favors the ordering of the moments, the temperature tends to prevent such an alignment. The competition between thermal effects and exchange interaction allows the occurrence of the spontaneous magnetisation only for $T < T_N$, where T_N is a well defined sharp transition temperature. For $T > T_N$ the magnetic moments are thermally disordered and there is no net magnetization. The simplest model describing strongly interacting localized magnetic moments is due to Heisenberg and Frenkel. The Hamiltonian of the Heisenberg model has the following form

$$H_1 = -\frac{1}{2} \sum_{i,j} J_{ij} \mathbf{S}_i \mathbf{S}_j - g\mu_B \sum_i \mathbf{B}_i \mathbf{S}_i \,. \tag{2.3}$$

$\mathbf{B}_i$ is the local magnetic field acting on the i-th spin. Here the exchange coupling J_{ij} is often considered as a phenomenological parameter describing the coupling between two spins or magnetic moments represented by the spin operators $\mathbf{S}_i$ and $\mathbf{S}_j$. A positive exchange coupling favors a parallel orientation while a negative J is responsible for an antiferromagnetic order.

In the absence of an external magnetic field, the magnetization M tends to lie along one or several axes in the magnetic solid, called the easy axes. The energy that is required to rotate the magnetization into any different direction from these preferred axes is determined by magnetic anisotropy. The influence of the crystal structure of a substance on its magnetic properties also manifests itself in the dependence of the magnetic properties on the direction along which they are measured. In other words, magnetic substances exhibit magnetocrystalline anisotropy. The magnetocrystalline anisotropy can be represented in different forms due to the symmetry group of the magnetic lattice [44]. In uniaxial ferromagnet which has one easy axis, the single-ion

anisotropy is modeled by

$$H_2 = -\sum_i K_i (\mathbf{S}_i)^2.$$ (2.4)

In a further approximation, one may consider only an effective anisotropy field, H_A which is described by

$$H_A = -g_J \frac{\mu_B}{\hbar} B_A \sum_i S_i^z.$$ (2.5)

In particular, this term is applied to uniaxial antiferromagnets.

The weak ferromagnetic properties of some compounds are known to be produced from spin canting. This prediction was made by Dzyaloshinskii within the framework of symmetry argument. A possible microscopic mechanism was proposed by Moriya, who declared that the required form can be realized by an antisymmetric microscopic coupling between two localized magnetic moments $\mathbf{S}_i$ and $\mathbf{S}_j$. This argument is formulated in the form of Eq. (2.6) and known as Dzyaloshinskii-Moriya interaction (DMI).

$$H_3 = -\frac{1}{2} \sum_{i,j} \mathbf{D}_{ij} (\mathbf{S}_i \times \mathbf{S}_j).$$ (2.6)

DM interaction resembles the form of antisymmetric superexchange interaction and induced by a relativistic spin-orbit coupling. Since this term is proportional to the vector product of spin operators, it is non-zero just for non-collinear spin configurations. $\mathbf{D}_{ij}$ is Dzyaloshinskii-Moriya vector and proportional to the strength of spin-orbit coupling. DMI plays an important role in the theory of the magnetoelectric effect especially in those multiferroic materials with non-collinear magnetic structure [45, 46].

2.2.5. Magnetism at nanoscale

At present, magnetism of nanoscale materials is a vital research field because of its relevance for technological applications in state of the art and future magnetic devices. The properties of nanosized magnets differ substantially from the bulk counterparts due to the increasing role of the surface spins as the particle size is decreased. The antiferromagnetic nanoparticle systems below their Neel temperature provide a particularly interesting case since any observed ferromagnetic-like moment must result from uncompensated surface spins and therefore becomes a direct measurement of the properties of the attractive surface atoms/spins. Temperature dependent magnetic effects of the surface spins lead to several very interesting phenomena like superparamagnetism, magnetic hysteresis, exchange bias and interparticle interactions. A detailed understanding of these complex but interesting properties are very essential to study the presence and role of magnetic nanoparticles in several areas of science and technology including spintronics, biomedical research, and catalysis. for more information see [47].

2.3. Multiferroics

Based on Maxwell's famous equations which were derived in 1865, one expect the coupling between magnetism and electricity in condensed matter. In 1894 Curie mentioned the possibility of an intrinsic correlation between magnetic and electric properties on the basis of symmetry considerations [48]. This coupling has been shown to occur in a small class of materials named magnetoelectric multiferroics.

The magnetoelectric effect was analyzed intensively in the 1950s and 1960s and several compounds have been studied such as $Pb(Fe_{1/2}Nb_{1/2})O_3$, $Pb(Fe_{1/2}Ta_{1/2})O_3$, and $Pb(Fe_{2/3}W_{1/3})O_3$, where the two former compositions were found to be ferroelectric and antiferromagnetic [49, 50]. Nickel iodine boracite $Ni_3B_7O_{13}I$ was the first compound for which simultaneous onset of ferroelectricity and weak ferromagnetism was observed to occur below 61 K [51]. Later, many more boracite compositions revealed both ferroelectric and ferromagnetic behavior. But due to the weakness of the magnetoelectric coupling in most materials and the difficulties of using it in applications, research activities in this field have desponded for a couple of years. The study of multiferroics was revived by the theoretical investigation of Hill [52] who discussed the conditions required for ferroelectricity and ferromagnetism to be compatible in oxides, and by the discoveries of new mechanisms of ferroelectricity in perovskite $TbMnO_3$, hexagonal $YMnO_3$, RMn_2O_5, and $Ni_2V_3O_8$ [53–56]. It was also promoted by the recent developments in thin film growth techniques and in experimental methods for observing magnetic and electronic domains [2, 57].

The term multiferroic was introduced by Schmid in 1994 to define materials that exhibits two or more primary ferroic properties such as ferromagnetism, ferroelectricity, ferroelasticity or ferrotoroidicity in the same phase [58]. Later, the utilization of this term has been expanded to include materials that exhibit any type of long-range magnetic ordering together with spontaneous polarization.
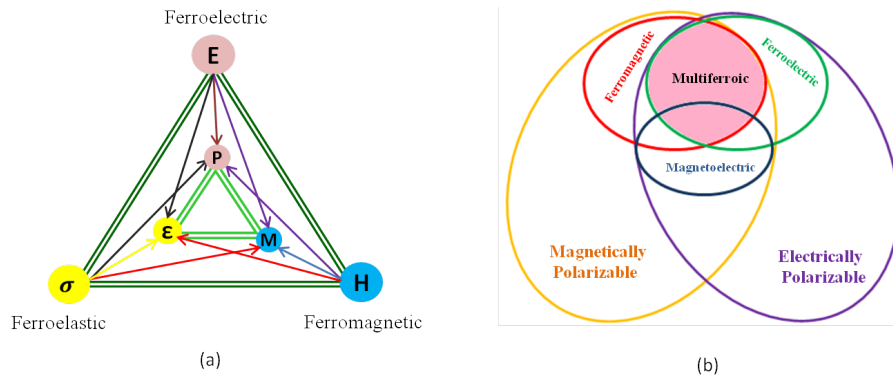
Figure 2.11. – (a) The cross-coupling of properties in a material (b) Multiferroic materials combine magnetic and ferroelectrical properties. Adapted from [59].

However, in the simultaneous presence of long-range ordering of magnetic moments and electric dipoles, polarization can be induced by applying a magnetic field. Materials which are shown such a property called magnetoelectrics. Generally speaking, the magnetoelectric effect is the appearance of a magnetization (polarization) with

the application of an electric (magnetic) field. Thermodynamically, this effect can be understood based on Landau theory, obtained from the expansion of the free energy of a material in powers of the applied magnetic B and the electric field E, i.e.

$$
\begin{aligned}
F(E, H) = & F_0 + P_i E_i + M_i B_i + \frac{1}{2}\epsilon_{ij}E_i E_j + \frac{1}{2}\mu_{ij}B_i B_j \\
& + \alpha_{ij}E_i B_j + \frac{1}{2}\beta_{ijk}E_i B_j B_k + \frac{1}{2}\gamma_{ijk}B_i E_j E_k + \dots ,
\end{aligned}
\tag{2.7}
$$

where ϵ_{ij} is the dielectric permittivity and μ_{ij} is the magnetic permeability. Since the electric field E and magnetic field B are vectors, the linear magnetoelectric susceptibility, shown by α_{ij}, is a tensor. This quantity which corresponds to the induced polarization or magnetization, is designated to the linear magnetoelectric (ME) effect. Higher order ME effects, β_{ijk} and γ_{ijk} are the bilinear ME susceptibility tensors. The corresponding polarization P_i and the magnetization M_i are obtained by minimizing the free energy. Under time reversal symmetry, dielectric quantities are symmetric and magnetic quantities are antisymmetric. Conversely, the magnetisation and magnetic field are invariant under spatial inversion while there would be a change of sign in electric polarization as well as electric field (Fig. 2.12). As a result, the linear magnetoelectric effect only occurs for a material which breaks both time and spatial inversion symmetry. For the first time, Dzyaloshinskii [60] showed explicitly the violation of time-reversal symmetry in antiferromagnetic Cr_2O_3, this was followed by experimental confirmation by Astrov [61]. All linear magnetoelectric materials con-
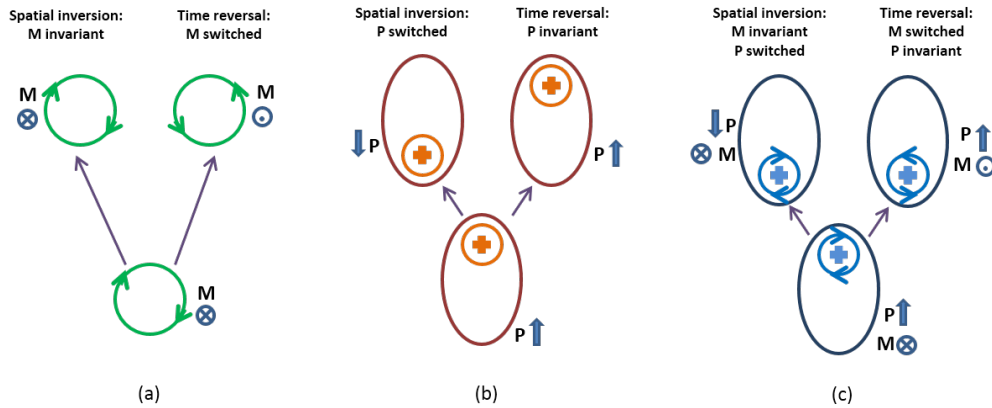
Figure 2.12. – The effect of spatial inversion and time reversal on (a) Ferromagnets, (b) Ferroelectrics and (c) Multiferroics. Adapted from Eerenstein et al. [62].

tain the linear term $\alpha_{ij}E_i H_j$, but this does not necessarily mean that they are multiferroic. For example, Cr_2O_3 is magnetoelectric but not ferroelectric. The opposite is also true; not all multiferroics are necessarily magnetoelectric. Schmid discusses the close connection between magnetoelectric coupling and crystal symmetries in depth in several papers [63, 64].

It is hard to find intrinsic multiferroic materials containing proper ferroelectrics, where structural instability together with the electronic pairing is the main driving force of polar state, since the mechanisms driving ferroelectricity and ferromagnetism are

generally incompatible. Most ferroelectrics are transition metal oxides with empty d-shells. On the contrary, magnetism usually requires a transition metal with a partially filled d-shell, as the spins of electrons occupying completely filled shells add to zero and do not participate in magnetic ordering. Therefore, alternative mechanisms are required to combine these two properties. Recently, various multiferroic materials have been discovered in which a polar state is induced by different types of ordering; these are known as improper ferroelectrics [1].

While the presence of localized electrons in the partially filled ionic shells and the exchange interactions between related spins is the origin of magnetic order in magnets, several microscopic sources of ferroelectricity are found to be responsible for ferroic order. Accordingly, one may expect different types of multiferroics. In general, multiferroic materials can be divided in two main groups. The first group, called type-I multiferroics, are single phase materials having widely separated ferroelectric and magnetic ordering temperatures with rather weak coupling. A single phase materials in which a particular type of magnetic order such as spiral or cycloidal or even collinear magnetic structures causes ferroelectricity known as type-II multiferroics.

2.3.1. Type-I multiferroics

In type-I multiferroics which are more numerous, ferroelectricity and magnetism are generated from different ions and appear largely independent of one another. As a result, the coupling between these two quantity is considerably weak. Besides, the Curie temperature is well above Neel temperature and the spontaneous polarization P is often rather large (of order 10 - 100 $\frac{\mu C}{cm^2}$). This class of multiferroics can be divided into different subclasses due to the number of possible microscopic origins for ferroelectricity [65].

One of the probable origin of ferroelectricity can be the presence of a transition metal with empty d shells in a perovskite structure, just as in $BaTiO_3$. Another possibility is ordering of highly polarized lone pairs of bismuth or lead in specific direction in compounds like $BiFeO_3$ and $PbVO_3$. Lone pairs are two outer 6s electrons that do not participate in chemical bonds.

Ferroelectricity due to charge ordering, often observed in transition metal compounds, especially those which contain transition metal ions with different valence [66]. In case that charge ordering process breaks spatial inversion symmetry, the resulting state can have a net dipole moment. This may happen when both sites and bonds turn out to be inequivalent.

Lastly, we consider the presence of 'geometric' ferroelectricity in hexagonal manganites $RMnO_3$ (R=Ho, Lu, Y) that appears because of the structural phase transition at high temperature. Here, ferroelectricity is caused by the tilting of the MnO_5 bipyramids. This tilting occurs to provide closer packing and the necessary symmetry reduction as a result of phase transition.

An early approach taken by Smolenskii et al. [50] proposed the doping of paramagnetic cations into known non-magnetic ferroelectric compounds. In the case of perovskites, this gives a B-site that contains both a cation with an empty d-shell for ferroelectricity and a cation with a partially filled d-shell for magnetization. For example, $Pb(Mn_{0.5}Nb_{0.5})O_3$ and $Pb(Fe_{0.5}Nb_{0.5})O_3$. The resulting spontaneous po-

larization and magnetization in these complex perovskites were similar to the ferro-magnetoelectric properties that were known in the boracites. However, this type of materials tends to have rather low Curie or Neel temperatures as a result of dilution of the magnetic ions. Due to their strong magnetoelectric effects, we mostly focus on type-II multiferroics. A more complete discussion of type-I multiferroics can be found in related articles and reviews [59, 65].

2.3.2. Type-II multiferroics

In type-II multiferroics the macroscopic electric polarization is directly caused by either an electronic degree of freedom such as spin, charge and orbital ordering or a complex lattice distortion. This means that a strong magnetoelectric coupling must exist between the two orders. However, due to the improper nature of ferroelectricity, the magnitude of polarization is much lower than that of a type-I multiferroics (of order $10^{-2} \frac{\mu C}{cm^2}$). The wide interest in these materials is not because of the strong coupling, rather, it is the high sensitivity of electric properties to the applied magnetic fields. The most well known example of type-II multiferroic with non-collinear spin-spiral structure is $TbMnO_3$, in which the magnetic field can strongly influence the electric polarization. The polarization can be rotated by 90 degrees by applying an external magnetic field in a specific direction [53]. The application of a magnetic field also enhances the dielectric constant by as much as 500% in the case of $DyMnO_3$.

In parallel to the development of multiferroics of spiral (helical) spin order, another type of multiferroics with collinear magnetic structure has also been received attention. Polarization can appear in these frustrated materials as a consequence of exchange-striction. The most prominent example of this group is $TbMn_2O_5$ where the polarization direction changed by $180°$ with applied field, and a field alternating between $+1.5$ and -1.5 Tesla leads to corresponding oscillations in the polarization [55]. These two microscopic mechanisms of magnetically-induced ferroelectricity give rise to two different forms of phenomenological magnetoelectric coupling which will be explained in the following section.

2.3.3. Magnetoelectric coupling in type-II multiferroics

The onset of ferroelectricity in this type of multiferroics is correlated to spin frustration. The first class of type-II multiferroics are those with spiral magnetic order. Like any other magnetic ordering, the magnetic spiral spontaneously breaks time-reversal symmetry. In addition, it breaks inversion symmetry by inverting the direction of spin rotation when the sign of all coordinates are reversed. Thus, the symmetry of the spiral state allows for a simultaneous presence of electric polarization. The mechanism of magnetically induced ferroelectricity in these frustrated structures has been studied using microscopic and phenomenological approaches. The microscopic mechanism involving magnetically induced ionic displacements in spiral ferroelectrics was presented by Katsura et al. by taking into account the spin orbit coupling in the superexchange interaction between nearest neighbor spins [67]. In this case, the

electric polarization has such a form

$$\mathbf{P} \propto \mathbf{r}_{ij} \times \left[\mathbf{S}_i \times \mathbf{S}_j \right] \tag{2.8}$$

for neighboring spins $\mathbf{S}_i$ and $\mathbf{S}_j$ separated by a vector r_{ij}. Being proportional to the vector product of spins, polarization arises only in non-collinear spin ordering. This form of coupling between spins and polarization is similar to the form of DMI. Here the non-collinear spins act back on the lattice to create the lattice distortion that induces ferroelectricity. Hence, the Katsura's picture is sometimes called the inverse Dzyaloshinskii-Moriya effect, as proposed by Sergienko et al. [45].

Based on the phenomenological approach, it is possible to obtain the form of the coupling of the electric polarization P to the magnetization M using general symmetry arguments [60]. The invariance upon the time reversal, t $\longrightarrow$ -t, transforms P $\longrightarrow$ P and M $\longrightarrow$ -M. As a result, the lowest order magnetoelectric coupling term has to be quadratic in M. On the other hand, the symmetry with respect to the spatial inversion, x $\longrightarrow$ -x, upon which P $\longrightarrow$ -P and M $\longrightarrow$ M, is preserved when the coupling of a uniform polarization to an inhomogeneous magnetization is linear in P and contains one gradient of M. Hence, in the case of a spatially inhomogeneous spin configuration the above symmetry argument allows for the third order magnetoelectric coupling term in the Landau free energy [68, 69]

$$\Phi_{mf}(\mathbf{r}) = \gamma \cdot (\nabla \mathbf{M})^2 + \mathbf{P} \cdot \left\{ \gamma'[\mathbf{M}(\nabla \cdot \mathbf{M}) - (\mathbf{M} \cdot \nabla)\mathbf{M}] + \dots \right\}. \tag{2.9}$$

Here r, P and M are spatial coordinate, polarization and magnetization,γ and γ' are the coupling coefficients as well. If we assume that in the absence of magnetism the system shows no instability towards ferroelectricity, we are allowed to only keep the quadratic term in the electric part of thermodynamic potential, $\Phi_f(P) = \frac{P^2}{2\chi_f}$, where χ_f is the dielectric susceptibility in the absence of magnetization. For cubic crystals, the allowed form of the magnetically induced electric polarization is obtained by minimization of the free energy with respect to P

$$\mathbf{P} = \gamma' \chi_e [(\mathbf{M} \cdot \nabla)\mathbf{M} - \mathbf{M}(\nabla \cdot \mathbf{M})]. \tag{2.10}$$

For example, in the case of spin-spiral structure which is expressed by

$$\mathbf{M} = S_1 \mathbf{e_1} \cos(Q \cdot x) + S_2 \mathbf{e_2} \sin(Q \cdot x), \tag{2.11}$$

the polarization is

$$\mathbf{P} = \gamma' \chi_e S_1 S_2 (\mathbf{e_3} \times \mathbf{Q}). \tag{2.12}$$

Here Q is the propagation vector of the spiral. This equation is so similar to Eq. (2.8) where P is proportional to the cross product of spins in different lattice sites. One can conclude that the Katsura et al. model is a microscopic interpretation of Mostovoy phenomenological analysis [68]. Therefore, the spin-orbit interaction can be considered as the origin of the coupling between the magnetic and ferroelectric orders in these type of multiferroics.

The spin-orbit coupling is not the only possible way towards the magnetism-induced ferroelectricity. The collinear spin arrangements can induce polarization without considering the spin-orbit interaction. In this type of frustrated magnetic structure, polarization can appear via the exchange-striction associated with symmetric superexchange coupling plus charge-ordered state. To explain the related mechanism, we

consider a one-dimensional Ising chain with competing ferromagnetic nearest neighbor (NN) exchange J_1 and antiferromagnetic next nearest neighbor (NNN) exchange J_2, i.e.

$$H = J_1 \sum_i \mathbf{S}_i \cdot \mathbf{S}_{i+1} + J_2 \sum_i \mathbf{S}_i \cdot \mathbf{S}_{i+2} \,. \tag{2.13}$$

For $J_2 \geq \mid J_1 \mid /2$ the ground state configuration corresponds to $\uparrow\uparrow\downarrow\downarrow$ state. In this case, the exchange-striction together with the symmetric superexchange interaction shortens the bonds between the parallel spins, while lengthening those between the antiparallel spins. Consequently, spatial inversion symmetry is lost and an electric polarization may arise along the chain direction, as it shown schematically in Fig. 2.13. In the case of $J_2 \geq \mid J_1 \mid /4$, due to the competition between ferromagnetic and antiferromagnetic order, the magnetic subsystem becomes frustrated and develops a spiral structure [70].
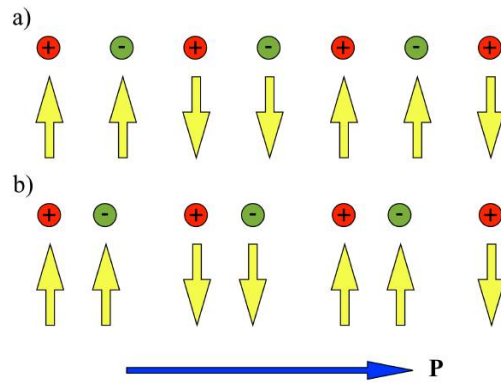
Figure 2.13. – The magnetoelectric mechanism for collinear magnetic structures. (a) One-dimensional chain with alternating charges and $\uparrow\uparrow\downarrow\downarrow$ spin structure, (b) Magnetostriction effect, which shortens the ferromagnetic bonds and generates a ferroelectric polarization. Taken from [59].

Most members of this class of multiferroics possess complicated magnetic structure which hardly can be explained using such a simplified picture. We will discuss some of these components in more detail in the following chapters.

2.4. Double-time Green's function method

The double time Green's function approach is widely used in statistical mechanics because it is an effective method of calculating the observable macroscopic properties of the system as well as the microscopic quantities like the expectation values and correlation functions, without an explicit knowledge of the partition function [43, 44, 71]. The other advantage of this method is that the results obtained are applicable to a wide range of temperatures and enables the treatment of systems with arbitrary spin. We shall follow Bogolyubov and Tyablikov [43] and use the double-time retarded Green's function which is very convenient for applications in statistics as they can be analytically continued in the complex plane. One can uses Matsubara's temperature-dependent Green's functions in statistical mechanics, which are apparently less convenient than the temperature- and time-dependent Green's functions.

2.4.1. The equation of motion

Let A(t) and $B(t')$ be some operators in the Heisenberg representation

$$A(t) = e^{\frac{i}{\hbar}\mathcal{H}t}A(0)e^{-\frac{i}{\hbar}\mathcal{H}t} \quad , \quad B(t') = e^{\frac{i}{\hbar}\mathcal{H}t'}B(0)e^{-\frac{i}{\hbar}\mathcal{H}t'} \, , \tag{2.14}$$

$\mathcal{H}$ is the Hamiltonian of the system in the grand-canonical ensemble

$$\mathcal{H} = H - \mu\hat{N} \, . \tag{2.15}$$

μ is the chemical potential and N is the operator of the total number of particles. In general, the operators A and B are second quantized operators. The equation of motion for these operators has the form

$$i\hbar\frac{\partial A(t)}{\partial t} = [A(t), \mathcal{H}] = A(t)\mathcal{H} - \mathcal{H}A(t) \, . \tag{2.16}$$

The double-time retarded Green's function is defined by

$$G_{AB}(t,t') = \langle\langle A(t); B(t')\rangle\rangle = -\frac{i}{\hbar}\Theta(t - t')\langle[A(t), B(t')]\rangle \, . \tag{2.17}$$

The step function Θ is written in the following way

$$\Theta(t) = \int_{-\infty}^{t} e^{\epsilon t'}\delta(t')dt' \quad (\epsilon \longrightarrow +0) \, . \tag{2.18}$$

It results

$$\Theta(t - t') = \begin{cases} 1 & t > t' \\ 0 & t < t' \end{cases} \tag{2.19}$$

and

$$\frac{d\Theta(t)}{dt} = \delta(t) \, . \tag{2.20}$$

In the case of statistical equilibrium, one can shows that the Green's function depends only on the difference between the time arguments

$$G_{AB}(t,t') = G_{AB}(t - t') \, . \tag{2.21}$$

The Green's functions are determined by their equation of motion

$$i\hbar\frac{\partial G_{AB}(t-t')}{\partial t} = \delta(t-t')\langle[A(t),B(t')]\rangle + \langle\langle[A(t),\mathcal{H}] \mid B(t')\rangle\rangle. \tag{2.22}$$

In more general cases, the right hand side of Eq. (2.22) contains the double-time Green's functions of higher order, for which a new equation of motion can be written. Therefore, instead of a closed set of equations we obtain an infinite chain of equations involving Green's functions of successively higher orders. To solve this hierarchy, we impose boundary conditions for t. The form of these conditions can be extracted from the Green's function definition (Eq. (2.17)). It is more convenient to use the Fourier transforms of the Green's functions

$$E\langle\langle A \mid B\rangle\rangle_E = \hbar\langle[A,B]\rangle + \langle\langle[A,\mathcal{H}] \mid B\rangle\rangle_E. \tag{2.23}$$

Thus, we are no longer dealing with a differential equation, but instead with a purely algebraic equation. Besides, the boundary conditions are in the form of spectral representations of the Green's functions. We note that the appearance of infinite chains of coupled equations is unavoidable for the system of interacting particles. In this case, approximation schemes are necessary to express high-order Green's functions as a product of Green's functions of lower order.

2.4.2. Spectral representation

The Green's functions have a spectral representation which enables us to find the correlation function. We shall represent the time correlation function by $\langle A(t)B(t')\rangle$ which can be written as

$$\begin{aligned}
\langle A(t)B(t')\rangle &= \frac{1}{\Xi}Tr\{e^{-\beta\mathcal{H}}A(t)B(t')\} \\
&= \frac{1}{\Xi}\sum_n\langle E_n \mid e^{-\beta\mathcal{H}}A(t)B(t') \mid E_n\rangle \\
&= \frac{1}{\Xi}\sum_{n,m}\langle E_n \mid B \mid E_m\rangle\langle E_m \mid A \mid E_n\rangle e^{-\beta E_n}e^{\beta(E_n-E_m)}\times \\
&\times \exp\left[-\frac{i}{\hbar}(E_n-E_m)(t-t')\right] \quad, \; \Xi = Tr(e^{-\beta\mathcal{H}}).
\end{aligned} \tag{2.24}$$

Ξ is the grand-canonical partition function. In analogy to the above calculation, one get the other correlation function

$$\langle B(t')A(t)\rangle = \frac{1}{\Xi}\sum_{n,m}\langle E_n \mid B \mid E_m\rangle\langle E_n \mid A \mid E_n\rangle e^{-\beta E_n}\times \tag{2.25}$$

$$\times \exp\left[-\frac{i}{\hbar}(E_n-E_m)(t-t')\right]. \tag{2.26}$$

Time-correlation functions are an effective and intuitive way of representing the dynamics of a system. We now define the spectral density, which is important in the following considerations

$$S_{AB}(t,t') = \frac{1}{2\pi}\langle[A(t),B(t')]\rangle. \tag{2.27}$$

Inserting Eq. (2.24) and Eq. (2.26) into Eq. (2.27) and do the related Fourier transformation, we end up with the so-called spectral representation of the spectral density

$$S_{AB}(E) = \frac{\hbar}{\Xi} \sum_{n,m} \langle E_n \mid B \mid E_m \rangle \langle E_m \mid A \mid E_n \rangle e^{-\beta E_n}(e^{\beta E} + 1)\delta(E_n - E_m + E) \,. \quad (2.28)$$

The argument of the δ-function contains the possible excitation energies of the system. With this, the spectral representation of retarded Green's function obtain

$$G_{AB}(E) = \int_{-\infty}^{\infty} dE' \frac{S_{AB}(E')}{E - E' + i0^+} \,. \quad (2.29)$$

The singularities of these functions are identical with the excitation energies of the system. Considering the spectral density as a real quantity, we get

$$S_{AB}(E) = -\frac{1}{\pi} Im G_{AB}(E) \,. \quad (2.30)$$

2.4.3. Spectral theorem

The relation between the correlation function and the related Green's function is given by the spectral theorem

$$\langle B(t')A(t) \rangle = \frac{1}{\hbar} \int_{-\infty}^{\infty} dE \frac{S_{AB}(E)}{e^{\beta E} - \epsilon} e^{-\frac{i}{\hbar}E(t-t')} + C \quad (2.31)$$

$$= \lim_{\delta \to 0^+} \frac{i}{\hbar} \int_{-\infty}^{\infty} e^{-\frac{i}{\hbar}E(t-t')} \frac{G(E + i\delta) - G(E - i\delta)}{e^{\beta E} - \epsilon} dE + C \,. \quad (2.32)$$

The constant C can be determined from the limiting case which is to be carried out in a complex plane

$$\lim_{E \to 0^+} E G_{AB}^{(\epsilon)}(E) = (1 - \epsilon)\hbar C, \quad \epsilon = \pm 1 \,. \quad (2.33)$$

$G_{AB}^{(+)}(E)$ and $G_{AB}^{(-)}(E)$ are the commutator or anticommutator Green's functions defined as

$$G_{AB}^{(-)}(E) = \frac{\hbar}{\Xi} \sum_{n,m} \langle E_n \mid B \mid E_m \rangle \langle E_m \mid A \mid E_n \rangle e^{-\beta E_n} \frac{e^{\beta(E_n - E_m)} + 1}{E - (E_n - E_m)}, \quad (2.34)$$

$$G_{AB}^{(+)}(E) = \frac{\hbar}{\Xi} \sum_{n,m}^{E_n \neq E_m} \langle E_n \mid B \mid E_m \rangle \langle E_m \mid A \mid E_n \rangle e^{-\beta E_n} \frac{e^{\beta(E_n - E_m)} - 1}{E - (E_n - E_m)} \,. \quad (2.35)$$

Using spectral theorem, as in Eq. (2.32), one can calculate correlation functions with the help of the Green's functions. These functions characterize the structure of the system and provide more detailed information than thermodynamic quantities. In the next chapters, the application of Green's function technique to investigate the properties of multiferroic systems will be presented. In the forthcoming chapters we work with natural unit where $\hbar = k_B = 1$.

3. Theoretical study of multiferroic bulk systems

3.1. General Hamiltonian for multiferroics

In this chapter, the elementary excitations, the damping and the resulting macroscopic quantities such as magnetization and polarization of different multiferroic systems will be analyzed using Green's function technique. Especially the influence of spin-phonon interaction, the effect of ion doping and the single ion anisotropy will be studied. Furthermore, we focus on the effect of external magnetic and electric fields on the spin wave dispersion and the related phonon modes. We consider the model Hamiltonian

$$H = H_m + H_f + H_{mf}\,, \tag{3.1}$$

where H_m, H_f and H_{mf} describe the magnetic part, the ferroelectric part and the coupling between these two subsystems. Here, we mainly concentrate on those type of multiferroics where the spin configuration in their frustrated magnetic structures is responsible for the appearance of ferroelectricity. The magnetic part H_m is expressed by the Heisenberg spin Hamiltonian with two competing coupling parameters namely the nearest neighbor ferromagnetic interaction $J > 0$, denoted as ij, and next nearest neighbor antiferromagnetic exchange interaction $\tilde{J} > 0$, indicated by $< ij >$

$$H_{\mathrm{m}} = -\frac{1}{2}\sum_{i,j} J_{ij}\mathbf{S}_i \cdot \mathbf{S}_j + \frac{1}{2}\sum_{<i,j>} \tilde{J}_{ij}\mathbf{S}_i \cdot \mathbf{S}_j - \sum_i D_i(S_i^z)^2 - h\sum_i S_i^z\,. \tag{3.2}$$

D ($D < 0$) is the single-site anisotropy parameter, $\mid D \mid < J$ and $h = g\mu_B B$ where B is the external magnetic field. It is appropriate to introduce spin-ladder operators $S^{\pm} = S^x \pm iS^y$ leading to

$$H_m = -\frac{1}{2}\sum_{i,j} J_{ij}(S_i^+ S_j^- + S_i^z S_j^z) + \frac{1}{2}\sum_{<i,j>} \tilde{J}_{ij}(S_i^+ S_j^- + S_i^z S_j^z) - \sum_i D_i(S_i^z)^2 - h\sum_i S_i^z\,. \tag{3.3}$$

The ferroelectric behavior is based on the Ising model in a transverse field (TIM), the relevance of which was discussed in section 2.1.3. The Hamiltonian reads

$$H_f = -\frac{1}{2}\sum_{i,j} J'_{ij}B_i^z \cdot B_j^z - 2\Omega\sum_i B_i^x - \mu E\sum_i B_i^z\,. \tag{3.4}$$

Here E represents the external electric field and μ is electron mobility. Because both mean values $\langle B^z\rangle$ and $\langle B^x\rangle$ are nonzero in the ordered phase, it is appropriate to

introduce a new coordinate system rotating the original one by an angle ν in the xz-plane. Following the calculations for magnetic system, we introduce step operators B_i^+ and B_i^-. In case of a spin $\frac{1}{2}$ system, the operators are equal to the Pauli operators b_i, b_i^+ and $B_i^z = \frac{1}{2} - \rho_i$. Accordingly, the averaged values $\langle B_i^+ \rangle$ and $\langle B_i^- \rangle$ are nonzero. These expressions are omitted by a rotation of the spin operators

$$\begin{pmatrix} B_i^{x'} \\ B_i^{y'} \\ B_i^{z'} \end{pmatrix} = \begin{pmatrix} \cos\nu & 0 & -\sin\nu \\ 0 & 1 & 0 \\ \sin\nu & 0 & \cos\nu \end{pmatrix} \begin{pmatrix} B_i^{x} \\ B_i^{y} \\ B_i^{z} \end{pmatrix} . \tag{3.5}$$

Hence the component based on the new operators are defined as

$$B_i^{x'} = (\frac{1}{2} - \rho_i)\sin\nu + \frac{1}{2}(b_i + b_i^\dagger)\cos\nu \,,$$

$$B_i^{y'} = \frac{i}{2}(b_i^\dagger - b_i),$$

$$B_i^{z'} = (\frac{1}{2} - \rho_i)\cos\nu - \frac{1}{2}(b_i + b_i^\dagger)\sin\nu \,, \quad \rho_j = b_i^\dagger b_i \,.$$

The angle ν is determined in such a manner that $\langle B^{x'} \rangle = 0$ after rotation, provided the system is within the range $T_C \leq T$. The last term in Eq. (3.1) describes the coupling between the magnetic and the ferroelectric subsystems. It should be emphasized that various mechanisms of this ME coupling were predicted for both single phase multiferroics and composite materials involving ferroelectric and magnetic phases. It is of fundamental interest to understand how such a coupling comes about and what is the microscopic mechanism behind the ME coupling in multiferroics.

Due to [72, 73] type I multiferroics allow a biquadratic coupling in spin operator **S** and pseudospin operators **B**

$$H_{mf} = -\sum_{i,j}\sum_{k,l} K_{ijkl} B_k^z B_l^z \mathbf{S}_i \cdot \mathbf{S}_j \,. \tag{3.6}$$

The use of biquadratic coupling between the pseudospins and magnetic moments implies that the magnetic and ferroelectric orderings have independent mechanisms. In particular, this generally leads to different transition temperatures for the two subsystems, $T_C >> T_N$, and the ME coupling is small, for example in hexagonal RMnO$_3$ and BiFeO$_3$. Katsufuji et al. [74] found that the changes in dielectric and magnetic properties of the hexagonal ferroelectromagnet RMnO$_3$ are dominated by the pair correlation of the nearest neighbor Mn ions, $< \mathbf{S}_i\mathbf{S}_j >$. Thus, for the coupling of intrinsic spin and polarization, there are sufficient reasons for proposing such a biquadratic ME coupling term.

For improper multiferrics where the ferroelectricity is driven by the magnetic ordering, the relevant magnetoelectric coupling H_{mf} is given by

$$H_{\mathrm{mf}} = -\sum_{i,j,r} K_{ijr} B_r^z \mathbf{S}_i \cdot \mathbf{S}_j \,. \tag{3.7}$$

In these Multiferroics, the transition temperatures are nearly of the same order, $T_N \geq T_C$, and the ME coupling is stronger compared to the biquadratic case.

Here K is the coupling constant between the magnetic and the electric order parameters. The underlying physical mechanism of the coupling is that the cooperative alignment of magnetic moments at a certain temperature is the reason for the polarization. The ME coupling in this group of multiferroics should be invariant with respect to spacial inversion. As mentioned before, the magnetization is odd under time reversal whereas the polarization changes its sign for spatial inversion. If the system already has broken inversion symmetry, lower-order coupling by the form of Eq. (3.7) is possible. This coupling corresponds to the phenomenological treatment of Mostovoy [68], see Eq. (2.10) where the coupling is given by $\dot{P}M(\nabla \dot{M})$.

3.2. Calculation of the Green's functions

The method of Green's function was introduced in section 2.4. Here, we introduce another method proposed by Tserkovnikov [75] for the approximate calculation of the Green's functions. The system's Hamiltonian consists of the non-interacting term (H_0) and the interacting part (H_1). In the Heisenberg representation, the operator B(t) satisfies the equation of motion

$$i\frac{dB_q(t)}{dt} = \epsilon_q B_q + J_q(t).$$
$$(3.8)$$

Here $[B, H_0] = \epsilon B$ and $J = [B, H_1]$ are the flux operator corresponding to B. The equation of motion for the Green's function is

$$i\frac{d}{dt}\langle\langle B_q(t); B_q^\dagger\rangle\rangle = \delta(t)\langle[B_q, B_q^\dagger]_\mp\rangle + \epsilon_q\langle\langle B_q(t); B_q^\dagger\rangle\rangle - i\Theta(t)\langle[J_q(t), B_q^\dagger]_\mp\rangle.$$
$$(3.9)$$

$[B, B^\dagger]_\mp = BB^\dagger \mp B^\dagger B$ is the commutator or anticommutator chosen for convenience. Eq. (3.9) can be represented in the form

$$i\frac{d}{dt}\langle\langle B_q(t); B_q^\dagger\rangle\rangle = \delta(t)\langle[B_q, B_q^\dagger]_\mp\rangle + [\epsilon_q + R_q(t)]_\mp\langle\langle B_q(t); B_q^\dagger\rangle\rangle,$$

$$R_q(t) = \frac{\langle[J_q(t), B_q^\dagger]_\mp\rangle}{\langle[B_q(t), B_q^\dagger]_\mp\rangle} = \frac{\langle[[B_q(t), H_{q1}(t)], B_q^\dagger]_\mp\rangle}{\langle[B_q(t).B_q^\dagger]_\mp\rangle}.$$
$$(3.10)$$

The exact solution of Eq. (3.9) is

$$\langle\langle B_q(t); B_q^\dagger\rangle\rangle = G_q(t) = -i\Theta(t)\langle[B_q, B_q^\dagger]\rangle exp(-itE_q(t)).$$
$$(3.11)$$

The related complex energy is

$$E_q(t) = \epsilon_q - \frac{i}{\hbar t}\int_0^t t'dt'\left(\frac{\langle[J_q(t), J_q^\dagger(t')]_\mp\rangle}{\langle[B_q(t), B_q^\dagger(t')]_\mp\rangle} - \frac{\langle[J_q(t), B_q^\dagger(t')]_\mp\rangle\langle[B_q(t), J_q^\dagger(t')]_\mp\rangle}{\langle[B_q(t), B_q^\dagger(t')]_\mp\rangle^2}\right).$$
$$(3.12)$$

In this case the time-independent term

$$\epsilon_q = \frac{\langle[[B_q^\dagger, H], B_q]\rangle}{\langle[B_q^\dagger, B_q]\rangle}$$
$$(3.13)$$

is the soft mode energy in the generalized Hartree-Fock approximation. The second term in Eq. (3.12) represents the associated damping, which is connected to the damping of the modes.

For the ferroic subsystem, the operators B and $B^\dagger$ are defined as

$$B_q = \begin{pmatrix} b_q \\ b_q^\dagger \\ \rho_q \end{pmatrix} , \quad B_q^\dagger = (b_q^\dagger, b_{-q}, \rho_{-q}) . \tag{3.14}$$

The retarded Green's function in matrix form is

$$G_q(t) = -i\Theta(t)\langle[B_q(t), B_q^\dagger]\rangle = \begin{pmatrix} \langle\langle b_q(t); b_q^\dagger\rangle\rangle & \langle\langle b_q(t); b_{-q}\rangle\rangle & \langle\langle b_q(t); \rho_{-q}\rangle\rangle \\ \langle\langle b_{-q}^\dagger(t); b_q^\dagger\rangle\rangle & \langle\langle b_{-q}^\dagger(t); b_{-q}\rangle\rangle & \langle\langle b_{-q}^\dagger(t); \rho_{-q}\rangle\rangle \\ \langle\langle \rho_q(t); b_q^\dagger\rangle\rangle & \langle\langle \rho_q(t); b_{-q}\rangle\rangle & \langle\langle \rho_q(t); \rho_{-q}\rangle\rangle \end{pmatrix} . \tag{3.15}$$

In the first step we consider only G^{11} to be non-zero. The Fourier transformation of Eq. (3.11) reads

$$G_q(E) = \int_{-\infty}^{\infty} G_q(t)e^{iEt}dt , \quad \mathrm{Im}E \geq 0 . \tag{3.16}$$

To calculate the polarization of the system under study one needs to find the correlation function $\langle b_q^\dagger b_q\rangle$. Based on the spectral theorem we can write

$$\langle b_q^\dagger b_q\rangle = \int_{-\infty}^{\infty} n(E)S_q(E)dE , \quad n(E) = (e^{\beta E} - 1)^{-1}$$

$$S_q(E) = -\frac{1}{\pi}\mathrm{Im}G_q(E + i\varepsilon) = \frac{1}{2\pi}\int_{-\infty}^{\infty} e^{-\varepsilon(t)}e^{iEt}\langle[b_q, b_q^\dagger]\rangle dt . \tag{3.17}$$

So

$$\langle b_q^\dagger b_q\rangle = \frac{2}{N}P\sum_{\mathbf{q}}\frac{1}{\exp(\beta E^f(\mathbf{q})) - 1} . \tag{3.18}$$

For spin $\frac{1}{2}$ one get $P = \frac{1}{2} - \langle b_q^\dagger b_q\rangle$. As a result

$$P = \frac{\frac{1}{2}}{1 + \frac{2}{N}\sum_{\mathbf{q}}\frac{1}{\exp(\beta E^f(\mathbf{q})) - 1}} , \tag{3.19}$$

which can be written as

$$P = \langle\sigma_P\rangle = \frac{1}{2N}\sum_{\mathbf{q}}\tanh\frac{E^f(\mathbf{q})}{2k_BT} . \tag{3.20}$$

The transverse pseudospin-wave energy $E^f(\mathbf{q})$ and the damping Γ_f are calculated beyond the RPA

$$\begin{aligned} E^f(\mathbf{q}) &= 2\Omega\sin\nu + \frac{1}{2}P\cos^2\nu J'_{eff}(0) - \frac{1}{4}P\sin^2\nu J'_{eff}(\mathbf{q}) + \mu E\cos\nu \\ &- \frac{1}{PN}\sum_{\mathbf{k}}\left(\cos^2\nu J'_{eff}(\mathbf{q} - \mathbf{k}) - \frac{1}{2}\sin^2\nu J'_{eff}(\mathbf{k})\right) < b_k^\dagger b_k > . \end{aligned} \tag{3.21}$$

$$\Gamma_f(\mathbf{q}) = \frac{\pi}{2N^2} \sum_{\mathbf{k},\mathbf{p}} \Bigg[\big(V(\mathbf{k}, \mathbf{q} - \mathbf{k}) + V(\mathbf{q} - \mathbf{p} - \mathbf{k}, \mathbf{p} + \mathbf{k}) \big)^2$$
$$+ \big[\bar{n}(\mathbf{p})\big(P + \bar{n}(\mathbf{p} + \mathbf{k}) + \bar{n}(\mathbf{q} - \mathbf{k}) \big) - \bar{n}(\mathbf{p} + \mathbf{k})\bar{n}(\mathbf{q} - \mathbf{k}) \big] \qquad (3.22)$$
$$\times \delta \big(E^f(\mathbf{q} - \mathbf{k}) + E^f(\mathbf{p} + \mathbf{k}) - E^f(\mathbf{p}) - E^f(\mathbf{q}) \big) \Bigg].$$

$\bar{n}(\mathbf{k}) = \langle B_{\mathbf{k}}^- B_{\mathbf{k}}^+ \rangle$, $V(\mathbf{k}, \mathbf{q} - \mathbf{k}) = J'_{eff}(\mathbf{k}) \cos^2 \nu - 0.5 J'_{eff}(\mathbf{q} - \mathbf{k}) \sin^2 \nu$. The coupling term is given by Eq. (3.6). Consequently, $J'_{eff} = J'_0 + 2K(\langle S_q^- S_q^+ \rangle + \langle S_q^z S_q^z \rangle)$. Within the generalized Hartree-Fock approximation the rotation angle ν is determined by the condition $\langle [b_k, H] \rangle = 0$. This ensures a minimization of the free energy [103,114] for the field free case

$$\begin{cases} \cos \nu = 0, \quad \nu = \frac{\pi}{2}, & \text{if } T \geq T_c, \\ \sin \nu = \frac{4\Omega}{J_{eff} P} = \frac{P_c}{P}, & \text{if } T \leq T_c. \end{cases}$$

The magnetic correlation function $\langle S^- S^+ \rangle$ and the magnetization M$= \langle \sigma_M \rangle = \langle S^z \rangle$ are calculated from the spin Green's function in a similar way

$$\frac{1}{M} = \frac{1}{N} \sum_{\mathbf{q}} \coth\left(\frac{\beta E^m(\mathbf{q})}{2} \right). \qquad (3.23)$$

E^m is the spin-wave energy taking into account all correlation functions

$$E^m(\mathbf{q}) = \frac{1}{2M} \frac{1}{N} \sum_k (J_{eff}(\mathbf{k}) - J_{eff}(\mathbf{q} - \mathbf{k}) + \tilde{J}_{eff}(\mathbf{k})$$
$$- \tilde{J}_{eff}(\mathbf{q} - \mathbf{k}))(2\langle S_k^z S_{-k}^z \rangle - \langle S_{q-k}^z S_{q-k}^+ \rangle) + 2MD + g\mu_B B. \qquad (3.24)$$

D is the single-site anisotropy parameter and M is the magnetization. Due to the ME coupling the exchange interaction constant is also renormalized to $J_{eff} = J + 2KP^2 \cos^2 \nu$ and correspondingly $\tilde{J}$. Calculations are possible using Eq. (3.7) where for example the renormalized exchange interaction constant will be $J_{eff} = J + KP \cos \nu$.

The analytical expressions for the excitation energies in Eqs. (3.21) and (3.24) are obtained without any approximation, the correlation functions are observed from the spectral theorem. By the numerical calculations we have made the following approximation in J'_{eff} and in Eq. (3.24): the longitudinal correlation function $< S^z S^z >$ is decoupled to $< S^z >< S^z >$. The approximations are consistent with the strong ME coupling mechanism. The spin-wave damping is calculated to

$$\Gamma_m(\mathbf{k}) = \frac{2M}{N^2} \sum_{\mathbf{p},\mathbf{q}} \Bigg[\big(J_{eff}^2(\mathbf{k}, \mathbf{q}, \mathbf{p}) + \tilde{J}^2(\mathbf{k}, \mathbf{q}, \mathbf{p}) + D^2 \big) k$$
$$\times \big[\bar{N}(\mathbf{p})\big(1 + \bar{N}(\mathbf{p} + \mathbf{q}) + \bar{N}(\mathbf{k} - \mathbf{q}) \big) - \bar{N}(\mathbf{p} + \mathbf{q})\bar{N}(\mathbf{k} - \mathbf{q}) \big] \qquad (3.25)$$
$$\times \delta \big(E^m(\mathbf{k} - \mathbf{q}) + E^m(\mathbf{p} + \mathbf{q}) - E^m(\mathbf{p}) - E^m(\mathbf{k}) \big) \Bigg].$$

$\bar{N}(q) = \langle S_q^+ S_q^- \rangle$ is the spin correlation function which is obtained via the spectral theorem. Using the Hamiltonians Eq. (3.2), Eq. (3.4), Eq. (3.7), for instance and solving the equation of motion for the Green's function one can find directly the dispersion relation. For the magnetic subsystem let us define the Green's function by

$$G_{lm}^m(t - t') \equiv \langle\langle S_l^+(t); S_m^-(t') \rangle\rangle = -i\Theta(t - t')\langle [\, S_l^+(t)\,, S_m^-(t')\,]\rangle \,. \tag{3.26}$$

Following the method of the equation of motion for the Green's functions which is introduced in section 2.4, and using the appropriate commutation relations, the Green's function is written as

$$E^m \langle\langle S_l^+; S_m^- \rangle\rangle = \langle [S_l^+, S_m^-] \rangle + \langle\langle [S_l^+; H]; S_m^- \rangle\rangle \,. \tag{3.27}$$

$[S_l^+, H] = [S_l^+, H_m] + [S_l^+, H_{mf}]$. Throughout this thesis, a system of units is used such that $\hbar = 1$. Within the rotated system we have

$$
\begin{aligned}
[S_l^+, H] = &-\sum_i J_{il} S_i^+ S_l^z + \frac{1}{2}\sum_i J_{il}\big(S_l^+ S_i^z + S_i^z S_l^+\big) + \sum_r \tilde{J}_{rl} S_r^+ S_l^z \\
&-\frac{1}{2}\sum_r \tilde{J}_{rl}\big(S_l^+ S_r^z + S_r^z S_l^+\big) - D\sum_i S_i^z S_i^+ \delta_{il} - D\sum_i S_i^+ S_i^z \delta_{il} - h\sum_i S_i^+ \delta_{il} \\
&-\sum_{i,j} K_{ijl}\left((\frac{1}{2} - \rho_j)\cos\nu + \frac{1}{2}(b_j^\dagger + b_j)\sin\nu\right)(S_l^+ S_i^z + S_i^z S_l^+)\,.
\end{aligned}
\tag{3.28}
$$

It results

$$
\begin{aligned}
E^m \langle\langle S_l^+; S_m^- \rangle\rangle = &2\langle S_z \rangle - \sum_i J_{il}\left(\langle\langle S_i^+ S_l^z; S_m^- \rangle\rangle - \frac{1}{2}\big(\langle\langle S_l^+ S_i^z; S_m^- \rangle\rangle + \langle\langle S_i^z S_l^+; S_m^- \rangle\rangle\big)\right) \\
&+\sum_r \tilde{J}_{rl}\left(\langle\langle S_r^+ S_l^z; S_m^+ \rangle\rangle - \frac{1}{2}(\langle\langle S_l^+ S_r^z; S_m^- \rangle\rangle + \langle\langle S_r^z S_l^+; S_m^- \rangle\rangle)\right) \\
&-2\sum_{i,j} K_{ijl}(\frac{1}{2} - \langle\rho\rangle)\cos\nu + \frac{1}{2}\big(\langle\langle S_l^+ S_i^z; S_m^- \rangle\rangle + \langle\langle S_i^z S_l^+; S_m^- \rangle\rangle\big) \\
&-D\big(\langle\langle S_l^+ S_i^z; S_m^- \rangle\rangle + \langle\langle S_i^z S_l^+; S_m^- \rangle\rangle\big) - h\langle\langle S_l^+; S_m^- \rangle\rangle \,.
\end{aligned}
\tag{3.29}
$$

This equation is still exact. However, it cannot be solved exactly since there exist higher order Green's functions on the right-hand side. There are several decoupling methods, mean field approximation (MFA) where fluctuations are completely ignored, Hartree-Fock approximation and random phase approximation (RPA), also known as the Tyablikov approximation. Based on RPA assumption we allow to neglect the correlations between S^+ on one lattice site and S^z on another lattice site and replace the operator S_i^z by its thermodynamic expectation value $\langle S_i^z \rangle$ [76]

$$\langle\langle S_l^z S_i^+; S_m^- \rangle\rangle \approx \langle S_l^z \rangle\langle\langle S_i^+; S_m^- \rangle\rangle \,. \tag{3.30}$$

This decoupling procedure is the aspect of the theory. The justification is the acceptive results obtained with this method. Further, we can assume translational

symmetry of the lattice. As a result, all averages are independent of the lattice site index

$$\langle S_i^z \rangle = \langle S^z \rangle \,. \tag{3.31}$$

Also because of translational invariance we can Fourier transform our Green's functions with respect to the reciprocal lattice. Thus, Eq. (3.29) simplifies to

$$E^m \langle\langle S_q^+; S_q^- \rangle\rangle = 2\langle S_z \rangle + \bigg(\langle S_z \rangle \big(J_0 - J_q - \tilde{J}_0 + \tilde{J}_q - D \big) $$
$$- 2K_0(\frac{1}{2} - \langle \rho \rangle)\langle S_z \rangle \cos\nu - h \bigg) \langle\langle S_q^+; S_q^- \rangle\rangle \,. \tag{3.32}$$

Therefore

$$G_q^m(E) = \frac{2M}{E - E^m(\mathbf{q})} \,, \qquad M = \langle S_z \rangle, $$
$$E^m(\mathbf{q}) = M\big[J_0 - J_\mathbf{q} + \tilde{J}_\mathbf{q} - \tilde{J}_0 - D - 2K_0 P \cos\nu) \big] - h \,. \tag{3.33}$$

Here E^m is the spin-wave energy of the magnetic subsystem modified by the magnetoelectric coupling K_0. Due to MEC the spectrum includes both the magnetization M as well as the polarization P. Following Callen's calculation [77] for arbitrary spin S, one can write

$$\langle S_q^z \rangle = SB_s(\beta, S, E_m), \tag{3.34}$$

where B_s is the well known Brillouin function. Hence the magnetization reads

$$M = \frac{1}{N} \sum_\mathbf{q} \big[(S+0.5)\coth[(S+0.5)\beta E^m(\mathbf{q})] - 0.5\coth(0.5\beta E^m(\mathbf{q})) \big] \,. \tag{3.35}$$

The analysis of the ferroelectric subsystem is more complex. Different to the magnetic case the Green's function is a matrix abbreviated as $G_{lm}^{(f)}(t)$

$$\begin{pmatrix} \langle\langle b_l; b_m^\dagger \rangle\rangle & \langle\langle b_l; b_m \rangle\rangle \\ \langle\langle b_l^\dagger; b_m^\dagger \rangle\rangle & \langle\langle b_l^\dagger; b_m \rangle\rangle \end{pmatrix} \equiv \begin{pmatrix} G_{lm}^{(f)11} & G_{lm}^{(f)12} \\ G_{lm}^{(f)21} & G_{lm}^{(f)22} \end{pmatrix} \,.$$

Using RPA we get this matrix equation

$$E^f \cdot \begin{pmatrix} G_q^{(f)11} & G_q^{(f)12} \\ G_q^{(f)21} & G_q^{(f)22} \end{pmatrix} = \begin{pmatrix} 2P & 0 \\ 0 & -2P \end{pmatrix} + \begin{pmatrix} \varepsilon_q^{11} & \varepsilon_q^{12} \\ \varepsilon_q^{21} & \varepsilon_q^{22} \end{pmatrix} \begin{pmatrix} G_q^{(f)11} & G_q^{(f)12} \\ G_q^{(f)21} & G_q^{(f)22} \end{pmatrix}, \tag{3.36}$$

where

$$\varepsilon_q^{11} = 2\Omega \sin\nu + J_0' P \cos^2\nu - K_0 \cos\nu M^2 - \frac{1}{2} J_q' P \sin^2\nu + \mu E \cos\nu,$$
$$\varepsilon_q^{12} = -\frac{1}{2} J_q' P \sin^2\nu, \tag{3.37}$$
$$\varepsilon_q^{21} = -\varepsilon_q^{12} \qquad \varepsilon_q^{22} = -\varepsilon_q^{11} \,.$$

Eq. (3.36) reads in components

$$EG^{(f)\alpha\beta}(q, E) = I_{\alpha\beta} + \sum_\gamma \Gamma^{\alpha\gamma} G^{(f)\gamma\beta}(q, E) \,, \tag{3.38}$$

which results in

$$G^{(f)\mu\beta}(q, E) = \sum_{\alpha}(X^{-1})^{\alpha\mu}I_{\alpha\beta}, \tag{3.39}$$

where X is

$$X = \begin{pmatrix} E - \varepsilon_q^{11} & -\varepsilon_q^{12} \\ -\varepsilon_q^{21} & E - \varepsilon_q^{22} \end{pmatrix}, \tag{3.40}$$

and

$$X^{-1} = \frac{1}{detT} \cdot \begin{pmatrix} E - \varepsilon_q^{22} & \varepsilon_q^{21} \\ \varepsilon_q^{12} & E - \varepsilon_q^{11} \end{pmatrix}. \tag{3.41}$$

Now, we are able to calculate the Green's function components. For instance $G_q^{(f)11}$ is

$$G_q^{(f)11} = \frac{P[E - \varepsilon_q^{22}]}{(E - \varepsilon_q^{11})(E - \varepsilon_q^{22}) - (\varepsilon_q^{12}\varepsilon_q^{21})}. \tag{3.42}$$

By defining

$$E_{1,2}(\mathbf{q}) = \frac{(\varepsilon_q^{11} + \varepsilon_q^{22}) \pm \sqrt{(\varepsilon_q^{11} + \varepsilon_q^{22})^2 - 4(\varepsilon_q^{11}\varepsilon_q^{22} - \varepsilon_q^{12}\varepsilon_q^{21})}}{2}, \tag{3.43}$$

we write $G_q^{(f)11}$ as

$$\begin{aligned} G_q^{(f)11} &= \frac{P[E - \varepsilon_q^{22}]}{(E - E_1)(E - E_2)}, \\ G_q^{(f)11} &= P\left(\frac{\epsilon_q}{E - E_1} - \frac{\epsilon_q'}{E - E_2}\right), \end{aligned} \tag{3.44}$$

$$\begin{aligned} \epsilon_q &= \frac{E_1 - \varepsilon_q^{22}}{E_1 - E_2} = \frac{\sqrt{(\varepsilon_q^{11})^2 - (\varepsilon_q^{12})^2} - \varepsilon_q^{22}}{2\sqrt{(\varepsilon_q^{11})^2 - (\varepsilon_q^{12})^2}} = \frac{\varepsilon_q^{11}}{2E^f(q)} + \frac{1}{2}, \\ \epsilon_q' &= \frac{E_2 - \varepsilon_q^{22}}{E_1 - E_2} = -\frac{\sqrt{(\varepsilon_q^{11})^2 - (\varepsilon_q^{12})^2} - \varepsilon_q^{22}}{2\sqrt{(\varepsilon_q^{11})^2 - (\varepsilon_q^{12})^2}} = \frac{\varepsilon_q^{11}}{2E^f(q)} - \frac{1}{2}. \end{aligned} \tag{3.45}$$

$E^f(\mathbf{q}) = \sqrt{(\varepsilon_q^{11})^2 - (\varepsilon_q^{12})^2} \equiv E_1 \equiv -E_2$. Based on the definition of spectral density

$$S_q(E) = -\frac{1}{\pi}ImG_q^{(f)}(E + i\eta) = P\left(\epsilon_q\delta(E - E_1) - \epsilon_q'\delta(E - E_2)\right), \tag{3.46}$$

one obtains the correlation function according to

$$\langle b_i^\dagger b_j \rangle = \frac{1}{N}\sum_q \exp(-iq(R_i - R_j))\int \frac{S_q(E)}{\exp(\beta E) - 1}dE. \tag{3.47}$$

We find,

$$\langle b_i^\dagger b_i \rangle = \frac{P}{N}\sum_q \left(\frac{\epsilon_q}{\exp(\beta E_1) - 1} - \frac{\epsilon_q'}{\exp(\beta E_2) - 1}\right). \tag{3.48}$$

Inserting Eq. (3.45) in Eq. (3.48) we end up with

$$\langle b_i^\dagger b_i \rangle = \frac{P}{N} \sum_{\mathbf{q}} \left(\frac{\varepsilon_q^{11}}{E^f(\mathbf{q})} \coth \frac{\beta E^f(\mathbf{q})}{2} - 1 \right) \equiv \langle \rho \rangle . \tag{3.49}$$

By the definition $P = \frac{1}{2} - \langle \rho \rangle$, the polarization reads

$$P = \frac{1}{\frac{2}{N} \sum_{\mathbf{q}} \left(\frac{\varepsilon_{\mathbf{q}}^{11}}{E^f(\mathbf{q})} \coth \frac{\beta E^f(\mathbf{q})}{2} \right)} . \tag{3.50}$$

To find M and P for the system we obtain the angle ν based on $\langle [b_q, H] \rangle = 0$. This results in the equation $A\langle b_q \rangle + B\langle b_q^\dagger \rangle + C = 0$ where A, B and C are coefficients. We know $\langle b_q \rangle = -\langle b_q^\dagger \rangle$. Further, $\langle b_q \rangle = 0$ is required leading to $C = 0$.

$$C = (-2\Omega \cos \nu + \frac{1}{2} P J_0' \sin \nu \cos \nu) P - \frac{1}{2} K_0 P \sin \nu \langle s^z \rangle^2 + \mu P E \sin \nu , \tag{3.51}$$

and

$$P \cos \nu (-2\Omega + \frac{1}{2} P J_0' \sin \nu) = \frac{1}{2} P K_0 \sin \nu \langle s^z \rangle^2 + \mu E P \sin \nu . \tag{3.52}$$

Considering $P \cos(\nu) \equiv \tilde{P}$, we have

$$\tilde{P}(-2\Omega + \frac{J_0'}{2} \tan \nu \tilde{P}) = \tilde{P}(\frac{K_0}{2} M^2 + \mu E) \tan \nu , \tag{3.53}$$

$$\tan \nu = \frac{4\Omega}{J_0' \tilde{P} - K_0 M^2 + 2\mu E} . \tag{3.54}$$

The angle ν is determined in such a manner that the polarization is zero provided the system is within the range $T_C \leq T \leq T_N$ and the magnetoelectric coupling is not relevant. This technical trick reflects the improper nature of the ferroelectricity. We replace P with $\tilde{P}$ in all related equations.
After solving the above equations we find the polarization using $P = \frac{\tilde{P}}{\cos \nu}$. Considering bcc structure, the q-dependency of couplings are as follows

$$\begin{aligned}
J_q &= zJ \cos(\frac{1}{2} q_x a) \cos(\frac{1}{2} q_y a) \cos(\frac{1}{2} q_z a), \\
\tilde{J}_q &= \frac{1}{3} z' \tilde{J} (\cos(2 q_x a) + \cos(2 q_y a) + \cos(2 q_z a)), \\
J_q' &= zJ' \cos(\frac{1}{2} q_x a) \cos(\frac{1}{2} q_y a) \cos(\frac{1}{2} q_z a) ,
\end{aligned} \tag{3.55}$$

where $z = 8$ is the number of nearest neighbors and $z' = 6$ is the number of next nearest neighbors. Furthermore, we have $J_0 = zJ$, $\tilde{J}_0 = z'\tilde{J}$ and $J_0' = zJ'$ where

$\tilde{J} = \alpha J$. Knowing T_C and T_N, one can find the approximate value for the exchange interaction based on the following analytical formulas

$$k_B T_N = \frac{S(S+1)zJ}{3F(\frac{\tilde{J}}{J})},$$
$$\frac{J'_0}{4\Omega} = 1/N \frac{\sum_k 1 - 1/2\gamma_k}{\sqrt{1-\gamma_k}} \coth(\frac{\Omega}{T}\sqrt{1-\gamma_k}). \tag{3.56}$$

Assuming a lattice constant $a = 1$ we find

$$F(\alpha) = \frac{v}{(2\pi)^3} \int_{-\pi}^{\pi} \frac{d^3q}{\left(1 - \frac{J(q)}{J(0)}\right) - \frac{z'}{z}\alpha\left(1 - \frac{\tilde{J}(q)}{\tilde{J}(0)}\right)} , \quad \alpha = \frac{\tilde{J}}{J}. \tag{3.57}$$

Here we find the energy spectrum together with the magnetization and polarization of the system. In next sections we use these analytical results to predict and analyze the behavior of the different multiferroics systems by choosing appropriate Hamiltonians. In section 3.3, we demonstrated that the analytical results obtained in this section are relevant for the magnetoelectric behavior in rare-earth manganite. Moreover, by extending these calculations the role of spin-phonon coupling in this group of materials will be studied. Furthermore, a realistic model for such complicated structures will be presented. We also show how one can insert impurities into multiferroic Hamiltonian and we discuss the relevant consequences on the phase diagram of $MnWO_4$. predict

3.3. The magnetoelectric effect in rare-earth manganite

There is currently a great effort in understanding the microscopic nature of the coupling between ferroelectric and magnetic ordering in a large class of manganese oxides known as $RMnO_3$ and RMn_2O_5, with rare-earth R = Y, Tb, Dy, etc. [52]. Regardless the innovative aspects, the underlying detailed mechanism of the multiferroics is under a permanent debate for many years [1, 59, 65]. Although the majority of magnetoelectric effects observed in rare-earth manganites are best described by Dzyaloshinskii-Moriya interaction, the appearance of a nontrivial polarization P in magnetic phase of RMn_2O_5 (R = Tb, Y, Dy, and Bi), suggesting that a different mechanism is involved in the interaction between the ferroelectricity and magnetism.

Based on experimental results, RMn_2O_5 belong to the space group Pbam, which meets the spatial-inversion symmetry and thus would exclude ferroelectricity because of the lack of this symmetry breaking. One known microscopic mechanism to invoke ferroelectricity include lattice distortion (exchange-striction) and redistribution of electron density in response to the spin ordering. Such processes occur locally in all magnetic materials. However, only when a spin ordering breaks the inversion symmetry these local electric dipoles sum up to a macroscopic electric polarization. To explain the observed ferroelectricity in RMn_2O_5 theoretically one may expect that at low temperatures a lattice distortion occurs, reducing the crystal symmetry to Pb21m and giving rise to a polarization along the b-axis, but until now no direct evidence has been presented. The nature of ferroelectricity is studied based on calculations of the ferroelectric polarization predicted by different microscopic coupling mechanisms. So far, two distinct scenarios have been proposed which already discussed in section 3.1.

Many of the recently discovered multiferroic materials, such as $TbMnO_3$, show cycloidal spin order attributed to frustration due to competing interactions [53, 78]. In these systems, non-collinear magnetic orders break inversion symmetry and give rise to polarization via the antisymmetric Dzyaloshinskii-Moriya interaction. On the other hand, a configuration of collinear spins breaking the inversion symmetry can induce polarization via a mechanism based on the isotropic Heisenberg exchange and a magnetostrictive coupling of spins to a polar lattice mode. First-principles calculations of the ground state as well as structural, electronic, and magnetic properties of multiferroic $TbMn_2O_5$ by Wang et al. [79] reveal that the ferroelectricity in $TbMn_2O_5$ is driven by the non-centrosymmetric antiferromagnetic ordering, without invoking the spin-orbit coupling and non-collinear spins. Similar arguments are also presented by [80, 81]. As a result, the material should possess a strong MEC. The kind of MEC is responsible for the sensitivity of the system to applied magnetic fields and may lead to a new class of functional materials. Moreover, the primary order parameter in this type of multiferroics is magnetization and the electrical polarization is at least an order of magnitude lower than in proper ferroelectrics. In spite of a broad variety of effects occurring in multiferroic materials, a detailed analysis of underlying quantum models is still lacking. Therefore our goal is to propose and to analyze a microscopic model for rare-earth manganites.

3.3.1. Structure of RMn$_2$O$_5$

The crystal structures of RMn$_2$O$_5$ were first well established by Bertaut et al. [82] and independently by Abrahams and Bernstein [83] and then later by many other authors [80, 81, 84–86]. At high temperatures, these isostructure insulators belong to the orthorhombic space group of Pbam, with four RMn$_2$O$_5$ formula units per primitive cell, where Mn^{3+} (S = 2) ions surrounded by oxygen pyramids and Mn^{4+} (S = 3/2) ions surrounded by oxygen octahedra (Fig. 3.1). Both the Mn^{4+}, Mn^{3+} and in some components R^{3+}, have magnetic moments, giving rise to complex magnetic orderings.
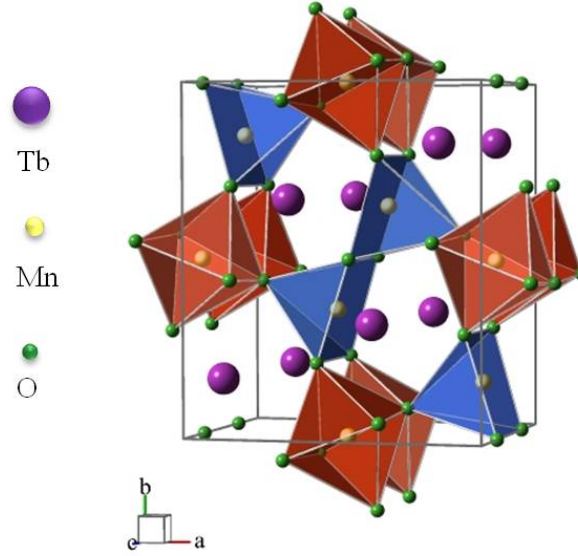
Figure 3.1. – A view of the crystal structure of TbMn$_2$O$_5$ along the z-axis. Sketched using [87].

3.3.2. Simplified structure and analytical representation

Here we follow the mechanism suggested by [81] which can be successfully applied to a large class of ferroelectric materials. The Hamiltonian H_{m} consists of the isotropic Heisenberg exchange interaction J and $\tilde{J}$, which represent NN and NNN couplings in Eq. (3.2). In this part, we neglect the effect of single-ion anisotropy. As pointed out in [88], compare also [89], the magnetic excitations in the multiferroic material are different. Within a numerical simulation, the authors have identified five different exchange coupling parameters appearing in the Heisenberg spin Hamiltonian. Following [80], the exchange interactions between neighboring Mn^{3+} and Mn^{4+} ions are all antiferromagnetic. As a result, magnetic frustration must exist in the smallest closed loop of Mn spins consisting of five magnetic ions. Therefore, zigzag chains of frustrated spins exist in a direction parallel to the a-axis as it is illustrated in Fig. 3.2(a). In the framework of an analytical calculation, we have simplified the model as depicted in Fig. 3.2(b). It comprises the frustrated magnetic subsystem represented by Eq. (3.2).
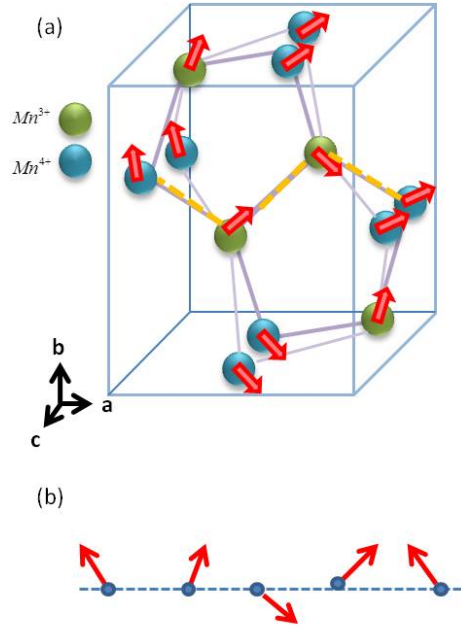
Figure 3.2. – (a) Mn-spin configuration in RMn_2O_5 structure showing frustration, (b) Typical sketch of a frustrated spin system with nearest neighbor ferromagnetic interaction and next nearest neighbor antiferromagnetic coupling.

The two different couplings J and $\tilde{J}$ in this equation reflect the competition between different magnetic orders which leads to frustration. The further analysis is done taking into account the q dependency of couplings, see Eq. (3.55). Let us make a technical remark. Although the geometry of the lattice of RMn_2O_5 is quite complex, we have used a bcc structure for simplicity. The reason is that in our approach the geometrical structure is primarily included by the wave vector dependency of the coupling parameters. Moreover, numerical simulations indicate that the results will not change drastically using an orthorhombic structure.

The ferroelectric behavior is modeled by the Ising model in a transverse field (Eq. (3.4)). The last term in Eq. (3.1) describes the coupling between the magnetic and the ferroelectric subsystems. Here, the coupling between the ferroelectric and the magnetic subsystems includes a quadratic coupling in the magnetic order parameter and a linear one in the ferroelectric order parameter. The underlying physical mechanism of the coupling is that the cooperative alignment of magnetic moments at a certain temperature is the reason for the polarization. The excitation spectrum offers a gap due to the MEC. The model will be extended by inclusion the coupling of external electric and magnetic fields. We demonstrate that the magnetization is affected by an electric field and the polarization by the corresponding magnetic field.

3.3.3. Excitation spectrum, magnetization and polarization in manganites

In this section the numerical results of our theoretical calculations will be presented based on the Green's functions calculation in section 3.2. The following model pa-

rameters are used for the ferroelectric and the magnetic subsystem: $T_C = 38$ K, T_N $= 43$ K, $J_0' = 75$ K, $\Omega = 0.2$ K, $J_0 = 54$ K, $\tilde{J} = 18.5$ K, $K_0 = -7$ K, $s = 1/2$. The spin assume to be $S = 2$. These values are appropriate for $TbMn_2O_5$ [81]. The analysis is focused on the magnetization obtained by Eq. (3.35), the polarization, Eq. (3.50), and the spin-wave frequency according to Eq. (3.33). The temperature

(a)   (b)
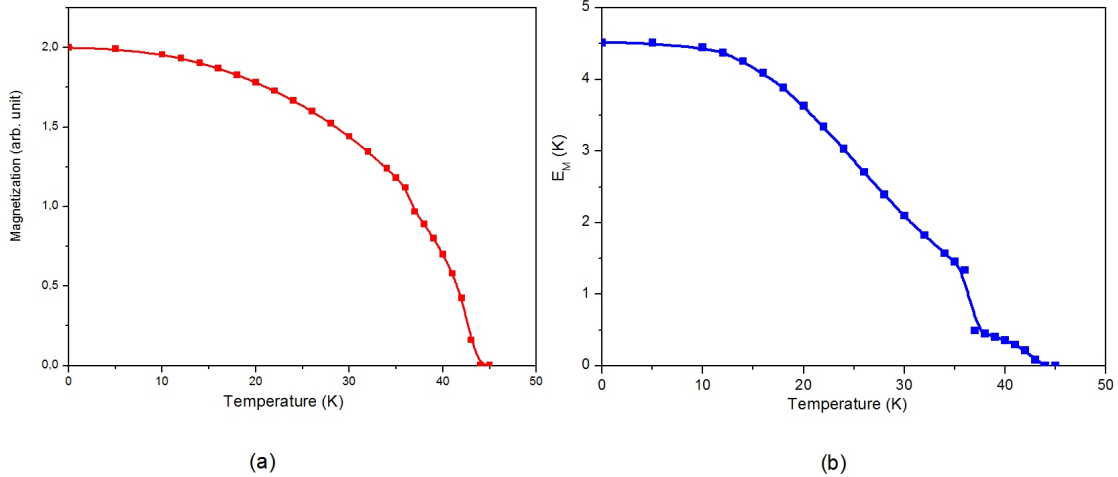
Figure 3.3. – Temperature dependence of the (a) Magnetization M (b) Spin-wave energy E^m for zero wave vector with $J_0' = 75$ K and $K_0 = -7$ K.

dependence of the magnetization M is shown in Fig. 3.3(a). Notice that the calculation of the magnetization is based on the spin-wave energy of the magnetic subsystem E^m which is given in Eq. (3.33). The temperature-dependent spin-wave energy E^m at zero wave vector is shown in Fig. 3.3(b). In both figures 3.3(a) and 3.3(b) the MEC between the two order parameters is manifested as a kink at the ferroelectric phase transition temperature T_C. This discontinuity in M and E^m characterizes the mutual influence between ferroelectric and magnetic ordering. A simple physical picture behind this effect could be related to an energy transfer from the magnetic phase to the polar phase. This energy is necessary to establish the new ferroelectric phase. Since $T_C < T_N$, the electric subsystem is not able to influence the magnetic one above T_C. The two phases coexist only below T_C. Such a cusp-like anomaly at the ferroelectric critical temperature is obtained experimentally for example in the magnetic susceptibility [90] in $TbMn_2O_5$ and in the magnetization [91–93] of RMn_2O_5 and orthorhombic $RMnO_3$.
The kink is a strong indication for the magnetoelectric effect. The measured specific heat shows kinks at the critical temperatures T_C and T_N in $DyMn_2O_5$ [94]. As shown in Fig. 3.3(b) the magnetic excitation offers a novel softening behavior around T_C. The polarization P decreases with increasing temperature and vanishes at the critical temperature T_C which is depicted in Fig. 3.4. The polarization offers a phase transition at T_C where above T_C the system is disordered and reveals no ferroelectric order. Notice that the spontaneous polarization P exists below T_C where the system is likewise magnetically ordered. Such a behavior is characteristic for multiferroics. The effect and the relevance of the magnetoelectric coupling K_0, introduced in Eq. (3.7),
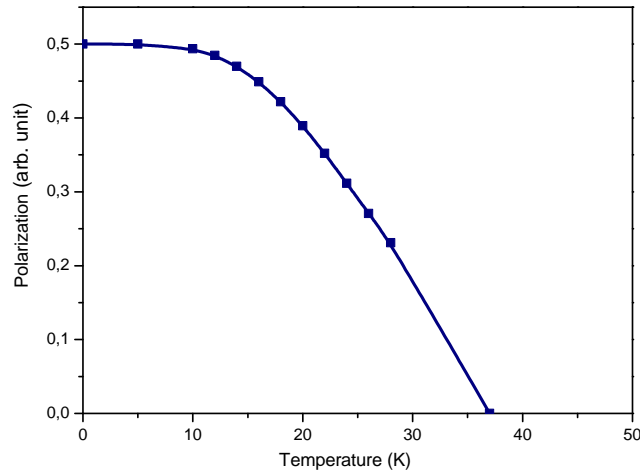
Figure 3.4. – Dependence of the polarization P on the temperature for $J_0' = 75$ K and $K_0 = -7$ K.
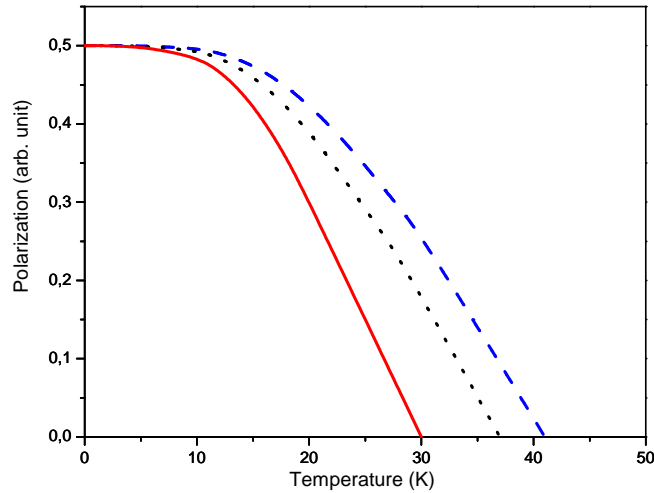
Figure 3.5. – Dependence of the polarization P for different magnetoelectric couplings $K_0 = -3$ K (solid); $K_0 = -7$ K (dot); $K_0 = -10$ K (dash); for $J_0' = 75$ K.

on the polarization P is demonstrated in Fig. 3.5. In case the coupling strength K_0 is varied the polarization is also changed. With increasing coupling K_0 the polarization P is enhanced and the phase transition temperature T_C grows, too. Consequently the kink in the magnetization M and energy E^m at T_C is shifted towards T_N, while for larger K_0 it vanishes, compare Fig. 3.6(a) and Fig. 3.6(b). The magnetic phase transition temperature T_N remains unchanged by K_0. The spin-wave energy $E^m(\mathbf{q})$ is also changed by the magnetoelectric coupling K_0. The result for a fixed temperature is shown in Fig. 3.7.

In the same manner the spin-wave dispersion at zero wave vector is varied for different
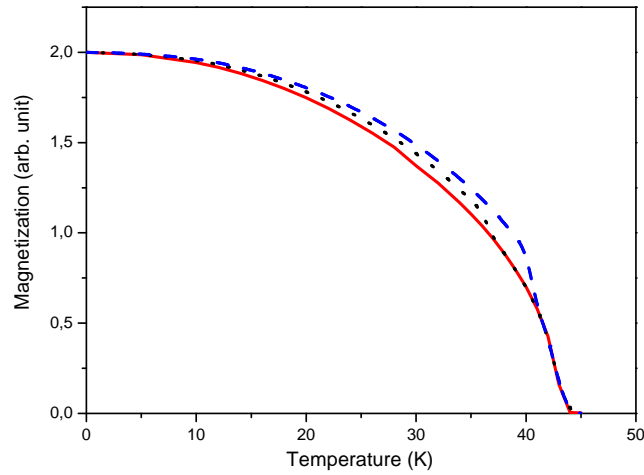
(a)
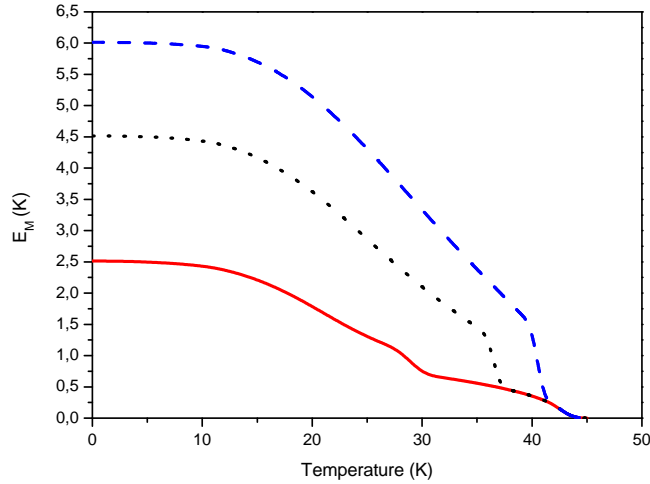
(b)

Figure 3.6. – Temperature dependence of the (a) Magnetization M and (b) Spin-wave energy E^m for different magnetoelectric couplings $K_0 = -3$ K (solid); -7 K (dot); -10 K (dash).

MEC which is shown in Fig. 3.6(b). The dispersion relation $E^m(\mathbf{q})$ increases with the wave vector $\mathbf{q}$, see Fig. 3.7. If the MEC is absent the energy is typically zero at $q = 0$ (solid curve). Due to the non-vanishing MEC the system develops an energy gap at zero wave vector which increases with increasing of the magnetoelectric coupling K_0, see dot and dash curve in Fig. 3.7. The MEC breaks the continuous symmetry of the magnetic subsystem and the related Goldstone mode becomes massive, i.e. the dispersion relation reveals a gap at zero wave vector.
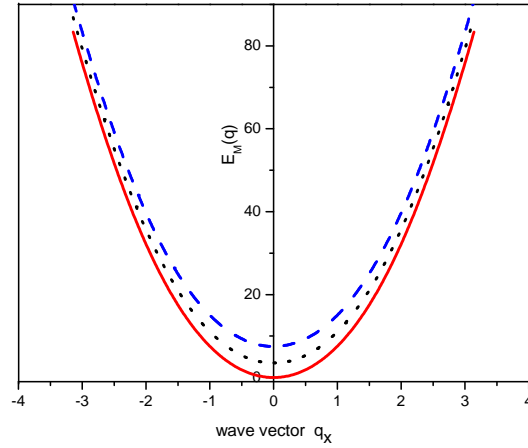
Figure 3.7. – Wave vector dependence of the spin-wave energy E^m for different magnetoelectric coupling constant: $K_0 = 0$ K (solid); -7 K (dot); -10 K (dash).

3.3.4. Observation of magnetoelectric effect

One advantage of multiferroic material is the possibility to trigger the polarization by an external magnetic field h and the magnetization by an external electric field E. Therefore our Hamiltonian Eq. (3.1) has to be supplemented by external field. The couplings of both external fields to the spins and to the pseudospins, are linear, respectively. The strong MEC can be seen by studying the influence of an applied electric field on the magnetic properties, see Fig. 3.8. It is shown that the increase of
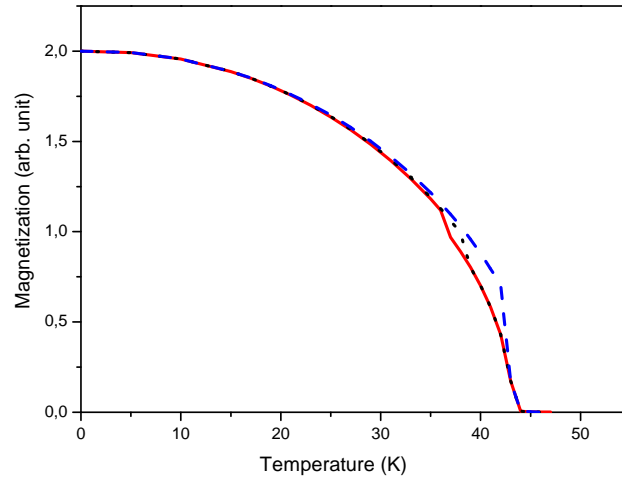
Figure 3.8. – Temperature dependence of the magnetization M for different electric fields E: $E = 0$ K (solid); $E = 1$ K (dot); $E = 5$ K (dash).

the electric field E leads to an enhancement of the magnetization M mainly in the temperature range $T_C \leq T \leq T_N$. Whereas T_N remains unchanged for small couplings

K_0, the ferroelectric phase transition temperature T_C is enhanced. The kink is shifted to higher temperatures, near to T_N, and for larger E-values the kink disappears. The reason is that the electric field shifts the phase transition temperature T_C to higher values and the distance between T_C and T_N shrinks. The saturation magnetization remains likewise unchanged indicating that the magnetic domains do not increase in size. From here we conclude that the domains are just reoriented by the electric field. The calculations suggest that for sufficient high electric field strengths the polarization becomes larger as the magnetization and hence $T_C > T_N$, then the kink disappears. This theoretical finding should be confirmed by experiments with higher electric fields. Here we present the results for small electric fields. The influence of an
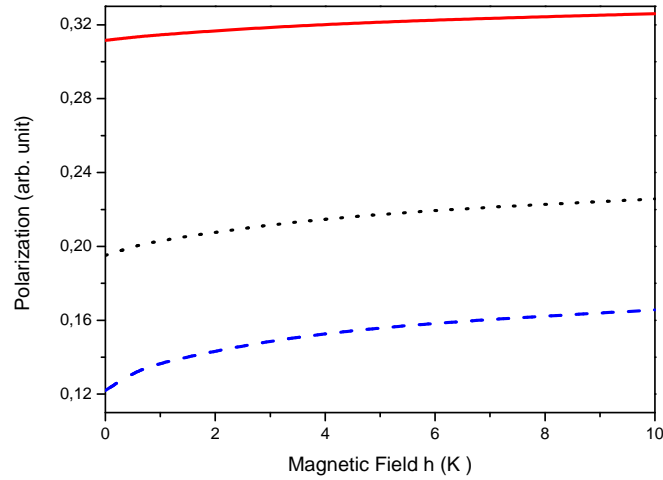
Figure 3.9. – Magnetic field dependence of the polarization P for different temperatures: $T = 24$ K (solid); $T = 30$ K (dot); $T = 35$ K (dash).

external magnetic field h on the polarization P is shown in Fig. 3.9. The polarization is enhanced with an increasing external magnetic field h. The higher the temperatures the stronger are the changes, compare blue dash curve in Fig. 3.9. Such a behavior is in agreement with the experimental data for $TmMn_2O_5$ [95], $MnWO_4$ [96] and of orthorhombic $YMnO_3$ [97]. The strong MEC is evident in $TbMn_2O_5$ [55], the upward jump in the dielectric constant at T_C transition is pushed to higher temperatures if a magnetic field is applied. Using our method we find that the ferroelectric phase transition temperature T_C and the related excitation E^f increase with increasing magnetic field h. Hence the electric phase in the multiferroic compounds RMn_2O_5 can be controlled by an external magnetic field and the dielectric properties turn out to be highly susceptible to such applied fields.

3.4. Phonon excitations in multiferroic RMn$_2$O$_5$

Since in the past phonons and their coupling with other degrees of freedom have played a crucial role in understanding classic ferroelectrics, one should expect that they have a great impact on magnetoelectric multiferroics. Recent investigations using Raman and infrared (IR) spectroscopy, by transmittance and reflectance measurements, have demonstrated the importance of phonon effects in multiferroics. There is an experimental evidence for a strong spin-phonon coupling in RMn$_2$O$_5$ [98, 99]. The experimental results show pronounced phonon anomalies around the magnetic and electric phase transition temperatures [93, 100–104]. These anomalies are attributed to the multiferroic character of the materials. Raman phonons in RMnO$_3$ orthorhombic and hexagonal manganites have been studied by [105] as a function of the rare-earth ion and the temperature.

The sign and the magnitude of such anomalous phonon shifts seem to be correlated with the ionic radius of the multiferroic RMn$_2$O$_5$ [101]. The phonon excitation becomes a zone-center transverse optical phonon mode known as soft mode in case that R is Bi and shows significant enhancement in the phonon frequency (phonon hardening) if the rare-earth part is Dy. An intermediate behavior is observed for Eu. Based on the temperature dependence of the far-IR transmission spectra of multiferroic YMn$_2$O$_5$ and TbMn$_2$O$_5$ single crystals, the occurrence of electromagnons was reported in RMn$_2$O$_5$ compounds by [106]. The phonon energy and its damping are different for diverse compounds. So varying selection rules for electromagnons in RMn$_2$O$_5$ and RMnO$_3$ suggest different magnetoelastic coupling mechanisms in the multiferroic systems. Molecular-spin dynamic studies of electromagnons in RMn$_2$O$_5$ are discussed in [107]. The so-called shell model lattice dynamic calculations are proposed in [108] for RMn$_2$O$_5$ (R = Ho, Dy) materials. Here spin-phonon couplings have been taken into account. Theoretically the influence of phonons is studied in [109].

The exchange-striction induces a biquadratic interaction between spins and transverse phonons. More recently, the spin-phonon coupling in multiferroic Mn compounds were analyzed in a classical spin model [110]. The new aspect focused on in the present section is the calculation of the phonon spectrum within a microscopic model for RMn$_2$O$_5$.

3.4.1. The model Hamiltonian considering phonon effects

The Hamiltonian of the whole system is introduced in Eq. (3.1). The magnetic part, H$_m$, and the MEC term are Eqs. (3.2) and (3.7). Due to the complexity of the manganites the ferroelectric behavior is described within our analytical approach by both order-disorder and displacive type aspects. The order-disorder properties are characterized by pseudospins in the frame of an Ising model in a transverse field [26], while the displacive behavior is characterized by lattice distortions. Therefore, H$_f$ is

$$H_\mathrm{f} = H_\mathrm{ph} + H_\mathrm{tim}\,,$$

$$H_{\mathrm{ph}} = \frac{1}{2} \sum_k (P_k P_{-k} + \omega_{(0)k}^2 Q_k Q_{-k})$$

$$+ \frac{1}{3!} \sum_{k,k_1} B(k, k_1) Q_k Q_{-k_1} Q_{k_1 - k} \tag{3.58}$$

$$+ \frac{1}{4!} \sum_{k,k_1,k_2} A(k, k_1, k_2) Q_{k_1} Q_{k_2} Q_{-k-k_2} Q_{-k_1+k},$$

$$H_{\mathrm{tim}} = -\frac{1}{2} \sum_{i,j} J'_{ij} B_i^z B_j^z - 2\Omega \sum_i B_i^x. \tag{3.59}$$

The first part of H_{ph} represents the harmonic part of the lattice distortions in terms of the normal coordinate Q_k, the momentum P_k and the harmonic phonon frequency $\omega_{(0)k}$ of the lattice mode with wave vector k. The remaining terms describe the anharmonic interactions, where the third order coupling is given by $B(k, k_1)$ and the quartic one by $A(k, k_1, k_2)$. In terms of phonon creation and annihilation operators the normal coordinate and the momentum are expressed by

$$Q_k = (2\omega_{(0)k})^{-1/2} (a_k + a_{-k}^\dagger) \ , \quad P_k = i(\frac{\omega_{(0)k}}{2})^{1/2} (a_k^\dagger - a_{-k}). \tag{3.60}$$

The ferroelectric subsystem is considered typically in a rotated frame as we discussed before. The MEC in Eq. (3.7) describes the direct influence of the magnetic order parameter on the secondary polar order parameter. However both subsystems are simultaneously influenced by lattice distortions. Hence the model has to be completed by spin-phonon interactions. Such a spin-phonon coupling had been already discussed within the pseudospin approach in [26]. As pointed out, the main effect comes from the modulation of an internal crystal field. Following that approach and former studies for ferroelectric thin films in [111] as well as for multiferroic materials in [112], the pseudospin-phonon coupling H_{fph} can be expressed in terms of normal displacement coordinates Q, compare Eq. (3.58). The total interaction is written in the form

$$\begin{aligned} H_{\mathrm{fph}} = & -\sum_k F^{(f)}(k) Q_k B_{-k}^z - \frac{1}{2} \sum_{kk_1} R^{(f)}(k, k_1) Q_k Q_{-k_1} B_{k_1-k}^z, \\ H_{\mathrm{mph}} = & -\sum_k F^{(m)}(k) Q_k S_{-k}^z - \frac{1}{2} \sum_{kk_1} R^{(m)}(k, k_1) Q_k Q_{-k_1} S_{k_1-k}^z. \end{aligned} \tag{3.61}$$

Here the first term H_{fph} models the coupling between the ferroelectric order parameter and the phonons, while the second term H_{mph} is responsible for the coupling between phonons and magnetic spins. We are aware that higher order couplings, quadratic in spins or pseudospins, can be also taken into account. Such terms seem to be irrelevant in searching the occurrence of a polarization due to magnetic ordering. The complete Hamiltonian will be analyzed in the subsequent section using Green's functions. The different terms denote spin-phonon interaction effects arising from the first and second powers in the relative displacement of lattice site away from equilibrium. $F(q) = \bar{F}(q)/(2\omega_q^0)^{1/2}$ and $R(q, p) = \bar{R}(q, p)/(2\omega_q^0)^{1/2}(2\omega_p^0)^{1/2}$ designate the amplitudes for coupling of phonons to the spin excitations in first and second order, respectively.

3.4.2. Green's functions and phonon excitation spectrum

Similar to the calculation in section 3.2, for the magnetic subsystem one gets

$$
\begin{aligned}
G_q^m(E) =& \frac{2M}{E - E^m(\mathbf{q})} \\
E^m(\mathbf{q}) =& M\left[J_0 - J_q + \tilde{J}_q - \tilde{J}_0 - K_0\cos\nu\left(\frac{1}{2} - \langle\rho\rangle\right)\right] \\
&+ F^{(m)}(0)\langle Q\rangle + R^{(m)}(0)\langle Q^2\rangle .
\end{aligned}
\tag{3.62}
$$

Here E^m is the spin-wave energy of the magnetic subsystem modified by the magnetoelectric coupling K_0 and the magnetic spin-phonon interaction $\mathrm{F}^{(m)}$ and $\mathrm{R}^{(m)}$. Similarly, additional terms would appear in the energy components of Eq. (3.37)

$$
\begin{aligned}
\varepsilon_q{}^{11} =& 2\Omega\sin\nu + J_0'P\cos^2\nu - K_0\cos\nu M^2 - \frac{1}{2}J_q'P\sin^2\nu + \\
&+ F^{(f)}\langle Q\rangle\cos\nu + \frac{1}{2}R^{(f)}\langle Q^2\rangle\cos\nu, \\
\varepsilon_q{}^{12} =& -\frac{1}{2}J_q'P\sin^2\nu , \quad \varepsilon_q{}^{21} = -\varepsilon_q{}^{12} \quad , \quad \varepsilon_q{}^{22} = -\varepsilon_q{}^{11} .
\end{aligned}
\tag{3.63}
$$

According to section 3.2, the pseudospin excitation energy is given by

$$
E^f(\mathbf{q}) = \sqrt{(\varepsilon_q^{11})^2 - (\varepsilon_q^{12})^2} .
\tag{3.64}
$$

These equations lead to the same definition for polarization and magnetization (Eq. (3.50) and Eq. (3.35)) with some modifications in the excitation energies.
The phononic part is also described by a Green's function matrix denoted as $G_q^{(\mathrm{ph})}(t)$

$$
\begin{pmatrix} \langle\langle a_q; a_q^\dagger\rangle\rangle & \langle\langle a_q; a_q\rangle\rangle \\ \langle\langle a_q^\dagger; a_q^\dagger\rangle\rangle & \langle\langle a_q^\dagger; a_q\rangle\rangle \end{pmatrix} \equiv \begin{pmatrix} G_q^{(\mathrm{ph})11} & G_q^{(\mathrm{ph})12} \\ G_q^{(\mathrm{ph})21} & G_q^{(\mathrm{ph})22} \end{pmatrix} .
\tag{3.65}
$$

This set of Green's functions fulfills the following equation of motion

$$
\omega\langle\langle a_q(t); a_q^\dagger(t')\rangle\rangle = \langle[a_q, a_q^\dagger]\rangle + \langle\langle[a_q, H]; a_q^\dagger\rangle\rangle,
\tag{3.66}
$$

where $[a_q, H] = [a_q, H_{ph}] + [a_q, H_{mph}] + [a_q, H_{fph}]$. The related calculations can be found in appendix. The equation of motion reads

$$
\omega\cdot\begin{pmatrix} G_q^{(\mathrm{ph})11} & G_q^{(\mathrm{ph})12} \\ G_q^{(\mathrm{ph})21} & G_q^{(\mathrm{ph})22} \end{pmatrix} = \begin{pmatrix} 1 & 0 \\ 0 & -1 \end{pmatrix} + \begin{pmatrix} \varpi_q{}^{11} & \varpi_q{}^{12} \\ \varpi_q{}^{21} & \varpi_q{}^{22} \end{pmatrix}\begin{pmatrix} G_q^{(\mathrm{ph})11} & G_q^{(\mathrm{ph})12} \\ G_q^{(\mathrm{ph})21} & G_q^{(\mathrm{ph})22} \end{pmatrix} ,
$$

with

$$
\begin{aligned}
\varpi_q{}^{11} &= \omega_0 + \bar{B}_q\langle Q\rangle + \frac{1}{2}\bar{A}_q\langle Q^2\rangle - \frac{1}{2}M\bar{R}^{(m)}(q) - \frac{1}{2}P\bar{R}^{(f)}(q)\cos\nu , \\
\varpi_q{}^{12} &= \bar{B}_q\langle Q\rangle + \frac{1}{2}\bar{A}_q\langle Q^2\rangle - \frac{1}{2}M\bar{R}^{(m)}(q) - \frac{1}{2}P\bar{R}^{(f)}(q)\cos\nu , \\
\varpi_q{}^{11} &- \varpi_q{}^{12} = \omega_0 , \\
\varpi_q{}^{21} &= -\varpi_q{}^{12} \quad , \quad \varpi_q{}^{22} = -\varpi_q{}^{11} .
\end{aligned}
\tag{3.67}
$$

Furthermore we have defined $\bar{B}(q) = \frac{B(q)}{(2w_q^0)}$ and $\bar{A}(q) = \frac{A(q)}{(2w_q^0)}$ and correspondingly $\bar{R}^{(f)}$ and $\bar{R}^{(m)}$ which designate the amplitudes for coupling phonons to the (pseudo) spin-wave excitations in first and second order, respectively. From here we drive the phonon dispersion relation as

$$\omega(q) = \sqrt{(\varpi_q^{11})^2 - (\varpi_q^{12})^2}\,. \tag{3.68}$$

The renormalized phonon excitation energy is given by the poles of the related Green's function and reads

$$\omega_q^2 = \omega_0^2 + 2\omega_0 \left(\bar{B}_q \langle Q \rangle + \frac{1}{2} \bar{A}_q \langle Q^2 \rangle - \frac{1}{2} M \bar{R}^{(m)}(q) - \frac{1}{2} \bar{R}^{(f)}(q) P \cos \nu \right). \tag{3.69}$$

Let us stress that the renormalized phonon frequency in Eq. (3.69) is apart from the coupling parameters determined by the magnetization M and the polarization P. Those macroscopic quantities like magnetization and polarization can be also found using Green's function. To find the excitation energies one needs the quantity of $\langle Q \rangle$ where $\langle Q \rangle \propto \langle a \rangle$. In order to find $\langle a \rangle$ we calculate $\langle [a_q, H] \rangle = 0$. $N_q = \langle a_q^\dagger a_q \rangle$ is the phonon correlation function. We write

$$\langle [a_q, H] \rangle = \omega_0 \langle a \rangle + \frac{1}{2} \bar{B}_0 (\omega_0)^{-\frac{1}{2}} \underbrace{(\langle aa^\dagger \rangle + \langle a^\dagger a \rangle)}_{(2N+1)} + \frac{1}{6} \bar{A}_0 (2\omega_0)^{-1} \big[(\langle a \rangle + \langle a^\dagger \rangle)(3N + 1) \big]$$
$$- \bar{R}_M(0) \langle S_z \rangle (\langle a \rangle + \langle a^\dagger \rangle) - \bar{R}_F(0)(\langle a \rangle + \langle a^\dagger \rangle)(\frac{1}{2} - \langle \rho \rangle) \cos \nu$$
$$- \bar{F}_M(0) \langle s_z \rangle - \bar{F}_F(0)(\frac{1}{2} - \langle \rho \rangle) \cos \nu\,, \tag{3.70}$$

if $\langle a \rangle = \langle a^\dagger \rangle$ then

$$\langle [a_q, H] \rangle = \omega_0 \langle a \rangle + \frac{1}{2} \bar{B}_0 (\omega_0)^{-\frac{1}{2}} (2N + 1) + \frac{1}{3} \bar{A}_0 (2\omega_0)^{-1} \langle a \rangle (3N + 1)$$
$$- 2\bar{R}_M(0) \langle S_z \rangle \langle a \rangle - 2\bar{R}_F(0) \langle a \rangle (\frac{1}{2} - \langle \rho \rangle) \cos \nu - \bar{F}_M(0) \langle s_z \rangle \tag{3.71}$$
$$- \bar{F}_F(0)(\frac{1}{2} - \langle \rho \rangle) \cos \nu\,,$$

and

$$\langle a \rangle = \frac{-\frac{1}{2} \bar{B}_0 (2N + 1) + M \bar{F}_M(0) + \bar{F}_F(0) P \cos \nu}{\omega_0 + \bar{A}_0 (2N + 1) - 2M \bar{R}_M(0) - 2P \bar{R}_F(0) \cos \nu}\,, \tag{3.72}$$

follows.

3.4.3. Phonon modes and their influence on magnetization and polarization

In the previous section we found an analytical expression for the phonon excitation of the multiferroic material (Eq. (3.69)). The spectrum is determined by the magnetization M, the polarization P, the anharmonic phonon interactions $\bar{B}_q, \bar{A}_q$ as well

as the various spin-phonon coupling parameters $\bar{R}^{(m)}$ and $\bar{R}^{(f)}$. In this section the results will be discussed and compared with experimental observations. Depending on the sign of the spin-phonon interaction constant R, see Eq. (3.61), the phonon frequencies become either harder or softer. The actual behavior depends on the interaction between the ferroic subsystems and hence it is a material-specific property. In BiMnO$_3$ and YCrO$_3$ one observes an interaction between the ferromagnetic and the ferroelectric subsystem, whereas YMnO$_3$ and BiFeO$_3$ offer a coupling between an antiferromagnetic and ferroelectric systems [52]. As demonstrated in [113] BiCrO$_3$ films exhibit a multiferroic coupling between antiferroelectricity and antiferromagnetism (or weak ferromagnetism). Following this line we have analyzed the influence of the magnetic and the ferroelectric subsystem as well as the MEC on the phonon excitation energy.

L+et us emphasize the anomalies around the ferroelectric and magnetic phase transitions. The numerical calculations for the optical phonon energy are based on the following model parameters which are relevant for TbMn$_2$O$_5$ [81]: T$_C$ = 38 K, T$_N$ = 43 K, J_0' = 75 K, K_0 = -7 K, s = 1/2, S = 2, ω_0 = 96.3 cm^{-1}. The anharmonic interaction parameters are estimated to be $A = -1\,\mathrm{cm}^{-1}$, $B = 0.5\,\mathrm{cm}^{-1}$, $F_0^{(m)} = F_0^{(f)} = 4\,\mathrm{cm}^{-1}$. In principle, the spin-phonon interaction constant R can be positive or negative leading to hardening or softening of the phonon mode, respectively. The measured temperature dependence of the phonon mode in TbMn$_2$O$_5$ reveals a softening of that mode [55] which suggests a negative coupling parameter $R < 0$. This means that the mode frequencies decrease rapidly as the temperature approaches the ferroelectric phase transition from below. In the opposite case ($R > 0$) the phonon mode becomes harder. A softening of the phonon mode at zero-wave vector $\omega(q = 0, T)$ with increasing temperature is also observed for DyMn$_2$O$_5$, BiMn$_2$O$_5$ [102] and EuMn$_2$O$_5$ [103]. The frequency of the mode versus the temperature is shown in Fig. 3.10. The harmonic phonon energy ω_0 introduced in Eq. (3.58) is renormalized due to the anharmonic spin-phonon and phonon-phonon interaction terms and becomes temperature-dependent. The phonon excitation is obtained in Eq. (3.69). The spin-phonon interactions are dominant at low temperatures, whereas at higher temperatures, above T$_N$, there remains only the anharmonic phonon-phonon coupling. Totally the phonon energy decreases slightly. The dispersion relation in Fig. 3.10 shows two kinks at the the ferroelectric phase transition temperature T$_C$ = 38 K and at the magnetic transition T$_N$ = 43 K. The first anomaly occurs when the ferroelectric order disappears. As above T$_C$ the ME coupling K_0 is irrelevant, the kink in the dispersion relation is a direct consequence of the ME coupling. The second kink reflects the influence of the magnetic order on the phonon energy. The frequency shift below T$_C$ is mainly originated in the anharmonic spin-phonon interactions introduced in Eq. (3.61). Let us remind that the spin-phonon coupling comes from the exchange interaction $J_{ij} = J(r_i - r_j)$ (and $\tilde{J}_{ij}$, compare Eq. (3.2) as well as J_{ij}', see Eq. (3.58)).

Assuming the interaction depends on the actual lattice coordinates they can be expanded with respect to the phonon displacements u_i and u_j. Hence the spin-phonon coupling parameters are determined by the first and second order derivatives of the related exchange coupling J_{ij}. The results shown in Fig. 3.10 are in agreement with experimental observations in different RMn$_2$O$_5$ compounds [93, 100–104]. In TbMn$_2$O$_5$
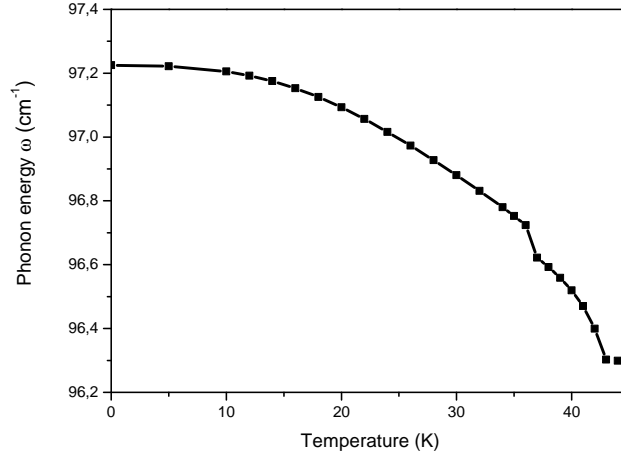
Figure 3.10. – Temperature dependence of the phonon energy ω_0 for TbMn$_2$O$_5$ with $K_0 = -7$ K, $R_0^{(m)} = -0.35\,\mathrm{cm}^{-1}$, $R_0^{(f)} = -0.45\,\mathrm{cm}^{-1}$, $F_0^{(m)} = F_0^{(f)} = 4\,\mathrm{cm}^{-1}$. The bare phonon frequency is $\omega_0 = 96.3$ cm^{-1}. The mode shows a softening behavior for negative spin-phonon coupling R.

a small increase will be observed in the phonon curve between T$_C$ and T$_N$ [101]. Such a behavior can be reproduced in our approach if a positive coupling $R^{(m)} > 0$ is assumed within the temperature interval $T_C \leq T \leq T_N$. A hardening of the phonon mode is reported in HoMn$_2$O$_5$ [100], which is consistent with our studies adopting positive spin-phonon couplings $R^{(f)} > 0$ and $R^{(m)} > 0$, see Fig. 3.11. The mentioned
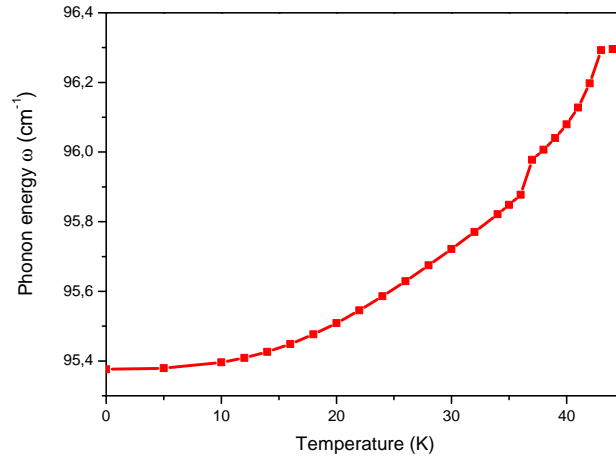
Figure 3.11. – Temperature dependence of the phonon energy ω_0 for TbMn$_2$O$_5$ with $K_0 = -7$ K, $R_0^{(m)} = 0.70\,\mathrm{cm}^{-1}$, $R_0^{(f)} = 0.90\,\mathrm{cm}^{-1}$, $F_0^{(m)} = F_0^{(f)} = 4\,\mathrm{cm}^{-1}$. The mode offers hardening for positive spin-phonon coupling R.

anomalies at T$_C$ and T$_N$ are also reproduced. The ME coupling parameter is introduced in Eq. (3.7). The effect of the magnetoelectric coupling constant K_0 between

the magnetic and electric subsystems is shown in Fig. 3.12. As shown the phonon
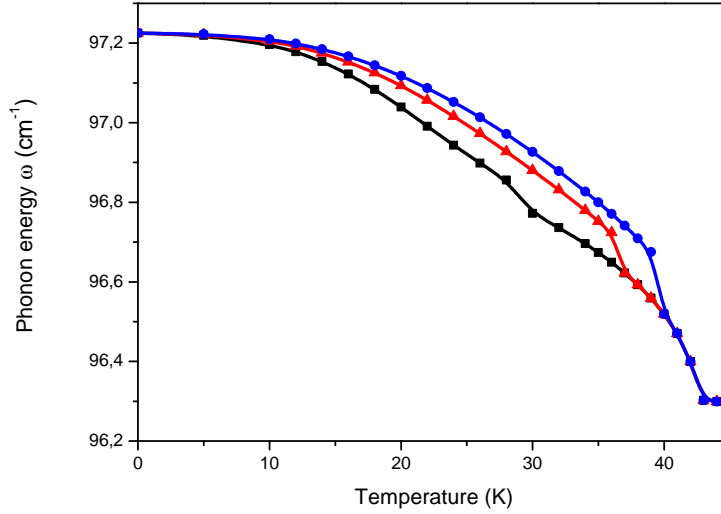
Figure 3.12. – Temperature dependence of the phonon mode energy for different magnetoelectric coupling $K_0 = -3$ K (black/lower curve); $K_0 = -7$ K (red/middle curve); $K_0 = -10$ K (blue/upper curve).

energy depends on the ME coupling K_0 in a significant manner. The kink at T$_C$ is shifted to higher temperatures, i.e. T$_C$ is increased for stronger ME coupling. The magnetic phase transition temperature T$_N$ remains unchanged by the ME coupling K_0 [114].

Let us remark that there is an experimental evidence for different coupling strengths and even for different coupling mechanisms compare to what we discussed here between the magnetic and the ferroelectric subsystems. So the replacement of Y atoms by magnetic Ho atoms in YMnO$_3$ leads to a stronger suppression of the thermal conductivity [115]. Another study in [116] predicts that the polarization in orthorhombic HoMnO$_3$ with biquadratic ME coupling would be enhanced by up to two orders of magnitude with respect to that in orthorhombic TbMnO$_3$. In that compound the ME interaction term is linear in the electrical dipole moments.

The phonon energy is very sensitive to the anharmonic spin-phonon interaction constants $R^{(m)}$ and $R^{(f)}$. The situation is depicted in Fig. 3.13. The phonon energy increases strongly with increasing $R^{(m)}$ below T$_N$, see Fig. 3.13(a), or with $R^{(f)}$ below T$_C$, in the multiferroic phase, compare Fig. 3.13(b). Synchrotron X-ray studies give evidence of lattice modulation in the ferroelectric phase of YMn$_2$O$_5$ [117], however the atomic displacements seem to be extremely small. Moreover, several phonons in TbMn$_2$O$_5$ exhibit explicit correlations to the ferroelectric properties of these materials [101]. The magnetization and polarization in multiferroic substances are affected by such external electric or magnetic fields. The influence of an external magnetic field $h = g\mu_B B$, see Eq.(3.2), on the polarization P is demonstrated experimentally in TmMn$_2$O$_5$ [95], in MnWO$_4$ [96] and in orthorhombic YMnO$_3$ [97]. The strong ME coupling in these materials can be illustrated by studying the influence of an ap-
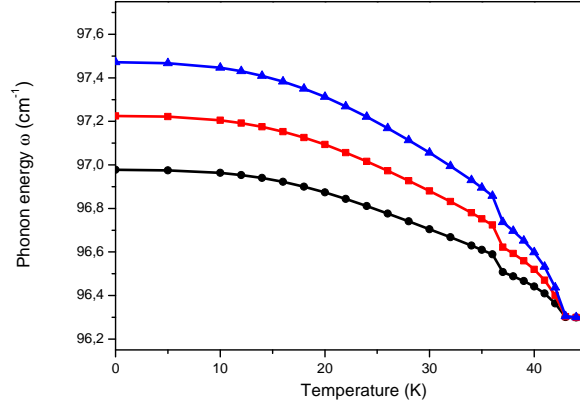
(a) $\omega(q = 0, T, R^{(m)})$
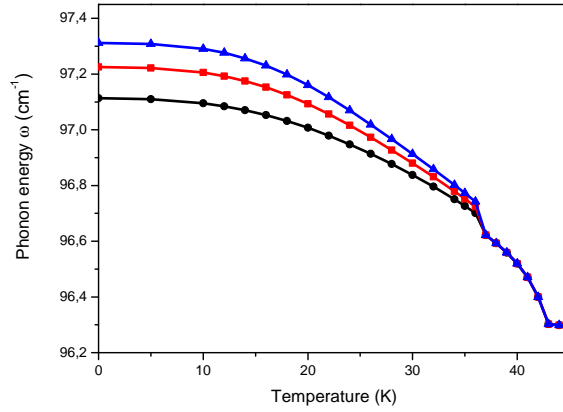
(b) $\omega(q = 0, T, R^{(f)})$

Figure 3.13. – Temperature dependence of the phonon energy for different (a) Spin-phonon couplings: $R^{(m)} = -0.45$ K (black/lower curve); $R^{(m)} = -0.70$ K (red/middle curve); $R^{(m)} = -0.95$ K (blue/upper curve); (b) Pseudospin-phonon couplings: $R^{(f)} = -0.45$ K (black/lower curve); $R^{(f)} = -0.90$ K (red/middle curve); $R^{(f)} = -1.25$ K (blue/upper curve).

plied magnetic field on the phonon spectrum. The result of our calculation is shown in Fig. 3.14. The phonon energy ω increases with increasing magnetic field h. Significant changes of the phonon energy due to magnetic fields are reported for orthorhombic TbMnO$_3$ [118] and for hexagonal HoMnO$_3$ [119]. Experimental data for RMn$_2$O$_5$ are still missing. Both phase transitions are indicated by the corresponding kinks in the phonon energy. For higher temperatures beyond 45 K we find no peculiarities. Fig. 3.14 shows that under the influence of a magnetic field the phase transition temperatures T$_C$ and T$_N$ are altered, where the effect is more pronounced for T$_C$ as a further indication of the magnetoelectric behavior. So the phase transition temperature T$_C$ is enhanced by about $4 - 5$ K. These changes are very sensitive to the model
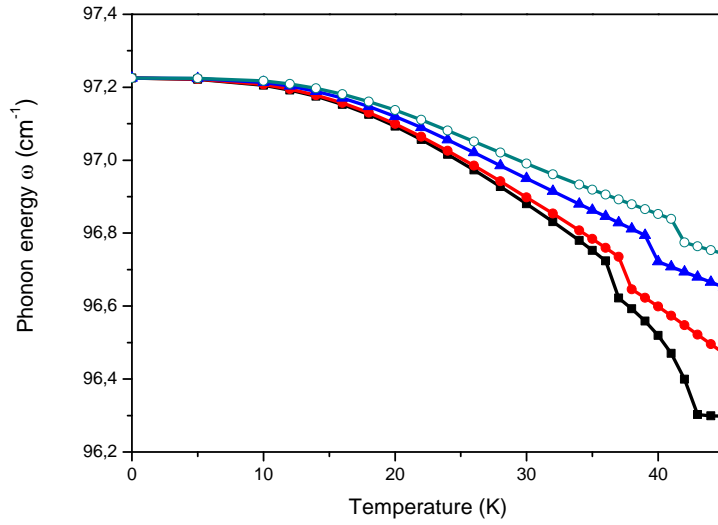
Figure 3.14. – Phonon energy versus temperature for different external magnetic field: $h = 0$ (black/lower curve), $h = 1$ K (read curve), $h = 5$ K (blue curve), $h = 10$ K (green curve).

parameters. The increase of T_C with the magnetic field h and a vanishing kink at T_N is observed in [120]. The dependence of the phonon frequency on the magnetic field is depicted in Fig. 3.15.
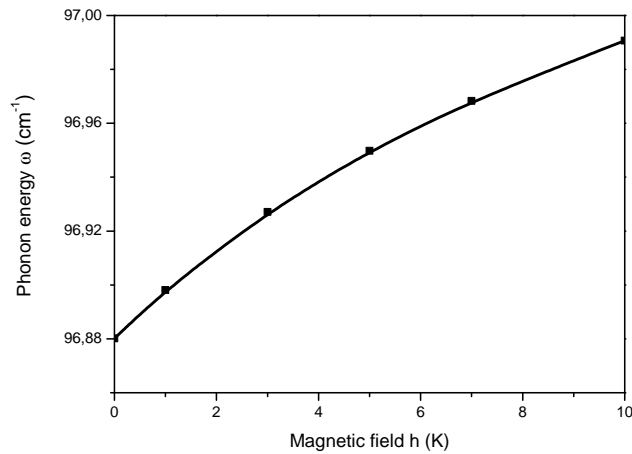
Figure 3.15. – Phonon frequency versus the magnetic field at fixed temperature, $T = 30$ K.

As expected, the phonon excitation energy for wave vector $\mathbf{q}$ is enhanced when the field is increased. As remarked in [121] the effect of a magnetic field or hydrostatic pressure are strongly dependent on the R atom in the RMn_2O_5 systems. The compression of these materials is supposed to be equivalent to applying a magnetic field

[122]. In [99, 123] it has been shown that the coupling between the magnetic orders and the dielectric properties in multiferroic RMn_2O_5 (R = Ho, Dy, Tb) is mediated by the lattice distortion. The mentioned compounds have different ionic sizes. Hence the thermal expansion data display specific differences of the lattice strains. In case R stands for Ho and Dy then a contraction appears along the c-axis, while one observes an expansion along the a- and b-axis at T_C. The opposite behavior is observed for Tb. The origin of this fact is due to the different spin modulations along the c-axis. The spin-lattice coupling leads to different stress in the lattice. As demonstrated in the
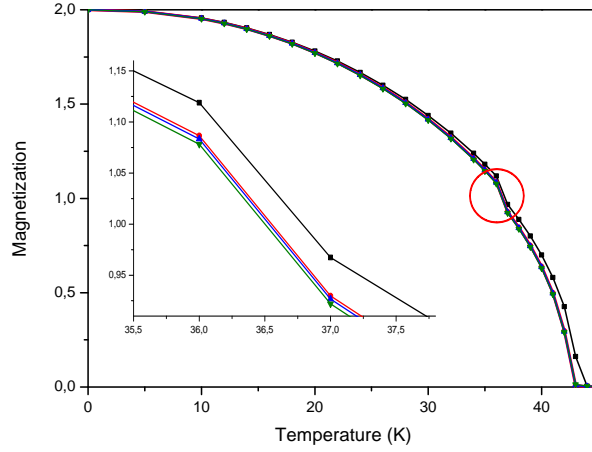
(a) $M(T)$
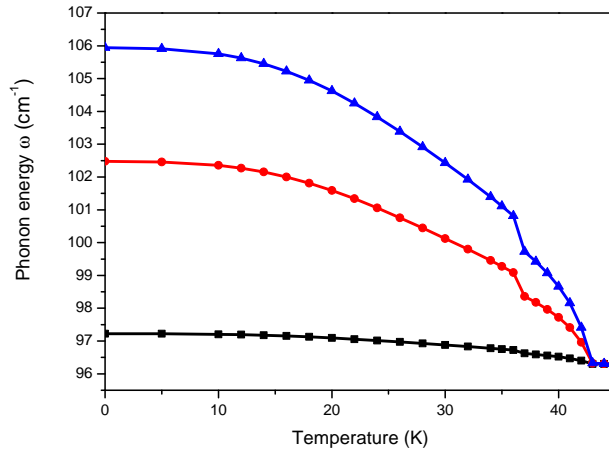
(b) $\omega(T)$

Figure 3.16. – Temperature dependence of the (a) Magnetization and (b) Phonon mode energy for changed spin-phonon coupling: $R^{(m)} = 7.5$ cm^{-1}, $R^{(f)} = 1.5$ cm^{-1} (blue), $R^{(m)} = 4.5$ cm^{-1}, $R^{(f)} = 7.5$ cm^{-1} (red), $R^{(m)} = 0.70$ cm^{-1}, $R^{(f)} = 0.90$ cm^{-1} (black).

previous section, the Green's function technique allows also to calculate macroscopic

quantities like the magnetization M and the influence of the phonon degrees of freedom on M. The results are shown in Fig. 3.16. In Fig. 3.16(a) one finds the influence of the spin-phonon coupling on the magnetization $M(T)$. Increasing the spin-phonon coupling parameter $R^{(m)}$ the magnetization decreases. The magnetic transition temperature T_N is lowered accordingly. In Fig. 3.16(b) the phonon energy is represented as function of the temperature with different (pseudo) spin-phonon couplings. The phonon excitation energy increases strongly when the spin-phonon coupling $R^{(m)}$ is enhanced. In the same manner the magnetization is slightly decreased. Obviously, the lattice degrees of freedom affect the magnetization and the phonon spectrum. Thus, for rare-earth R=Tb the system offers a tensile strain. The ordered Mn magnetic moments are suppressed at high pressure. The kink at T_C is due to the ME coupling and can be observed again. Our results are in agreement with the experimental data for orthorhombic BiMnO$_3$ and LuFe$_2$O$_4$ [124, 125]. There are no data available for the influence of pressure on the magnetic properties of MF RMn$_2$O$_5$ systems. For the polarization the influence of the coupling is not very pronounced. The effect is clearly stronger for the magnetization than for the polarization.

3.5. Extended Heisenberg model for asymmetric zigzag structures in RMn_2O_5

As we already discussed in previous section, the family of manganese oxides with general formula RMn_2O_5 (R = rare-earth, Bi, and Y) have provided a new and different perspective in the field of multiferroics due to very complex magnetic and ferroelectric phase transitions upon temperature variation. Regarding the magnetic properties of these compounds, some works have been devoted to the determination of their magnetic structures using powder neutron diffraction [126, 127]. The analysis shows that the magnetic structures of the RMn_2O_5 series mainly differ in their periodicity along the c-axis, which is determined by the radius of R. In orthorhombic RMn_2O_5, the spins of the Mn^{4+} and Mn^{3+} ions and the R^{3+} moments are coupled via the predominantly antiferromagnetic (AFM) superexchange interactions giving rise to a complex magnetic phase diagram. This crystal structure is best described by considering ab-planes and a c-axis stacking, as shown in Fig. 3.17. Such a complex structure results in five different magnetic interactions which can be identified between neighboring spins [81].

Along c, Mn^{4+} atoms interact via direct exchange and weak superexchange with two inequivalent interactions (J_1, through the R layer, J_2 through the Mn^{3+} layer). The Mn^{4+} also linked to $Mn^{3+}O_5$ pyramids either through their pyramidal base corners (J_3) or through the pyramid apex (J_4). J_3 and J_4 are both of the superexchange type and are controlled by $Mn^{4+}-O-Mn^{3+}$ bond angles ($\sim 131°$ for J_3 and $\sim 123°$ for J_4), which is close to the critical angle between FM and AFM according to the Goodenough-Kanamori-Anderson (GKA) rules [38, 128]. Finally, the pyramids are linked together by their base edges (J_5). The configuration parallel to c, involving interactions J_1 and J_2, is determined only by the radius of the rare-earth cation. In the ab-plane the nearest neighbor interaction along the a-axis (J_4, J_5) is stronger than that along the b-axis (J_3, J_5). This results in zigzag AFM chains parallel to the a-axis mediated by $J_4 > 0$ and $J_5 > 0$. J_3 is then close to zero, and alternates between FM and AFM, linking the AFM chains [81]. The arrangement of Mn spins within the ab-plane, which are responsible for magnetism, is essentially insensitive to R. So with a good approximation one can consider $J_1 = J_2$.
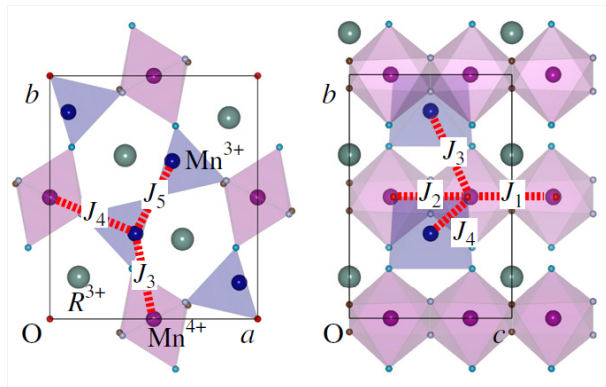
Figure 3.17. – Crystal structure of RMn_2O_5 in the paraelectric phase, projected on the ab-plane (left panel) and bc-plane (right panel). Taken from [121].

RMn$_2$O$_5$ materials form frustrated magnets. As it is shown in Fig. 3.17 the Mn spins are arranged in the five-spin loop; Mn^{4+}-Mn^{3+}-Mn^{3+}-Mn^{4+}-Mn^{3+}. The nearest neighbor magnetic coupling in the loop is of the antiferromagnetic type, favoring antiparallel alignment of the neighboring spins. However, because of the odd number of spins in one loop, a perfect antiparallel spin configuration cannot be possible, eventually leading to the frustrated complex magnetic structure [59]. Because of the complex magnetic interactions and the MEC, RMn$_2$O$_5$ compounds undergo several magnetic and associated electric phase transitions upon temperature fluctuation and external stimuli. Below $T_{2DICM} \simeq 43$ K a two dimensional incommensurate (2DICM) manganese magnetic structure forms with propagation vector q = (q$_x$, 0, q$_z$). At $T_{CM} \simeq 38$ K, the magnetic propagation locks into a commensurate phase (CM) with q = (0.5, 0, 0.25). Then unusually at $T_{LT-2DICM} \simeq 25$ K, there occurs a re-entry into a second incommensurate phase at low temperature (LT-2DICM). For those members with magnetic rare-earth ions (i.e. excluding Y, Bi or La) a final transition occurs at $T_{RE} \simeq 10$ K into the LT-2DICM phase, marking the onset of spontaneous rare-earth ordering.

To investigate the thermodynamic properties of these materials, we simplified the complex magnetic structure by the model shown in Fig. 3.2(b). However, the main mechanism for the appearance of a nontrivial polarization P in RMn$_2$O$_5$ (R = Tb, Y, Dy, and Bi) has been attributed to exchange-striction among frustrated Mn spin networks [81].
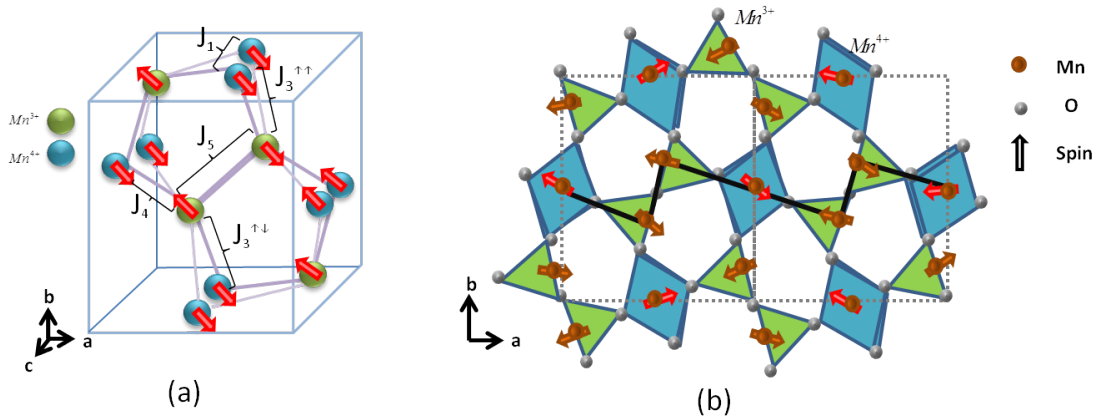
Figure 3.18. – (a) Spin configuration of RMn$_2$O$_5$, (b) Projected on the ab-plane.

In this section, building upon experimental facts and the space group symmetry, we will propose a more realistic model to study the properties of antiferromagnetic zigzag spin chain of two different Mn^{4+} and Mn^{3+} magnetic ions as it shown in Fig. 3.18. Here, we will present our first results for these rather complex structures which had bin studied before only by ab-initio calculations. We demonstrate that the Heisenberg model can be extended in a manner that it incorporates such more complex magnetic order like zigzag structures.

3.5.1. Analytical representation of multiferroics with asymmetric zigzag spin chain

The most important element controlling ferroelectricity is the in-plane components of the magnetic structure. The spin configuration in the ab-plane is shown in Fig. 3.18. It can be seen that two zigzag chains per unit cell of AFM-coupled nearest neighbor Mn^{4+} and Mn^{3+} run in a direction parallel to the a-axis. The electrical polarization is proportional to the scalar product of spins in different zigzag chains. The electrical polarization is always directed along the b-axis by symmetry. The spin configuration within the ab-plane of the commensurate phases is essentially the same for each system; the radius of R determines the sign of the magnetic exchange between adjacent planes. We investigate the system by considering two ferromagnetic zigzag spin chains consist of two different magnetic ion which are coupled antiferromagnetically as it shown in Fig. 3.19 forming an antiferromagnetic asymmetric zigzag spin chain. Mn^{3+} and Mn^{4+} ions denoted as A and B. These chains are coupled to each other through Mn^{4+} ions with the exchange interactions $J_1 = J_2$ in c-direction.
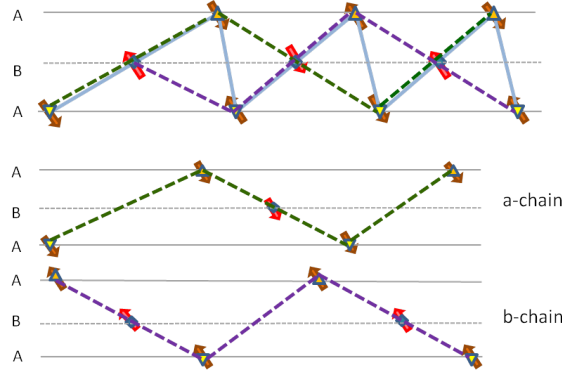
Figure 3.19. – Antiferromagnetic asymmetric zigzag chain consisting of two ferromagnetic spin chains of different spin magnitude.

The Hamiltonian of magnetic subsystem in a-direction can be presented as

$$H_m = -\frac{1}{2} \sum_{i,j} \sum_{\alpha,\beta} \sum_{\nu\mu} J^{\nu\mu}_{i\alpha,j\beta} (\mathbf{S}^\nu_{i\alpha} \cdot \mathbf{S}^\mu_{j\beta}) . \qquad (3.73)$$

The J's represent the nearest neighbor spin interactions. i, j refer to lattice sites. α, β represent the two ferromagnetic chains, introduced as 'a' and 'b'. ν, μ show Mn^{3+} and Mn^{4+} sublattices denoted as A and B, respectively. These indexes allow us to take in to account the complex exchange interactions that are expected.

Along the b-direction, $TbMn_2O_5$ exhibits a charge and spin ordering that can schematically be denoted as a chain of $Mn^{4+}_\uparrow - Mn^{3+}_\downarrow - Mn^{3+}_\uparrow - Mn^{4+}_\uparrow$ which is repeated along this direction. In the undistorted Pbam structure, the distances $d \uparrow\uparrow$ (between $Mn^{3+}_\uparrow$ and $Mn^{4+}_\uparrow$) and $d \downarrow\uparrow$ (between $Mn^{3+}_\downarrow$ and $Mn^{4+}_\uparrow$) are the same. In Pb21m structure $d \uparrow\uparrow < d \downarrow\uparrow$, which optimizes the double exchange energy and causes ferroelectricity.

Although the structure must be polar in the ferroelectric phase, experimental data does not provide direct evidence for the lowering of symmetry from Pbam to Pb21m and any low temperature deviation from Pbam symmetry is very small [80]. This is consistent with the extremely weak nature of the polarization, two or three orders of magnitude smaller than in typical ferroelectrics, which is not expected to give large atomic displacements.

The ferroelectric subsystem was considered by defining polarization operators P in b-direction.

$$H_f = \frac{1}{2} \sum_{i,j} L_{ij} P_i^{(b)} P_j^{(b)} . \tag{3.74}$$

This polar part offers no phase transition. The ferroelectric phase transition is triggered by inclusion of the coupling term which is responsible for the improper ferroelectricity in these materials. The polarization is obtained by minimizing of the free energy considering $H = H_f + H_{mf}$ as a Hamiltonian. The related coupling Hamiltonian can be written as

$$H_{mf} = -\frac{1}{2} \sum_{\alpha,\beta} \sum_{i,j,r} K_{ijr} P_r^{(b)} J_{i\alpha j\beta}^{AB} (1 - 2\delta_{\alpha\beta}) \mathbf{S}_{i\alpha}^A \cdot \mathbf{S}_{j\beta}^B . \tag{3.75}$$

Here P$^{(b)}$ reflexes the direction of polarization.

3.5.2. Green's Function calculation

Considering the appropriate commutation relations

$$\begin{aligned}
[S_{l\gamma}^{+\varphi}, S_{i\alpha}^{+\nu} S_{j\beta}^{-\mu}] &= 2S_{i\alpha}^{+\nu} S_{j\beta}^{z\mu} \delta_{\gamma\beta} \delta_{\varphi\mu} \delta_{lj}, \\
[S_{l\gamma}^{+\varphi}, S_{i\alpha}^{z\nu} S_{j\beta}^{z\mu}] &= -S_{i\alpha}^{z\nu} S_{j\beta}^{+\mu} \delta_{\gamma\beta} \delta_{\varphi\mu} \delta_{lj} - S_{i\alpha}^{+\nu} S_{j\beta}^{z\mu} \delta_{\gamma\alpha} \delta_{\varphi\nu} \delta_{li},
\end{aligned} \tag{3.76}$$

the Green's function reads

$$\begin{aligned}
\omega G_{\gamma\Gamma}^{\varphi^+\phi^-}(q) =& 2\langle s_\Gamma^{z\phi}\rangle \delta_{\gamma\Gamma}\delta_{\varphi\phi} + \sum_{\alpha,\gamma} -J_{\alpha\gamma}^{\varphi\nu}(q)\langle S_\gamma^{z\phi}\rangle G_{\alpha\Gamma}^{\nu^+\phi^-}(q) + J_{\alpha\gamma}^{\varphi\nu}(0)\langle S_\alpha^{z\nu}\rangle G_{\gamma\Gamma}^{\varphi^+\phi^-}(q) \\
&- \frac{1}{2}\Bigg[2K_{q+q'}\langle P\rangle\big(J_{\alpha\gamma}^{AB}(q')G_{\alpha\Gamma}^{A^+\phi^-}(q) - J_{\beta\gamma}^{AB}(q')G_{\beta\Gamma}^{B^+\phi^-}(q)\big)\langle S_\alpha^{z\varphi}\rangle \\
&- K_0\langle P\rangle\big(J_{\alpha\gamma}^{AB}(0)\langle S_\alpha^{zA}\rangle + J_{\beta\gamma}^{AB}(0)\langle S_\beta^{zB}\rangle\big)G_{\gamma\Gamma}^{\varphi^+\phi^-}(q) \\
&- 2\bigg(2K_{q+q'}\langle P\rangle J_{\gamma\gamma}^{AB}(q')\langle S_\gamma^{z\varphi}\rangle\big(G_{\gamma\Gamma}^{A^+\phi^-}(q) - G_{\gamma\Gamma}^{B^+\phi^-}(q)\big) \\
&- K_0\langle P\rangle J_{\gamma\gamma}^{AB}(0)\big(\langle S_\gamma^{zA}\rangle + \langle S_\gamma^{zB}\rangle\big)G_{\gamma\Gamma}^{\varphi^+\phi^-}(q)\bigg)\Bigg] .
\end{aligned} \tag{3.77}$$

It can be written as

$$\omega \cdot \begin{pmatrix} G_{aa}^{A^+A^-} & G_{ab}^{A^+A^-} & G_{aa}^{A^+B^-} & G_{ab}^{A^+B^-} \\ G_{ba}^{A^+A^-} & G_{bb}^{A^+A^-} & G_{ba}^{A^+B^-} & G_{bb}^{A^+B^-} \\ G_{aa}^{B^+A^-} & G_{ab}^{B^+A^-} & G_{aa}^{B^+B^-} & G_{ab}^{B^+B^-} \\ G_{ba}^{B^+A^-} & G_{bb}^{B^+A^-} & G_{ba}^{B^+B^-} & G_{bb}^{B^+B^-} \end{pmatrix} = \begin{pmatrix} 2\langle S_A^z\rangle & 0 & 0 & 0 \\ 0 & -2\langle S_A^z\rangle & 0 & 0 \\ 0 & 0 & 2\langle S_B^z\rangle & 0 \\ 0 & 0 & 0 & -2\langle S_B^z\rangle \end{pmatrix}$$

$$
+ \begin{pmatrix} \varepsilon_q^{11} & \varepsilon_q^{12} & \varepsilon_q^{13} & \varepsilon_q^{14} \\ \varepsilon_q^{21} & \varepsilon_q^{22} & \varepsilon_q^{23} & \varepsilon_q^{24} \\ \varepsilon_q^{31} & \varepsilon_q^{32} & \varepsilon_q^{33} & \varepsilon_q^{34} \\ \varepsilon_q^{41} & \varepsilon_q^{42} & \varepsilon_q^{43} & \varepsilon_q^{44} \end{pmatrix} \begin{pmatrix} G_{aa}^{A^+A^-} & G_{ab}^{A^+A^-} & G_{aa}^{A^+B^-} & G_{ab}^{A^+B^-} \\ G_{ba}^{A^+A^-} & G_{bb}^{A^+A^-} & G_{ba}^{A^+B^-} & G_{bb}^{A^+B^-} \\ G_{aa}^{B^+A^-} & G_{ab}^{B^+A^-} & G_{aa}^{B^+B^-} & G_{ab}^{B^+B^-} \\ G_{ba}^{B^+A^-} & G_{bb}^{B^+A^-} & G_{ba}^{B^+B^-} & G_{bb}^{B^+B^-} \end{pmatrix},
$$

where

$$
\varepsilon_q^{11} = (J^6(0) - J^6(q) + J^5(0))\langle S_A^z \rangle + \left(J_{\uparrow\uparrow}^3(0) + J_{\uparrow\downarrow}^3(0) + J^4(0)\right)\langle S_B^z \rangle
$$

$$
+ K_{q+q'}\langle P \rangle J_{\uparrow\uparrow}^3(q')\langle S_A^z \rangle - \frac{1}{2}K_0\langle P \rangle\left[J_{\uparrow\uparrow}^3(0) - J_{\uparrow\downarrow}^3(0)\right](\langle S_A^z \rangle + \langle S_B^z \rangle) = -\varepsilon_q^{22},
$$

$$
\varepsilon_q^{12} = J^5(q)\langle S_A^z \rangle + K_{q+q'}\langle P \rangle J_{\uparrow\downarrow}^3(q')\langle S_A^z \rangle = -\varepsilon_q^{21},
$$

$$
\varepsilon_q^{13} = -J_{\uparrow\uparrow}^3(q)\langle S_A^z \rangle - K_{q+q'}\langle P \rangle J_{\uparrow\uparrow}^3(q')\langle S_A^z \rangle = -\varepsilon_q^{24},
$$

$$
\varepsilon_q^{14} = \left(J_{\uparrow\downarrow}^3(q) + J^4(q)\right)\langle S_A^z \rangle - K_{q+q'}\langle P \rangle J_{\uparrow\downarrow}^3(q')\langle S_A^z \rangle = -\varepsilon_q^{23},
$$

$$
\varepsilon_q^{31} = -J_{\uparrow\uparrow}^3(q)\langle S_B^z \rangle + K_{q+q'}\langle P \rangle J_{\uparrow\uparrow}^3(q')\langle S_B^z \rangle = -\varepsilon_q^{42}
$$

$$
\varepsilon_q^{32} = \left(J^4(q) + J_{\uparrow\downarrow}^3(q)\right)\langle S_B^z \rangle + K_{q+q'}\langle P \rangle J_{\uparrow\downarrow}^3(q')\langle S_B^z \rangle = \varepsilon_q^{41},
$$

$$
\varepsilon_q^{33} = (J^4(0) + J_{\uparrow\uparrow}^3(0) + J_{\uparrow\downarrow}^3(0))\langle S_A^z \rangle + (J^1(0) - J^1(q))\langle s_B^z \rangle
$$

$$
- K_{q+q'}\langle P \rangle J_{\uparrow\uparrow}^3(q')\langle S_B^z \rangle - \frac{1}{2}K_0\langle P \rangle\left[J_{\uparrow\uparrow}^3(0) - J_{\uparrow\downarrow}^3(0)\right](\langle S_A^z \rangle + \langle S_B^z \rangle) = -\varepsilon_q^{44},
$$

$$
\varepsilon_q^{34} = -K_{q+q'}\langle P \rangle J_{\uparrow\downarrow}^3(q')\langle S_B^z \rangle = -\varepsilon_q^{43}.
$$

(3.78)

The exchange interactions are defined in Table 3.1. Here $J_{aa}^{AA} \equiv J_6$ represents the NNN interaction between two Mn^{3+} ions. All these quantities are positive. The sign of AFM interactions are considered in the formulas.

Table 3.1. – Different exchange parameters in Eq. (3.77) in accordance to Fig. 3.18.

$J_{aa(bb)}^{BB}$	$J_{aa(bb)}^{AB}$	$J_{ab(ba)}^{AB}$	$J_{ab(ba)}^{AB}$	$J_{ab(ba)}^{AA}$	$J_{aa(aa)}^{AA}$
J^1, J^2	$J_{\uparrow\uparrow}^3$	$J_{\uparrow\downarrow}^3$	J^4	J^5	J^6

To find the excitation energy, we solve

$$
\begin{vmatrix} \omega - \varepsilon_q^{11} & \varepsilon_q^{12} & \varepsilon_q^{13} & \varepsilon_q^{14} \\ \varepsilon_q^{21} & \omega - \varepsilon_q^{22} & \varepsilon_q^{23} & \varepsilon_q^{24} \\ \varepsilon_q^{31} & \varepsilon_q^{32} & \omega - \varepsilon_q^{33} & \varepsilon_q^{34} \\ \varepsilon_q^{41} & \varepsilon_q^{42} & \varepsilon_q^{43} & \omega - \varepsilon_q^{44} \end{vmatrix} = 0
$$

This leads to $\pm\omega_1$ and $\pm\omega_2$ as shows in the appendix. Following Eq. (3.39) the $G_{aa}^{A^+A^-}(q) \equiv G_q^{11}$ reads

$$
G_q^{11} = \frac{I^{11}\left(\omega^3 + A\omega^2 + B\omega + C\right)}{(\omega - \omega_1)(\omega + \omega_2)(\omega - \omega_2)(\omega + \omega_2)}. \tag{3.79}
$$

A, B and C are coefficients which can be found in appendix as well. Eq. (3.79) is simplified as

$$
G_q^{11} = I^{11}\left(\frac{\Gamma_1}{\omega - \omega_1} + \frac{\Gamma_2}{\omega + \omega_1} + \frac{\Gamma_3}{\omega - \omega_2} + \frac{\Gamma_4}{\omega + \omega_2}\right). \tag{3.80}
$$

Comparing Eq. (3.77) and Eq. (3.80) one gets

$$
\begin{aligned}
\Gamma_1 + \Gamma_2 + \Gamma_3 + \Gamma_4 &= 1, \\
\Gamma_1\omega_1 - \Gamma_2\omega_1 + \Gamma_3\omega_2 - \Gamma_4\omega_2 &= A, \\
-\Gamma_1\omega_1^2 - \Gamma_2\omega_2^2 - \Gamma_3\omega_1^2 - \Gamma_4\omega_1^2 &= B, \\
-\Gamma_1\omega_1\omega_2^2 + \Gamma_2\omega_1\omega_2^2 - \Gamma_3\omega_1^2\omega_2 + \Gamma_4\omega_1^2\omega_2 &= C.
\end{aligned}
\tag{3.81}
$$

$\Gamma_1 - \Gamma_4$ will be found using Cramer rules. These quantities are given in the appendix. There are two different magnetic ions in this compound with spin amounts bigger than one. Thus in order to calculate the related magnetization we need a more general formula. For this purpose we solve

$$
\langle (S_z)^m \rangle S(S+1) - \langle (S_z)^{m+1} \rangle - \langle (S_z)^{m+2} \rangle = \langle n \rangle \Big(2\langle S_z(S_z-1)^m \rangle
$$

$$
+ \langle [(S_z-1)^m - S_z^m] \cdot [S(S+1) - S_z - S_z^2] \rangle \Big), \quad m = 0, 1..., 2S-1,
\tag{3.82}
$$

$$
\text{and} \quad \langle (S_z)^{2S+1} \rangle = \sum_{m=0}^{2S} a_m \langle (S_z)^m \rangle .
$$

Considering $\langle S_z \rangle = SM$, the magnetizations of A and B sublattices are

$$
\begin{aligned}
S = 2 &\longrightarrow M_1 = \frac{10n^3 + 15n^2 + 9n + 2}{5(n^4 + 2n^3 + 2n^2 + n) + 1}, \\
S = \frac{3}{2} &\longrightarrow M_2 = \frac{5n^2 + 5n + \frac{3}{2}}{4n^3 + 6n^2 + 4n + 1}, \\
n \equiv \langle n \rangle &= \frac{1}{N} \sum_q \Big(\frac{\Gamma_1(q)}{e^{\beta\omega_1} - 1} + \frac{\Gamma_2(q)}{e^{-\beta\omega_1} - 1} + \frac{\Gamma_3(q)}{e^{\beta\omega_2} - 1} + \frac{\Gamma_4(q)}{e^{-\beta\omega_2} - 1} \Big) .
\end{aligned}
\tag{3.83}
$$

The magnetization of the whole system is

$$
M = \Big| \frac{M_1 + M_2}{2} \Big| .
\tag{3.84}
$$

Using phenomenological approach we calculate the polarization. The free energy is

$$
F = -k_B T ln(Z),
\tag{3.85}
$$

where Z is the partition function. Minimizing the free energy with respect to $P_l^{(b)}$ we get

$$
\chi \langle P \rangle = -\frac{1}{2} \sum_{\alpha,\beta} \sum_{i,j,l} K_{ijl} J_{i\alpha j\beta}^{AB} (1 - 2\delta_{\alpha\beta}) \langle \mathbf{S}_{i\alpha}^A \cdot \mathbf{S}_{j\beta}^B \rangle .
\tag{3.86}
$$

In a first approximation by considering only z-z correlation function, this expression is simplified to

$$
\langle P \rangle = \frac{1}{\chi} \sum_{i,j} K_{ijl} (| J_{\uparrow\downarrow}^3 - J_{\uparrow\uparrow}^3 |) \langle S_A^Z \rangle \langle S_B^Z \rangle,
\tag{3.87}
$$

which reflects the origin of ferroelectricity. In case $J_{\uparrow\downarrow}^3 = J_{\uparrow\uparrow}^3$, the polarization will be vanishes as it expected.

3.6. Ion doping effects in multiferroic MnWO$_4$

In this last part of section 3, devoted to bulk multiferroics, we analyze doping effects which are quite relevant for the understanding of experimental observations and technical applications. The calculation is performed for multiferroic MnWO$_4$ which offers frustration in a zigzag structure. Different quasi-degenerate low energy magnetic structures can be found in a frustrated system. These structures compete for the ground state. As a result, a frustrated system shows high sensitivity of magnetic and ferroelectric phases to small perturbations in form of external magnetic fields [78, 129, 130] or pressure [122, 131, 132]. Chemical substitutions have also been shown to change the multiferroic properties of various compounds [133, 134]. It is therefore of interest to study the effects of substitutional doping in a multiferroic system that allows for the replacement of the major magnetic ion with a variety of other magnetic or non-magnetic ions with the aim of tuning the magnetic exchange coupling and anisotropy parameters and the subtle interaction between different frustrated magnetic and ferroelectric orders.

A unique material that does already exist in nature is the mineral Huebnerite, MnWO$_4$ which not only exhibits multiferroic properties at low temperature but also shows rich magnetic phases via chemical substitutions [135, 136]. The compound crystallizes in a monoclinic structure with the space group P2/c. The details of the magnetic structures have been revealed in neutron scattering experiments [137, 138]. The building blocks of MnWO$_4$ are MnO$_6$ octahedra containing Mn^{2+} ions and WO$_6$ octahedra containing diamagnetic W$^{6+}(d^0)$ ions. The MnO$_6$ octahedra share edges to form zigzag MnO$_4$ chains along the c-direction (see Fig. 3.20(a)), and the WO$_6$ octahedra form zigzag WO$_4$ chains along the c-direction (see Fig. 3.20(b)). The three-dimensional (3D) structure of MnWO$_4$ is obtained from these MnO$_4$ and WO$_4$ chains on sharing their octahedral corners (see Fig. 3.20(c)). Thus, in MnWO$_4$, layers of magnetic Mn^{2+} ions parallel to the bc-plane alternate with layers of diamagnetic W^{6+} ions parallel to the bc-plane along the a-direction. The Mn spins form different frustrated orders upon decreasing temperature. At T$_N$ = 13.5 K, a sinusoidal magnetic order with an incommensurate (ICM) modulation is established. The magnetic order parameter in this AF3 phase is defined by the modulation vector in reciprocal space, $Q_3 = (-0.214, 0.5, 0.457)$ [138]. The Mn spins are collinear and lie in the ac-plane at an angle of 35° with the a-axis. At slightly lower temperature, T$_2$ = 12.6 K, the spins tilt toward the b-axis and form a (non-collinear) helical structure. The magnetic modulation vector in this AF2 phase is the same as in the AF3 phase, $Q_2 = Q_3$. With further decreasing temperature, below T$_1$ = 7.5 K, the Mn spins undergo another phase transition to a frustrated commensurate (CM) AF1 phase with the propagation vector $Q_1 = (-0.25, 0.5, 0.5)$. The latter spin structure corresponds to the ↑↑↓↓ modulation that is characteristic for frustrated magnetic systems with competing nearest and next-nearest neighbor exchange interactions. The loss of inversion symmetry due to the helical spin ordering at AF2 phase induce polarization in MnWO$_4$, thus T$_2$ is also the ferroelectric critical temperature T$_C$. The polarization vector is parallel to the monoclinic b-axis: P = (0, P$_b$, 0). P$_b$ is relatively small. It takes a maximal value (50 μC/m^2) at around T_1, and then monotonously decreases and vanishes at around T$_C$ [78]. Other phases display no sign of FE activity. The
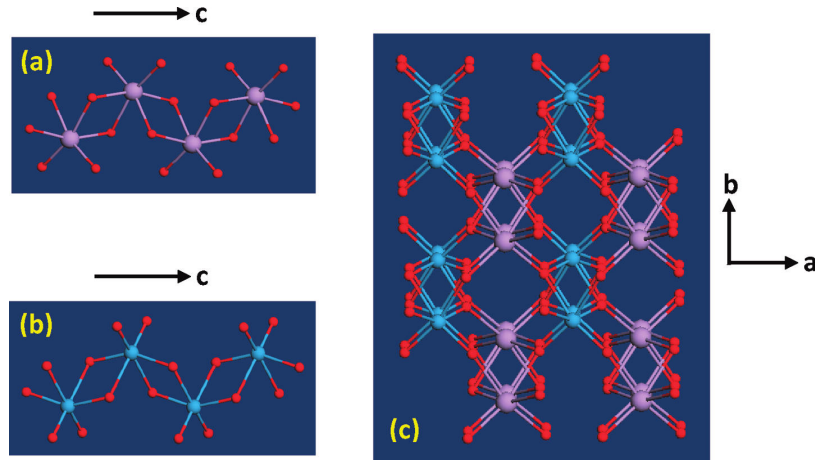
Figure 3.20. – Perspective views of (a) A zigzag MnO$_4$ chain, (b) A zigzag WO$_4$ chain, and (c) The three-dimensional (3D) arrangement of the MnO$_4$ and WO$_4$ chains in MnWO$_4$. Taken from [139].

close proximity of three different magnetic phases proves the existence of significant frustration in the magnetic system. This means that MnWO$_4$ has spin frustration in the exchange interactions within each c-chain and between the c-chains along the a-direction. It further suggests a high degree of sensitivity to small changes of the microscopic exchange interactions and anisotropy parameters. This can be achieved by substituting Mn by other transition metals. MnWO$_4$ is a perfect candidate since it forms stable compounds when Mn is completely replaced by Fe [140], Co, Ni [141], or Zn [142]. The replacement of the Mn^{2+} (spin 5/2) by Fe^{2+} (spin 2), Co^{2+} (spin 3/2), or the non-magnetic Zn will change the magnetic exchange interactions, the single ion anisotropy, and it will introduce disorder into the Mn spin system [143]. The spin-lattice coupling is strong in this compound. We are aware that doping effects have an influences on lattice dynamics and therefore, spin-lattice coupling should be considered in more detail following the line proposed in section 3.4 Such an approach is the goal of future studies.

3.6.1. An effective Hamiltonian for doped frustrated zigzag chain.

Here, we study the ion doping effects on different transition temperatures in the MF compound MnWO$_4$ based on a microscopic model introduced in section 3. By ion doping due to the different radii between the doping ions and the host ions there appear different strains, which lead to changing of the exchange interaction constants. We denote them in the defect sites with the index d. In dependence on the strain - tensile or compressive - they can be smaller or greater compared to the case without strain, without ion doping or defects. Several theoretical studies based on ab-initio methods have been done to explain the origin of ferroelectricity in this material [144, 145]. We assume that the ferroelectricity is related to the frustrated spin structure which is given by the Heisenberg Hamiltonian with NN and NNN AFM exchange interaction within the zigzag spin chain as it shown in Fig. 3.21. In the case
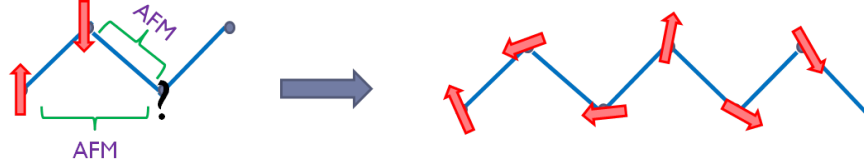
Figure 3.21. – Schematic representation of frustrated magnetic zigzag chain of
  $MnWO_4$.

without defects, Eq. (3.2) describes the interaction between the Mn-ions in $MnWO_4$.
By replacing some of the Mn-ions with different doping ions, the situation would be
similar to a ferrimagnet with two sublattices, so Eq. (3.2) describes the interaction
between the Mn-ions in the new strained lattice, then we must add a Heisenberg term
which describes the interaction between the Co ions, and a term for the description of
the interaction between the Mn-Co ions. Considering the dopant the related magnetic
Hamiltonian reads

$$H_m = -\frac{1}{2}\sum_{i,j}[(1-x)J^{Mn}(i,j)\mathbf{S}_i^{Mn}\cdot\mathbf{S}_j^{Mn} - xJ^d(i,j)\mathbf{S}_i^d\cdot\mathbf{S}_j^d + xJ^{Mn-d}(i,j)\mathbf{S}_i^{Mn}\cdot\mathbf{S}_j^d]$$
$$-\sum_i[D_i^{Mn}(S_i^{zMn})^2 + D_i^d(S_i^{zd})^2].$$

$$(3.88)$$

In addition, H_{mf} gives the coupling between the magnetic and the electrical subsys-
tems in $MnWO_4$ which is in the form of Eq. (3.7). Using the Green's function method
we calculate the polarization P, magnetization M, and the critical temperatures T_C
and T_N as the temperatures where P and M vanish. The relative polarization P
obtain from Eq. (3.20) while the relative magnetization M for arbitrary spin value S
is introduced in Eq. (3.35) with the spin-wave energy in Eq. (3.24).

3.6.2. Discussions of the phase diagrams

From the model presented in previous section we can obtain the properties around
the magnetic and ferroelectric critical temperatures, T_N and T_C, and in the phase
where magnetic and ferroelectric properties coexist. Moreover, taking into account
the single-ion anisotropy this model can be applied in the whole temperature interval
and can describe the correct dependence of T_N, T_C and T_1 on the Fe- and Co-ion
doping concentration.
At first, we study the influence of doping with the non-magnetic ions Zn^{2+} and Mg^{2+}.
Their radii (0.88 and 0.86 $\mathring{A}$) are larger compared to the ion radius of Mn^{2+} (0.81 $\mathring{A}$).
This leads to tensile strain and to smaller magnetic and electric exchange interaction
constants $J_d < J$, $J_d' < J'$. The results for the critical temperatures T_N (black curve)
and T_C (red curve) for $Mn_{1-x}Zn_x WO_4$ are shown in Fig. 3.22. It can be seen that
they decrease with increasing the Zn-concentration. This is in agreement with the
experimental data of Chaudhury et al. [136] and Meddar et al. [139]. For Mg-doping
the behavior is comparable.
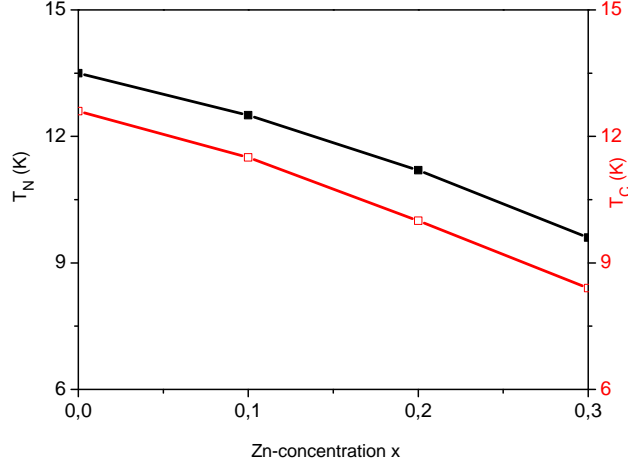
Figure 3.22. – Zn-concentration dependence x of the (black) magnetic T$_N$ and (red) ferroelectric T$_C$ transition temperatures in Mn$_{1-x}$Zn$_x$WO$_4$ with J^{Mn} = -12.2 K, $J_d^{Mn} = 0.8 J^{Mn}$, $D_d^{Mn} = D^{Mn}$ = -5 K, J^{Zn-Mn} = -6 K, $J_d' = 0.8 J' = 8$ K.

By the Fe and Co-doping we observe the opposite result for the magnetic transition temperature T$_N$. The ionic radii of Fe^{2+} and Co^{2+} (75 and 79 $\mathring{A}$) are smaller in comparison to the Mn-ion radius. This leads to a compressive strain, i.e. to $J_d > J$. In Fig. 3.23 is demonstrated the Fe-concentration (x) dependence of the magnetic transition temperature T$_N$ (black curve), it increases with increasing of x. A similar dependence was obtained also for Co-doping. The increase of T$_N$ is stronger compared to the Fe-doping, because exchange energies for Co^{2+} are typically much larger than for Fe^{2+}. This behavior is experimentally reported by many authors [96, 135, 136, 143]. For the ferroelectric transition temperature T$_C$ (red curve) we obtain a small decrease with increasing Fe- and Co-ion doping concentration.

In order to explain the experimentally observed differences in the T_1 behavior by Fe- and Co-ion doping, we must take into account the single-ion anisotropy D [27–29, 68, 135, 146–148]. The substitution of magnetic transition metal (TM) Fe^{2+} (S = 2) or Co^{2+} ($S = 3/2$) ions for Mn^{2+} ($S = 5/2$), which introduces extra Mn-TM ($J^{Mn-Fe} < 0$, $J^{Mn-Co} > 0$) and TM-TM (TM = Fe, Co, $J^{Fe-Fe} > 0$, $J^{Co-Co} > 0$) spin interactions, along with a different local magnetic anisotropy D determined by the TM^{2+} ions, modifies the phase competition. Additively, there is a competition between the influence of the exchange interaction constant J, which enhances the magnetization, T$_N$ and the spin-wave energy, and D, which reduces them [148].

It is also important that the single-ion anisotropy is of different sign for Fe and Co and that in Fe is at least one order of magnitude larger than in Co [149, 150]. In the case of the Fe-doping (Fig. 3.23) all this leads to an increasing the transition temperature T$_1$ (blue curve) which reaches the ferroelectric T$_C$ curve, i.e. the Fe-doping would stabilize the AF1 order. Contrary, by the Co-ion doping (Fig. 3.24) T$_1$ (blue curve) would decrease with increasing Co-concentration, i.e. it would suppress the AF1 state and stabilize the spin-spiral AF2 magnetic structure. This behavior is in
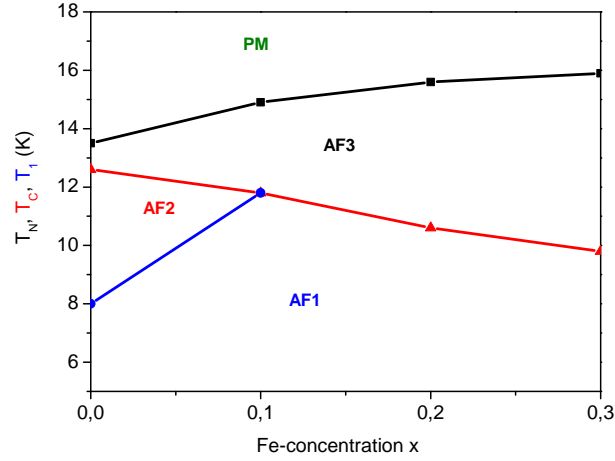
Figure 3.23. – Fe-concentration (x) dependence of the transition temperatures (black) T_N, (red) T_C and (blue) T_1 in $Mn_{1-x}Fe_xWO_4$ with $J^{Mn} = -12.2$ K, $J_d^{Mn} = 1.2J^{Mn}$, $D_d^{Mn} = 0.8D^{Mn}$, $J^{Fe} = 30$ K, $D^{Fe} = -24$ K, $J^{Fe-Mn} = -21$ K.
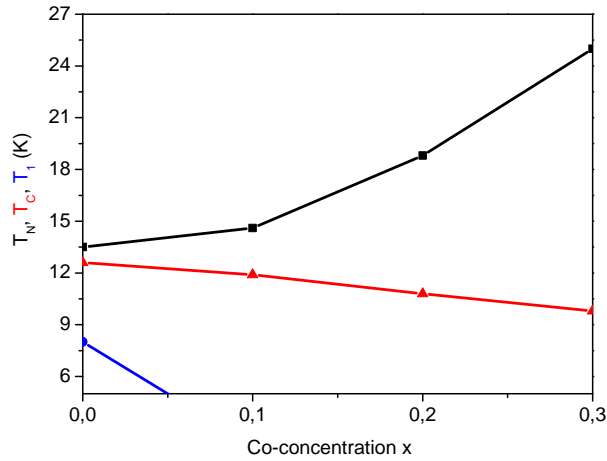
Figure 3.24. – Co-concentration dependence x of the transition temperatures (black) T_N, (red) T_C and (blue) T_1 in $Mn_{1-x}Co_xWO_4$ with $J^{Mn} = -12.2$ K, $J_d^{Mn} = 1.5J^{Mn}$, $D_d^{Mn} = 1.4D^{Mn}$, $J^{Co} = 49.5$ K, $D^{Co} = 12$ K, $J^{Co-Mn} = 30$ K.

agreement with that reported in [96, 135, 136, 143]. Moreover, in $MnWO_4$, as in many other multiferroics, the spin-phonon interaction is strong and plays an important role [151, 152]. Therefore, it must be taken into account in order to obtain correct results. It would contribute also to clarify whether the origin of the polarization is electric or ionic.

4. Theoretical study of multiferroic thin films and nanostructures

Nowadays, the formation and fabrication of very small structures and the characterization of their functional properties at the nanoscale are demanding tasks. In between, the field of multiferroics is notably of interest, since the effect of size reduction on the magnetic and ferroelectric properties is not necessarily the same. In such multifunctional materials, the manner in which the properties scale with the structure size as well as how the coupling behaves when size is decreased, are particularly important for any potential application.

Multiferroic thin films and nanostructures have been produced using a wide variety of growth techniques including sputtering, spin coating, pulsed laser deposition, molecular beam epitaxy, and more. Thin films including the hexagonal manganites and Bi and Pb based perovskites are the most studied single phase multiferroics. One of the earliest multiferroic to be investigated in thin film form was the hexagonal manganite $YMnO_3$(YMO) [153]. Although the thin film and bulk properties of YMO are qualitatively similar, the thin film samples typically show a reduction in the ferroelectric polarization and dielectric response compared with the corresponding single crystal values.

Experimental results reveal that thin film multiferroics can exhibit a large spontaneous polarization as well. The magnetic properties can also be significantly different from those of the bulk. Perovskite-structure bismuth ferrite is the most studied single-component multiferroic. $BiFeO_3$ has long been known to be a G-type antiferromagnet. It reveals a spontaneous polarization of 6.1 μCcm^{-2} along the [111]-direction. In 2003, Wang et al. reported enhancements of polarization and related properties in heteroepitaxially constrained thin films of BFO [154]. Most importantly, this report indicated a magnetoelectric coupling coefficient as high as 3 V cm Oe^{-1} at zero field as well as intensification of the polarization up to 90 μCcm^{-2} at room temperature and enhanced thickness-dependent magnetism compared to bulk samples. Enhanced multiferroicity could also exist on the nanoscale. Large coupling effects have been observed as well; for example in nanopillar heterostructures, switching of the ferroelectric polarization by an applied electric field leads to a reversal of the magnetization direction [155]. In spite of sufficient experimental findings a microscopic model describing the situation is still missing. Here we investigate a theoretical model to explain the multiferroics thin films and nanoparticles behavior.

4.1. General Hamiltonian for multiferroics in low dimensions

Similar to the bulk model, the Hamiltonian of the whole system is comprises of three parts

$$H = H_m + H_f + H_{mf} . \tag{4.1}$$

For a film consisting of n layers parallel to its surface, the effective spin Hamiltonian has the form

$$H_m = -\sum_{\alpha,\beta} \sum_{i\in\alpha, j\in\beta} J_{\alpha i,\beta j}[S^+_{\alpha i}S^-_{\beta j} + S^z_{\alpha i}S^z_{\beta j}] - \sum_\alpha \sum_i D_{\alpha i}(S^z_{\alpha i})^2 - h\sum_\alpha \sum_i S^z_{\alpha i} . \tag{4.2}$$

Our calculations are related to a rectangular coordinate system. The x-axis coincides with the normal direction of the film and the z-axis with the quantization axis of our spin system. $S^\gamma_{\alpha i}$ denotes the γ-component of the spin operator $S_{\alpha i}$, at the lattice point $R_{\alpha i}$. The first index α characterizes each layer (α = 1, 2,. . . , N), the second index i a lattice point in the layer α. The external magnetic field is denoted as $h = g\mu_B B$.

H_f is the electric part which given by TIM (Eq. (3.4)). Recently the applicability of this model was extended to thin films [111, 156] and nanoparticles [157]. The magnetoelectric coupling is H_{mf} described either by Eq. (3.6) or (3.7) based on the behavior of the system. Surface and size effects in multiferroelectric nanoparticles and thin films modify the interaction parameter between nearest neighbors for bulk and surface components. Likewise the tunneling frequency Ω in Eq. (3.4) is different for bulk and surface atoms. This can be included by different coupling parameters for the free surface layers, denoted by Ω_s and J_s and D_s, respectively. The related parameters for the bulk are written as Ω_b, D_b and J_b. The exchange interaction $J_{ij} = J(r_i - r_j)$ depends on the distance between the spins, i.e. on the lattice parameter, on the lattice symmetry and on the number of next nearest neighbors. This is very important for investigations of surface and ion doping effects. The Curie temperature is connected with the exchange interaction constant. The Hamiltonian of the TIM includes both
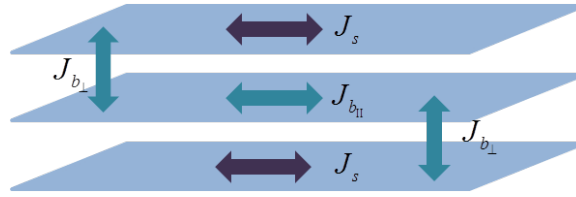
Figure 4.1. – Scheme for a ferroelectric thin film with three layers.

bulk and surface properties reads

$$H_f = -\frac{1}{2}\sum_{\alpha,\beta} \sum_{i\in\alpha, j\in\beta} J'_{\alpha i,\beta j}B^z_{\alpha i}B^z_{\beta j} - 2\Omega_\alpha \sum_{i,\alpha} B^x_{\alpha i} . \tag{4.3}$$

As in the pure bulk case, a new coordinate system is reached by rotating the original one with the angle ν in the xz-plane. The three dimensional system of N layers in
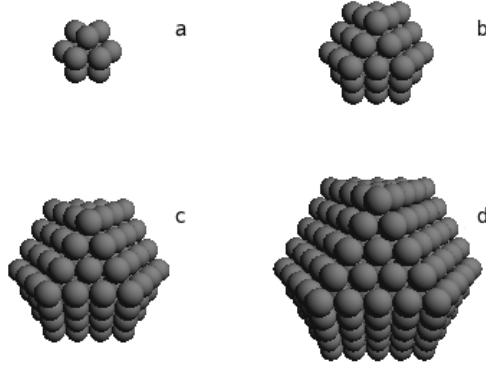
Figure 4.2. – Array of nanoparticles composed of different shells. Each sphere repre-
sents a spin situated in the center, where (a) Consists of one central spin plus N=1
shell, (b) N=2, (c) N=3, and (d) N=4 [158].

z-direction on a simple cubic lattice is shown schematically in Fig. 4.1. The layers
are numbered by n = 1, ...N, where the layers n = 1 and n = N represent the two
surfaces of the system with the modified coupling parameters J_s and Ω_s. The bulk is
established by the remaining (N - 2) layers.
The study of materials with no translational symmetry is greatly detained by a lack
of detailed knowledge of its structure. A good starting point for the discussion of the
arrangement of atoms is the packing of spheres. A nanoparticle is defined by fixing
the origin at a certain (pseudo) spin in the center of the particle and including all
other (pseudo) spins within the particle into shells as it shown in Fig. 4.2. The shells
are numbered by $n' = 0, ..., N$, where $n' = 0$ denotes the central spin and $n' = N$
represents the surface shell of the system. Hence the number N is a measure of the
extension of the NP. The real size of the NP is obtained by multiplying N with the
lattice constant. The surface effects are included by different coupling parameters
within the surface shell and within the bulk, denoted with the indices 's' and 'b',
respectively. Similarly, the magnetoelectric coupling is introduced as

$$H_{mf} = -\sum_{\alpha,\beta} \sum_{i,j,r,f} K_{\alpha\beta} B_{\alpha r}^z B_{\beta f}^z \mathbf{S}_{\alpha i} \cdot \mathbf{S}_{\beta j} \, . \tag{4.4}$$

4.2. Green's function approach to thin films

We introduce the double-time temperature-dependent retarded Green's function
$G(t - t')$ for thermodynamical equilibrium as

$$G_{\varphi m \phi l}(t - t') = \langle\langle S_{\varphi m}^+(t); S_{\phi l}^-(t')\rangle\rangle \, . \tag{4.5}$$

This Green function satisfies the equation of motion

$$i\frac{dG_{\varphi m \phi l}}{dt} = \delta(t - t')\langle[S^+{}_{\varphi m}, S^-{}_{\phi l}]\rangle + \langle\langle[S^+{}_{\varphi m}, H]; S^-{}_{\phi l}\rangle\rangle \, . \tag{4.6}$$

Here $H = H_m + H_{mf}$. Using RPA, the explicit form of the equation of motion is

$$\langle\langle S^+_{\varphi m}; S^-_{\phi l}\rangle\rangle = 2\langle S^z_{\varphi m}\rangle\delta_{\varphi\phi}\delta_{lm} - 2\sum_{\alpha}\sum_{i\in\alpha} J^{eff}_{\alpha i\varphi m}\langle S^z_{\varphi m}\rangle\langle\langle S^+_{\alpha i}; S^-_{\phi l}\rangle\rangle+$$

$$2\sum_{\alpha}\sum_{i\in\alpha} J^{eff}_{\alpha i\varphi m}\langle S^z_{\alpha i}\rangle\langle\langle S^+_{\varphi m}; S^-_{\phi l}\rangle\rangle, \tag{4.7}$$

$$J^{eff} = J + 2K_{\alpha\beta}\langle B_{r\alpha}\rangle\langle B_{f\beta}\rangle\cos\nu_\alpha\cos\nu_\beta\,.$$

Taking into account the periodic boundary conditions in the film plane, the quantity $\langle S^z_{\varphi m}\rangle$ is independent of the index m and we can expand the Fourier transform into a two dimensional Fourier series

$$G_{\varphi m\phi l}(\omega) = \frac{1}{N'}\sum_{K_\parallel} e^{i\mathbf{k}_\parallel(R_m - R_l)}G_{\varphi\phi}(\mathbf{K}_\parallel, \omega)\,. \tag{4.8}$$

Here N' is the number of sites in any of the lattice planes, R_m represents the position vectors of site m; $\mathbf{k}_\parallel$ is a two-dimensional wave vector parallel to the surface. The summation is taken over the two dimensional first Brillouin zone. From Eq. (4.7) we get a system of N equations for the N unknown quantities $G^{\mathbf{k}_\parallel}_{\varphi\phi}$ ($\varphi = 1,2, \ldots$, N), which can be rewritten in the following matrix form

$$\mathbf{H}(\omega)\mathbf{G}(\mathbf{k}_\parallel, \omega) = \mathbf{R}, \tag{4.9}$$

$\mathbf{H}$ can be expressed as:

$$\mathbf{H} = \begin{pmatrix} \omega - V_1 & k_1 & 0 & 0 & 0 & 0 & \ldots \\ k_2 & \omega - V_2 & k_2 & 0 & 0 & 0 & \ldots \\ 0 & k_3 & \omega - V_3 & k_3 & 0 & 0 & \ldots \\ \vdots & \vdots & \vdots & \vdots & \vdots & \vdots & \ddots \\ 0 & 0 & 0 & 0 & 0 & k_N & \omega - V_N \end{pmatrix}, \tag{4.10}$$

with

$$K_n = 2J^{eff\,(b)}_\perp(\mathbf{k}_\parallel)\langle S^z_\varphi\rangle\,, \quad n = 1, 2, \ldots\ldots, N\,,$$

$$V_1 = h + 2\big[\langle S^z_1\rangle[J^{eff\,(s)}_\parallel(0) - J^{eff\,(s)}_\parallel(\mathbf{k}_\parallel)] + J^{eff\,(s)}_\perp(0)\sum_{<\alpha,\neq\underline{1}>}\langle S^z_\alpha\rangle\big]\,,$$

$$V_\varphi = h + 2\big[\langle S^z_\varphi\rangle[J^{eff\,(b)}_\parallel(0) - J^{eff\,(b)}_\parallel(\mathbf{k}_\parallel)] + J^{eff\,(b)}_\perp(0)\sum_{<\alpha,\neq\underline{\varphi}>}\langle S^z_\alpha\rangle\big]\,, \tag{4.11}$$

$$V_N = h + 2\big[\langle S^z_N\rangle[J^{eff\,(s)}_\parallel(0) - J^{eff\,(s)}_\parallel(\mathbf{k}_\parallel)] + J^{eff\,(s)}_\perp(0)\sum_{<\alpha,\neq\underline{N}>}\langle S^z_\alpha\rangle\big]\,,$$

$$\bar{m}_{\mathbf{q}_\parallel} = \langle S^-_{\mathbf{q}_\parallel}S^+_{\mathbf{q}_\parallel}\rangle\,, \quad \varphi = 2, 3, \ldots\ldots, n - 1\,,$$

where the underlined indices are fixed. Here $J^{eff}_\parallel$ denotes the exchange integral between neighboring lattice points situated in the same layer, whereas $J^{eff}_\perp$ stands

for the exchange integral of two lattice points lying in neighboring layers. In the following, we consider these two quantities to be equivalent.

$$
\begin{aligned}
J_{\parallel}^{eff}(\mathbf{k}_{\parallel}) &= \frac{1}{N'} \sum_{\underline{m \in \varphi, i \in \varphi}} J_{\parallel}^{eff}(i,m) e^{i\mathbf{k}_{\parallel}(R_i - R_m)}, \\
J_{\perp}^{eff}(\mathbf{k}_{\parallel}) &= \frac{1}{N'} \sum_{\underline{m \in \varphi, i \in \varphi+1}} J_{\perp}^{eff}(i,m) e^{i\mathbf{k}_{\parallel}(R_i - R_m)} .
\end{aligned}
\tag{4.12}
$$

In order to obtain the solutions of the matrix Eq. (4.9), we introduce the two-dimensional column matrices, $\mathbf{G}_m$ and $\mathbf{R}_m$, where the elements are given by $(\mathbf{G}_n)_m = G_{mn}$ and $(\mathbf{R}_n)_m = P_n \delta_{mn}$, so that Eq. (4.9) yields

$$
\mathbf{H}(\omega)\mathbf{G}_n = \mathbf{R}_n. \tag{4.13}
$$

From Eq. (4.13), $G_{nn}(\omega)$ is obtained as

$$
G_{nn}(\omega) = \frac{|H_{nn}(\omega)|}{|\,H(\omega)\,|} . \tag{4.14}
$$

The quantity $|H_{nn}(\omega)|$ is the determinant made by replacing the n-th column of the determinant $|H(\omega)|$ by R_n. E_n^m, are the poles of the Green's function $G_{nn}(\omega)$, can be calculated by solving $|H(\omega)| = 0$. The thermal average of a spin in the n-th layer for arbitrary magnitude of S is given by Eq. (3.35)

$$
\langle M_n \rangle = \frac{1}{N'} \sum_{\mathbf{k}_{\parallel}} \left[(S + 0.5) \coth[(S + 0.5)\beta E_n^m(\mathbf{k}_{\parallel})] - 0.5 \coth(0.5\beta E_n^m(\mathbf{k}_{\parallel})) \right]. \tag{4.15}
$$

The total relative magnetization reads

$$
M = \frac{1}{N} \sum_{n=1}^{N} M_n . \tag{4.16}
$$

In a similar way, for the ferroic subsystem the matrix components of Eq. (4.10) are

$$
\begin{aligned}
k_n &= J_n'^{eff} P_n \sin^2 \nu_n, \quad n=1,...,N, \\
V_n &= 2\Omega_n \sin \nu_n + \frac{1}{2} P_n J_n'^{eff} \cos^2 \nu_n - \frac{P_n J_n'^{eff}}{4} \sin^2 \nu_n \gamma(\mathbf{k}_{\parallel}) + J_{n-1}'^{eff} P_{n-1} \cos^2 \nu_{n-1} \\
&\quad + J_{n+1}'^{eff} P_{n+1} \cos^2 \nu_{n+1} - \frac{J_n'^{eff}}{P_n N} \sum_{\mathbf{q}_{\parallel}} [\gamma(\mathbf{q}_{\parallel}) \cos^2 \nu_n - 0.5\gamma(\mathbf{k}_{\parallel} - \mathbf{q}_{\parallel}) \sin^2 \nu_n] \bar{n}_n(\mathbf{q}_{\parallel}) \\
&\quad - \frac{J_{n-1}'^{eff}}{P_{n-1} N} \sum_{\mathbf{q}_{\parallel}} \gamma(\mathbf{q}_{\parallel}) \cos^2 \nu_{n-1} \bar{n}_{n-1}(\mathbf{q}_{\parallel}) - \frac{J_{n+1}'^{eff}}{P_{n+1} N} \sum_{\mathbf{q}_{\parallel}} \gamma(\mathbf{q}_{\parallel}) \cos^2 \nu_{n+1} \bar{n}_{n+1}(\mathbf{q}_{\parallel}), \\
J_n'^{eff} &= J_n' + 2K_n(\langle S^+ S^- \rangle + \langle S^z S^z \rangle)_n, \quad \gamma(\mathbf{k}_{\parallel}) = \frac{1}{2}(\cos(k_x a) + \cos(k_y a)), \\
n(\mathbf{q}_{\parallel}) &= \langle b_{\mathbf{q}_{\parallel}}^\dagger b_{\mathbf{q}_{\parallel}} \rangle.
\end{aligned}
\tag{4.17}
$$

Here we have $J_1' \equiv J_N' = J_s'$, $J_n' = J_b'$ for $n = 2, 3, 4, ..., N - 1$, $\Omega_1 = \Omega_N = \Omega_s$, $\Omega_n = \Omega_b$ ($n = 2, 3, 4, ..., N - 1$), $J_0' = J_{N+1}' = 0$. The quantity $P_n(T)$ is the relative polarization in each layer n in the direction of the mean field and is equal to $2\langle B^z \rangle$. The correlation function is

$$\langle b_{\mathbf{k}_\parallel}^\dagger b_{\mathbf{k}_\parallel} \rangle_n = \frac{P_n}{2} \left[\frac{P_n J_n'^{eff}}{2 E_n^f(\mathbf{k}_\parallel)} (1 - 0.5 \sin^2 \nu_n \gamma(\mathbf{k}_\parallel)) \coth \frac{E_n^f}{2T} - 1 \right]. \tag{4.18}$$

Hence, the relative polarization in the n-th layer is given by

$$P_n = \left(\frac{P_n J'^{eff}}{2N} \sum_{\mathbf{k}_\parallel} \frac{1 - 0.5 \sin^2 \nu_n \gamma(\mathbf{k}_\parallel)}{E_n^f} \coth \frac{E_n^f}{2T} \right)^{-1}. \tag{4.19}$$

The solution for Eq. (4.19) has to be evaluated numerically. Due to the assumption of symmetrical surfaces, there are $\frac{1}{2}N$ layer polarizations. Eq. (4.19) must be solved self-consistently.

In order to investigate the phonon spectrum and take into account the experimentally obtained strong spin-phonon coupling observed in some multiferroics, we have to include the following terms in the Hamiltonian in Eq. 4.1

$$H' = H_{ph} + H_{mph} + H_{fph}. \tag{4.20}$$

The first term H_{ph} contains the lattice vibrations, H_{fph} and H_{mph} describe the interaction of the pseudospins of the ferroelectric subsystem and of the magnetic spins with the phonons. These terms are very important in order to explain the experimental data of Raman and IR spectroscopy lines in multiferroics. For the approximate calculation of the phonon Green's function we follow the line proposed in [75]. The retarded phonon Green's function $\langle\langle a_i(t); a_j^\dagger(0) \rangle\rangle$ has a matrix form define as

$$\mathbf{H} = \begin{pmatrix} \omega - (W_1 - i\Gamma_1) & k_1 & 0 & 0 & 0 & 0 & \cdots \\ k_2 & \omega - (W_2 - i\Gamma_2) & k_2 & 0 & 0 & 0 & \cdots \\ 0 & k_3 & \omega - (W_3 - i\Gamma_3) & k_3 & 0 & 0 & \cdots \\ \vdots & \vdots & \vdots & \vdots & \vdots & \vdots & \ddots \\ 0 & 0 & 0 & 0 & 0 & k_N & \omega - (W_N - i\Gamma_N) \end{pmatrix}$$

with

$$K_n = 2 P_n \cos \nu_n R_n^f + M_n R_n^m, \quad n = 1, 2, ..., N,$$

$$W_N = \omega_0(\mathbf{k}_\parallel) + B_n(\mathbf{k}_\parallel) \langle Q_n(\mathbf{k}_\parallel) \rangle \delta_{\mathbf{k}_\parallel, 0} + 0.5 \sum_{\mathbf{q}_\parallel} A_n(\mathbf{k}_\parallel, \mathbf{q}_\parallel)(2\bar{N}_n(\mathbf{q}_\parallel) + 1)$$

$$- 0.5 P_n \cos \nu_n R_n^f(\mathbf{k}_\parallel) - M_n R_n^m(\mathbf{k}_\parallel),$$

$$\langle Q_n(\mathbf{k}_\parallel) \rangle = \left(0.5 P_n \cos \nu_n F_n^f(\mathbf{k}_\parallel) + M F_n^m(\mathbf{k}_\parallel) - \frac{1}{N'} \sum_{\mathbf{q}_\parallel} B_n(\mathbf{k}_\parallel, \mathbf{q}_\parallel)[2\bar{N}_n(\mathbf{q}_\parallel) + 1] \right) \times$$

$$\left(\omega_0(\mathbf{k}_\parallel) - 0.5 R_n^f(\mathbf{k}_\parallel) p_n \cos \nu_n + \frac{1}{N'} \sum_{\mathbf{q}_\parallel} A_n(\mathbf{k}_\parallel, \mathbf{q}_\parallel)[2\bar{N}_n(\mathbf{q}_\parallel) + 1] \right)^{-1},$$

$$\bar{N}_n(\mathbf{q}_\parallel) = \langle a_{\mathbf{q}_\parallel}^+ a_{\mathbf{q}_\parallel}^- \rangle. \tag{4.21}$$

The damping is defined as

$$\Gamma_n = \Gamma_n^{ph-ph} + \Gamma_n^{m-ph} + \Gamma_n^{f-ph}\,. \tag{4.22}$$

Γ_n^{m-ph} and Γ_n^{f-ph} is the damping part which comes from the spin-phonon and pseudospin-phonon interaction and Γ_n^{ph-ph} is the phonon damping due to the phonon-phonon anharmonic interaction. We have

$$
\begin{aligned}
\Gamma_n^{ph-ph} =& \frac{9\pi}{N'} \sum_{\mathbf{q}_\parallel} B_n^2(\mathbf{k}_\parallel, \mathbf{q}_\parallel) \left[\bar{N}_n(\mathbf{q}_\parallel) - \bar{N}_n(\mathbf{k}_\parallel - \mathbf{q}_\parallel) \right] \{ \delta \left[\omega_n(\mathbf{q}_\parallel) - \omega_n(\mathbf{k}_\parallel - \mathbf{q}_\parallel) - \omega_n(\mathbf{q}_\parallel) \right] \\
&- \delta \left[\omega_n(\mathbf{k}_\parallel - \mathbf{q}_\parallel) - \omega_n(\mathbf{q}_\parallel) - \omega_n(\mathbf{k}_\parallel) \right] \} + \frac{16\pi}{N'^2} \sum_{\mathbf{q}_\parallel, \mathbf{p}_\parallel} A_n^2(\mathbf{k}_\parallel, \mathbf{q}_\parallel, \mathbf{p}_\parallel) \{ \bar{N}_n(\mathbf{p}_\parallel) \\
&\times \left[1 + \bar{N}_n(\mathbf{q}_\parallel) + \bar{N}_n(\mathbf{p}_\parallel + \mathbf{k}_\parallel - \mathbf{q}_\parallel) \right] - \bar{N}_n(\mathbf{q}_\parallel) \bar{N}_n(\mathbf{p}_\parallel + \mathbf{k}_\parallel - \mathbf{q}_\parallel) \} \delta \left[\omega_n(\mathbf{q}_\parallel) \right. \\
&\left. + \omega_n(\mathbf{p}_\parallel + \mathbf{k}_\parallel - \mathbf{q}_\parallel) - \omega_n(\mathbf{p}_\parallel) - \omega_n(\mathbf{k}_\parallel) \right],
\end{aligned} \tag{4.23}
$$

$$
\begin{aligned}
\Gamma_n^{m-ph} =& \frac{4\pi M^2}{N'} \sum_{\mathbf{q}_\parallel} (F_n^m)^2(\mathbf{k}_\parallel, \mathbf{q}_\parallel)(\bar{m}_q - \bar{m}_{\mathbf{q}_\parallel - \mathbf{k}_\parallel}) \delta \left[E_n^m(\mathbf{q}_\parallel - \mathbf{k}_\parallel) - E_n^m(\mathbf{q}_\parallel) - \omega_n(\mathbf{k}_\parallel) \right] \\
&+ \frac{4\pi M^2}{N'^2} \sum_{\mathbf{q}_\parallel, \mathbf{p}_\parallel} (R_n^m)^2(\mathbf{k}_\parallel, \mathbf{q}_\parallel) \left(\bar{m}_n(\mathbf{q}_\parallel) - \bar{m}_n(\mathbf{p}_\parallel) \right) \{ \left[1 + \bar{N}_n(\mathbf{k}_\parallel + \mathbf{p}_\parallel - \mathbf{q}_\parallel) \right] \delta \left[E_n^m(\mathbf{p}_\parallel) \right. \\
&\left. - E_n^m(\mathbf{q}_\parallel) - \omega_n(\mathbf{k}_\parallel + \mathbf{p}_\parallel - \mathbf{q}_\parallel) + \omega_n(\mathbf{k}_\parallel) \right] + \bar{N}_n(\mathbf{q}_\parallel - \mathbf{p}_\parallel - \mathbf{k}_\parallel) \delta \left[E_n^m(\mathbf{p}_\parallel) - E_n^m(\mathbf{q}_\parallel) \right. \\
&\left. + \omega_n(\mathbf{k}_\parallel) + \omega_n(\mathbf{q}_\parallel - \mathbf{k}_\parallel - \mathbf{p}_\parallel) \right] \} + \frac{\pi}{N'^2} \sum_{\mathbf{q}_\parallel, \mathbf{p}_\parallel} (R_n^m)^2(\mathbf{k}_\parallel, \mathbf{q}_\parallel, \mathbf{p}_\parallel) \langle S_n^z \rangle^4 \delta_{\mathbf{q}_\parallel, 0} \delta_{\mathbf{p}_\parallel, 0} \\
&\times \{ \delta \left[E_n^m(\mathbf{p}_\parallel) - E_n^m(\mathbf{q}_\parallel) - \omega_n(\mathbf{k}_\parallel + \mathbf{p}_\parallel - \mathbf{q}_\parallel) + \omega_n(\mathbf{k}_\parallel) \right] - \delta \left[E_n^m(\mathbf{p}_\parallel) - E_n^m(\mathbf{q}_\parallel) \right. \\
&\left. + \omega_n(\mathbf{q}_\parallel - \mathbf{k}_\parallel - \mathbf{p}_\parallel) + \omega_n(\mathbf{k}_\parallel) \right] \},
\end{aligned} \tag{4.24}
$$

and

$$
\begin{aligned}
\Gamma_n^{f-ph} =& \frac{\pi P_n \sin^2 \nu_n}{4} (F_n^f)^2(\mathbf{k}_\parallel) \delta [E_n^f(\mathbf{k}_\parallel) - \omega_n(\mathbf{k}_\parallel)] + \frac{\pi P_n \cos^2 \nu_n}{N'^2} \sum_{\mathbf{q}_\parallel, \mathbf{p}_\parallel} (R_n^f)^2(\mathbf{k}_\parallel, \mathbf{q}_\parallel) \{ \bar{n}_n(\mathbf{p}_\parallel) \\
&\left[1 + \bar{N}_n(\mathbf{q}_\parallel) + \bar{n}_n(\mathbf{p}_\parallel + \mathbf{k}_\parallel - \mathbf{q}_\parallel) \right] - \bar{N}_n(\mathbf{q}_\parallel) \bar{n}_n(\mathbf{p}_\parallel + \mathbf{k}_\parallel - \mathbf{q}_\parallel) \} \delta [\omega_n(\mathbf{q}_\parallel) - E_n^f(\mathbf{p}_\parallel) \\
&+ E_n^f(\mathbf{p}_\parallel + \mathbf{k}_\parallel - \mathbf{q}_\parallel) - \omega_n(\mathbf{k}_\parallel)] + \frac{\pi P_n \sin^2 \nu_n}{4N'} \sum_{\mathbf{q}_\parallel} (R_n^f)^2(\mathbf{k}_\parallel, \mathbf{q}_\parallel) \{ [\bar{N}_n(\mathbf{q}_\parallel) \\
&- \bar{n}_n(\mathbf{k}_\parallel - \mathbf{q}_\parallel)] \delta [\omega_n(\mathbf{q}_\parallel) - E_n^f(\mathbf{k}_\parallel - \mathbf{q}_\parallel) - \omega_n(\mathbf{k}_\parallel)] + [1 + \bar{N}_n(\mathbf{q}_\parallel) + \bar{n}_n(\mathbf{k}_\parallel - \mathbf{q}_\parallel)] \times \\
&\delta [\omega_n(\mathbf{q}_\parallel) + E_n^f(\mathbf{k}_\parallel - \mathbf{q}_\parallel) + -\omega_n(\mathbf{k}_\parallel)] \}\,.
\end{aligned} \tag{4.25}
$$

For the phonon energy in the n-th layer we obtain

$$
\begin{aligned}
\omega_n^2(\mathbf{k}_\parallel) =& [\omega_0(\mathbf{k}_\parallel)]^2 - 2\omega_0(\mathbf{k}_\parallel)\left(\frac{P_n\cos\nu_n}{2}R_n^f(\mathbf{k}_\parallel) + M^2 R_n^m(\mathbf{k}_\parallel)\right.\\
&\left. - \frac{1}{2N}\sum_{\mathbf{q}_\parallel}A_n(\mathbf{k}_\parallel,\mathbf{q}_\parallel)[2\bar{N}_n(\mathbf{q}_\parallel)+1] - B_n(\mathbf{k}_\parallel)\langle Q_n(\mathbf{k}_\parallel)\rangle\delta_{\mathbf{k}_\parallel 0}\right).
\end{aligned}
\tag{4.26}
$$

Considering phonon effects, the interaction J'^{eff} in Eq. (4.17) should be replaced by

$$
J'^{eff} = J'^{eff} + \frac{2F_0^f F_k^f \delta_{k0}}{\omega_k - P\cos\nu R_k^f + 0.5A_k},
\tag{4.27}
$$

which is now temperature-dependent. The anharmonicity phonon-phonon parameter $A(\mathbf{k}_\parallel)$ will decrease the effective exchange coupling J'_{eff}, while the pseudospin-lattice coupling constants $F^f(\mathbf{k}_\parallel)$ and $R^f(\mathbf{k}_\parallel)$ will increase its value. This should applies in a similar way to the magnetic exchange interaction, J.

4.3. Green's function approach to nanoparticles

Due to the lack of translational invariance in nanosized systems, the Green's function calculation has to be performed in the real space. As a result, the average is defined in the conventional way as

$$
\langle S^z\rangle = \frac{TrS^z exp(-\beta H)}{Trexp(-\beta H)}.
\tag{4.28}
$$

Following the same approach as the one in bulk and thin film systems, we consider a system of two sublattices as Eq. (4.1). The magnetic Hamiltonian is simply reads

$$
H_m = -\frac{1}{2}\sum_{i,j}J_{ij}(S_i^+ S_j^- + S_i^z S_j^z) - \sum_i D_i(S_i^z)^2 - h\sum_i S_i^z.
\tag{4.29}
$$

The relative magnetization M is observed

$$
M = \langle S^z\rangle = \frac{1}{N}\sum_n\left[(S+0.5)\coth[(S+0.5)\beta E_n^m] - 0.5\coth(0.5\beta E_n^m)\right],
\tag{4.30}
$$

where N is the number of shells. E_n^m is the energy of elementary spin excitations of a given shell. Considering Eq. (3.6) is a coupling Hamiltonian, for the spin-excitation energies we obtain the following expression in the generalized Hartree-Fock approximation taking into account all correlation functions

$$
\begin{aligned}
E_{ij}^m =& \left(\frac{2}{N}\sum_m J_{im}^{eff}(\langle S_m^- S_i^+\rangle + 2\langle S_m^z S_i^z\rangle)\delta_{ij} - 2J_{ij}^{eff}(\langle S_i^- S_j^+\rangle + 2\langle S_i^z S_j^z\rangle)\right.\\
&\left. + 2D_i(2\langle S_i^z S_i^z\rangle - \langle S_i^- S_i^+\rangle)\delta_{ij} + 2g\mu_B H\langle S_i^z\rangle\delta_{ij}\right)/2\langle S_i^z\rangle\delta_{ij},
\end{aligned}
\tag{4.31}
$$

where N is the number of lattice sites and $J_{ij}^{eff} = J_{ij} + 2KP_iP_j \cos\nu_i \cos\nu_j$. If we neglect the transverse correlation functions $\langle S_i^- S_j^+ \rangle$ and decouple the longitudinal correlation functions $\langle S_i^z S_j^z \rangle \longrightarrow \langle S_i^z \rangle\langle S_j^z \rangle$ we obtain the energy in RPA

$$E_{ij}^m = g\mu_B H\delta_{ij} + \frac{2}{N}\sum_m J_{im}^{eff}\langle S_m^z\rangle\delta_{ij} - 2J_{ij}^{eff}\langle S_i^z\rangle + 2D_i\langle S_i^z\rangle\delta_{ij}\,. \tag{4.32}$$

The rotated Hamiltonian for the ferroic subsystem is written in the form

$$
\begin{aligned}
H_f = &- 2\Omega\sum_i \left(P_i\sin\nu + \frac{1}{2}(b_i + b_i^\dagger)\cos\nu_i\right) - 2\mu E\sum_i\left(P_i\cos\nu_i - \frac{1}{2}(b_i + b_i^\dagger)\sin\nu_i\right)\\
&- \frac{1}{2}\sum_{i,j} J'_{i,j}\Big(\cos\nu_i\cos\nu_j P_iP_j - \cos\nu_i\sin\nu_j(P_ib_j^\dagger + P_ib_j)\\
&+ \frac{1}{4}\sin\nu_i\sin\nu_j(b_i^\dagger + b_i)(b_j^\dagger + b_j)\Big)\,.
\end{aligned}
\tag{4.33}
$$

The equation of motion in RPA reads

$$
\begin{aligned}
E^f\langle\langle b_l; b_m^\dagger\rangle\rangle \equiv E^f G_{lm} = &2\langle P_l\rangle\delta_{lm} + \Big(2\Omega_l\sin\nu_l + 2\mu E\cos\nu_l + \sum_j J_{lj}^{'eff}\cos\nu_l\cos\nu_j\langle P_j\rangle\\
&+ \frac{1}{2}\sum_j J_{lj}^{'eff}\sin\nu_l\sin\nu_j\langle b_l b_j^\dagger\rangle\Big)G_{lm}\\
&- \frac{1}{2}\sum_j J_{lj}^{'eff}\Big(\sin\nu_l\sin\nu_j\langle P_l\rangle + 2\cos\nu_j\cos\nu_l\langle b_l b_j^\dagger\rangle\Big)G_{jm}\,.
\end{aligned}
\tag{4.34}
$$

This system of equations which will be treated in matrix representation in accordance with Eq. (4.9), has to be solved numerically. The soft-mode energy of the n-th shell, is obtained from

$$E_n^f = 2\Omega_n\sin\nu_n + \frac{1}{N}\sum_i J_{in}^{'eff}\cos\nu_n\cos\nu_i\langle B_i^z\rangle + \mu E\cos\nu_n\,, \tag{4.35}$$

where $J_{ij}^{'eff} = J'_{ij} + 2K(\langle S_i^+ S_j^-\rangle + \langle S_i^z S_j^z\rangle)$. Contrary to the bulk system, here one has to solve the coupled set of Eq. (4.34) in order to find the excitation energies and the on-site polarization. The damping of the spin-wave is

$$\Gamma_n = \frac{\pi}{4}\sum_i J_{il}^{'eff\,2}(\cos\nu_l\cos\nu_i - 0.5\sin\nu_l\sin\nu_i)^2\bar{n}_i(1 - \bar{n}_i)\delta(\omega_l - \omega_i + \omega_i - \omega_l)\,. \tag{4.36}$$

The rotation angle ν_l is given by

$$\langle[b_l, H]_-\rangle = \langle P_l\rangle\left(2\Omega\cos\nu_l - 2\mu E\sin\nu_l - \sin\nu_l\sum_i J_{il}^{'eff}P_i\cos\nu_i\right) = 0\,, \tag{4.37}$$

and leads to

$$\tan\nu_l = \frac{2\Omega_l}{\sum_i J^{'eff}{}_{il}\cos\nu_i\langle P_i\rangle + 2\mu E}\,. \tag{4.38}$$

This relation is valid in both regims, above ($\nu = \pi/2$) and below the phase transition temperature T_C. The relative polarization P_n for the n-th shell in the rotated frame, taking only the diagonal term of (4.34) into account, reads

$$P_n = \frac{1}{2} \tanh \frac{E_n^f}{2T} \, . \tag{4.39}$$

Here E_n^f is the transverse excitation energy, i.e. the soft mode energy of the n-th shell. The interaction energy J'_{ni} is determined by the interaction within each shell and the averaged number of nearest neighbors. In the following sections, we apply our model to explain the experimental behavior observed in multiferroic thin films and nanoparticles.

4.4. The magnetoelectric effect in double-perovskite thin films

As a new development of multiferroic materials, double-perovskite multiferroic compounds of the form $A_2BB'O_6$ have been theoretically and experimentally designed. The unit cell of double-perovskite structure is twice that of perovskite. The transition metal atoms B and B' are in the center of alternating oxygen octahedras. The cation A occupies the interstices between the octahedras (Fig. 4.3). To this group of material belong Bi_2NiMnO_6 (BNMO), Bi_2FeMnO_6 (BFMO), Bi_2CoMnO_6 (BCMO) and Bi_2FeCrO_6 (BFCO). Especially in BNMO the Bi^{3+} ion, located at the A site in the perovskite structure, gives rise to a structural distortion at $T_c = 485$ K which leads to ferroelectricity. On the other hand the B- and B'-site ordering of the Ni^{2+} and Mn^{4+} ions, respectively in a rock-salt configuration gives rise to a ferromagnetic behavior at the lower critical temperature ($T_N = 140$ K) [159]. Further experimental studies of BNMO thin films have confirmed the strong coupling between magnetic and ferroelectric phases [160–162]. Other studies of multiferroic Bi_2FeCrO_6 (BFCO) thin films have offered a similar behavior [163–165].
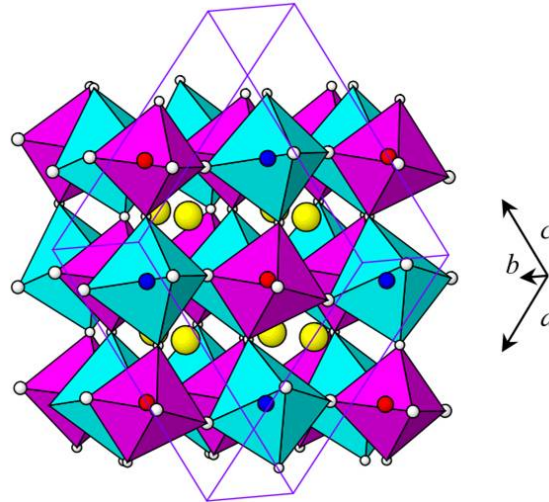
Figure 4.3. – Crystal structure of Bi_2 $NiMnO_6$. The blue octahedra correspond to NiO_6 and the red octahedra correspond to MnO_6. Bi ions are shown in yellow spheres. The monoclinic unit cell is superimposed. Taken from [166].

The first density functional studies for BNMO and Y_2NiMnO_6 (YNMO) have been presented in [167] and more recently in [168]. Temperature-dependent Raman measurements in BNMO thin films [169] reveal a softening below 140 K and a step-like anomaly in between 420-490 K of the main Raman peak frequency. This observation provides a strong evidence for the multiferroic behavior of the material. Furthermore, the results for thin films are similar to those of bulk materials. Infrared reflectance spectra of Bi_2FeCrO_6 thin films, reported in [170], yields similar results. One observes some phonon anomalies near to the phase transition.

In this section, we focus on the spin-phonon coupling. We demonstrate that such a coupling is quite relevant in the double-perovskite structure. In particular, the

influence of the magnetoelectric coupling on phonon excitation and its damping is analyzed.

4.4.1. The analytical representation of double-perovskite multiferroics

The Hamiltonian for the materials characterized above is written as a summation of Eq. (4.20) and Eq. (4.1). The electric part H_f, the magnetic subsystem H_m and the coupling H_{mf} are considered following Eqs. (4.2), (4.3) and (4.4). Because BNMO offers a great difference between the two critical temperatures we suggest likewise a biquadratic magnetoelectric coupling between the two order parameters. The coupling term implies that the magnetic and the ferroelectric subsystems are subjected to independent ordering mechanism which is manifested by well separated transition temperatures $T_c \gg T_N$ which is also relevant for BFO [171] as we discussed before. There is an evidence for a strong (pseudo) spin-lattice coupling in the double-perovskite multiferroics [169, 170, 172], therefore the total Hamiltonian in (4.1) is supplemented by the additional part

$$H' = H_{ph} + H_{fph} + H_{mph} \qquad (4.40)$$

representing the phonon part. Here H_{ph} describes the lattice vibrations in terms of the normal coordinates Q_i and the related frequency ω_{i0} as in Eq. (3.58). The remaining contributions H_{fph} and H_{mph} comprise the coupling between the pseudospins of the ferroelectric subsystem and of the magnetic spins with the phonons. This spin-phonon coupling is introduced in Eq. (3.61).

The complete system is analyzed by retarded Green's functions. Especially the phonon part is studied with the function defined by

$$G_{ij}(t) = \ll a_i(t); a_j^\dagger(0) \gg = -i\Theta(t)\langle[a_i(t), a_j^\dagger(0)]\rangle. \qquad (4.41)$$

Due to the coupling of the phonons to the electric as well as to the magnetic subsystem the phonon excitation energy is characterized by the polarization P, the magnetization M and the spin-phonon coupling parameters $R^{(f)}$ and $R^{(m)}$. The polarization and the magnetization are calculated self-consistently from the corresponding Green's functions for the ferroelectric and magnetic subsystem. In the same manner as the dispersion relation of the phonon system we get also the damping of the phonons according to Eq. (4.9).

4.4.2. Phonon modes and damping

Now let us present the numerical results based on our analytical findings. To this aim the following model parameters, appropriate for BNMO, are used: $T_N = 140$ K and $T_c = 485$ K for the bulk system, $J_b = 58$ K, $J_b' = 310$ K, $\Omega_b = 2$ K, $K_b = 50$ K, $F_b^f = F_b^m = 6\,\text{cm}^{-1}$, $R_b^m = -10\,\text{cm}^{-1}$, $R_b^f = -50\,\text{cm}^{-1}$, $A_b = -5\,\text{cm}^{-1}$, $B_b = 0.5\,\text{cm}^{-1}$, $\omega_0 = 610\,\text{cm}^{-1}$, $S = 1$ for the Ni-ions and $S = 3/2$ for the Mn-ions. The index b is related to the bulk material whereas s characterizes the surface. For simplicity we assume nearest neighbor exchange interaction and take $J_{ij}' = J'^{(s)}$,

$J_{ij} = J^{(s)}$, $R^{(s)}$ on the surface of the thin film and $J'_{ij} = J'^{(b)}$, $J_{ij} = J^{(b)}$, $R^{(b)}$ in the bulk. They can be enhanced or reduced compared to the bulk values. Because the anharmonic spin-phonon interaction parameters $R^{(f)}$ or $R^{(m)}$ are related to the second derivative of J'_{ij} or J_{ij} [111] it results also a change of the spin-phonon coupling on the surface. The exchange interaction constants are calculated from their relation to the critical temperatures. The magnetoelectric coupling constant K is obtained indirectly from the expression for the exchange coupling J_{ij} and J'_{ij} after calculation of the renormalized exchange interaction constants. The phonon-phonon interaction parameters follow from fitting the experimental data above the critical temperatures where the spin-phonon interactions vanish. The spin-phonon interaction constants are obtained from the experimental data at low temperatures, where the phonon-phonon interactions play only a minor role. In Fig. 4.4 the temperature dependence of the

Figure 4.4. – Temperature dependence of the phonon energy in BNMO thin films with $j^{(s)} = 52$ K, $J'^{(s)} = 290$ K, $R^{m(s)} = -8$cm^{-1}, $R^{F(s)} = -45$cm^{-1} for external magnetic field, $h = 0$ K (black), 10 K (red), 20 K (blue).

phonon energy of a BNMO thin film with $N = 7$ layers is shown. The phonon energy decreases with an increase of the temperature T. Such a softening is reported for BNMO thin films in [169] and BFCO thin films [170]. Below the magnetic transition T_N the system exhibits magnetic and ferroelectric properties. Fig. 4.4, black curve , illustrates clearly the coupling between the electric and magnetic properties below T_N, which is manifested as a kink at the magnetic phase transition temperature $T_N = 123$ K. This anomaly can be explained as an influence of vanishing magnetic ordering on the structural and the electric ordering in the system. Because of $T_N << T_C$, the magnetic system cannot influence the electric one above T_N, the two phases coexist only below T_N.

A similar small kink in the dielectric constant is observed in BNMO thin films in [160] indicating the interplay between ferromagnetic and ferroelectric interactions. The anomaly is attributed also to the strong anharmonic spin-phonon coupling characterized by the coupling $R^{(m)}$. In case $R^{(m)} = 0$ the kink disappears. Generally the kink can be considered as an evidence that the spin-lattice coupling is modified due

to the magnetoelectric effect. Obviously the magnetic exchange energy is enhanced when the magnetic ions shift their positions. This effect is particularly strong near to or below the magnetic phase transition and may result in structural anomalies and a change of the dielectric properties. A smaller kink is observed at the Curie temperature T_C due to anharmonic pseudospin-phonon interaction characterized by the coupling $R^{(f)}$. In the same manner one gets a softening of the phonon mode in BNMO near T_C. Above T_C the pseudospin-phonon interaction disappears and consequently only the anharmonic phonon-phonon interaction remains. In that case the phonon mode decreases very slowly and it is nearly temperature independent. The phonon damping Γ, related to the width of the Raman peaks, increases with
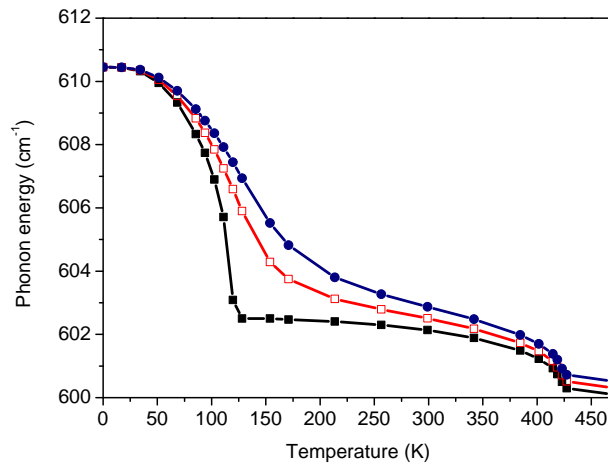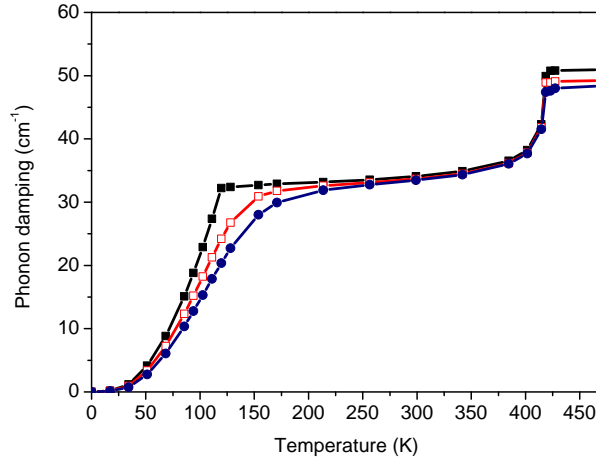

Figure 4.5. – Temperature dependence of the phonon damping in BNMO thin films with $J^{(s)} = 52$ K, $J'^{(s)} = 290$ K, $R^{m(s)} = -8\text{cm}^{-1}, R^{f(s)} = -45\text{cm}^{-1}$ for h= 0 K (black), 10 K (red), 20 K (blue).

increasing temperature. Around the magnetic transition temperature $T_N = 123$ K one observes again a kink in Γ, see Fig. 4.5 (black curve). The damping grows up in case the anharmonic spin-phonon interaction constant $R^{(m)}$ is enhanced.

A feature of the magnetoelectric effect is the ability to control the system by external electric and magnetic fields. In Figs. 4.4 and 4.5 we demonstrate that the phonon energy increases with an increasing magnetic field whereas the phonon damping decreases with h, see red and blue curves.

4.4.3. The thickness dependence of the phase transition temperatures

Both Figs. 4.4 and 4.5 suggest that the critical temperatures T_C and T_N for BNMO thin films are smaller compared to the bulk case. In Fig. 4.6 we present the thickness dependence of the phase transition temperatures based on our model. The critical temperature decreases with decreasing film thickness. For seven layers the temperature is fixed by $T_N = 123$ K. A similar decrease of T_C is also reported for BNMO
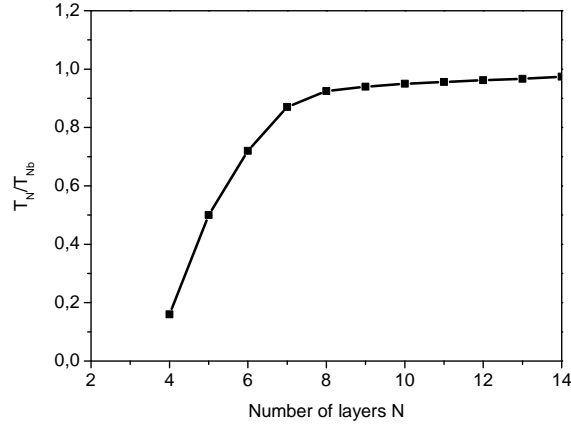
(a) T_N
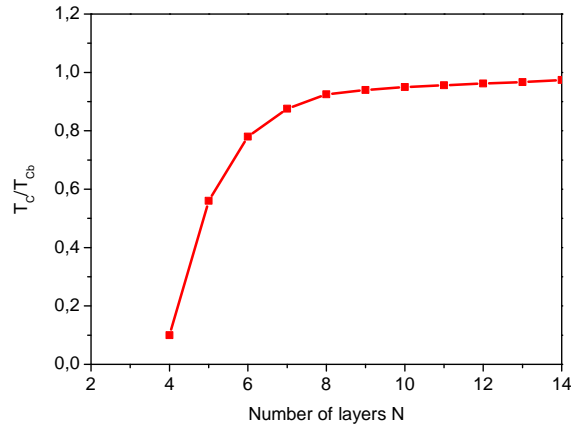
(b) T_C

Figure 4.6. – Thickness dependence of the phase transition temperatures (a) T_N (b) T_C in BNMO thin films.

thin films in [160] and for BNMO nanoparticles in [173] with $T_N = 122$ K.

To our understanding the model proposed is also applicable to other materials like $Bi_2M(1)M(2)O_6$ ($T_C >> T_N$), where the two magnetic ions M(1)M(2) could be Fe-Mn, Co-Mn, Fe-Cr. In case the Yttrium atoms in the compound Y_2MNO is subjected to a distortion similar to the Bi in BNMO we expect that our model is also useful for that material. As far as we know an experimental verification for Y_2MNO is still missing. So we would suggest to test the predictions of our model for Y_2MNO.

4.5. The origin of magnetism in ferroelectric ABO₃ nanoparticles

Ferroelectric oxides ABO_3 in which A is an alkali or rare-earth element, and B may represent different transition metals, such as $SrTiO_3$ (STO), $BaTiO_3$ (BTO), $PbTiO_3$ (PTO), $KTaO_3$ (KTO), $LiNbO_3$ (LNO) with a perovskite structure are widely used in the fields of non-linear optics, pyroelectric detectors, electro-optical modulators, thin film capacitors, and optical memories [16, 18]. Because their properties depend not only on its chemical composition but also on its structure, shape, and size, it has been found that reduction of the grain size to the nanoscale leads to distinct properties from those of the bulk [157].

Very recently, it has been shown from both experiments and theory that the ferroelectric materials ABO_3 (A = K, Li; B = Ta, Nb or A = Ba, Sr, Pb; B = Ti) become multiferroic when it is downsized to nanoscale [174–179]. These nanoparticles will be considered in the present section, and especially the origin of the magnetism using spin Hamiltonian models will be investigated. KTO single crystal is an archetypal incipient ferroelectric in which a long-range ferroelectric order does not establish at low temperatures owing to quantum fluctuations [16]. Skoromets et al. [180] reported a strong evidence of the ferroelectric phase transition near 60 K revealed by terahertz spectroscopy and microwave permittivity measurements of a polycrystalline KTO thin film on (0001) sapphire substrate. The optical properties of KTO nanocrystalline were investigated by Zhou et al. [181]. Photoluminescence studies exhibits that a broad blue light emission band peaking at about 490 nm was observed at room temperature. Oxygen vacancies should be responsible for this emission peak.

Anion vacancy driven magnetism in incipient ferroelectric STO and KTO nanoparticles is reported by Eliseev et al. [174]. Oxygen vacancies are observed in LTO [182] and LNO [183]. Very recently, it has been shown from both experiments and ab-initio calculations that the ferroelectric material STO becomes multiferroic when it is made at the nanoscale [174, 175, 184]. First principle prediction of vacancy-induced magnetism in non-magnetic perovskite $SrTiO_3$ is reported by Shein and Ivanovskii [185]. The role of the oxygen vacancies on the photoluminescence of nanocrystalline STO is investigated by Zhang et al. [186]. While ferroelectricity in proper ABO_3 ferroelectrics (which are often called classic ferroelectrics, such as BTO) is expected to diminish with the particle size reduction [187, 188], ferromagnetism cannot occur in its bulk form [52]. For example, bulk pure BTO, without defects or doping ions shows ferroelectric, but not magnetic properties. Based on their analytical results, Eliseev et al. [174] predicted that undoped nanoparticles of incipient ferroelectrics without any magnetic ions can become ferromagnetic even at room temperatures due to the inherent presence of a new type of magnetic defects with spin S = 1, namely oxygen vacancies, where the magnetic triplet state is the ground state in the vicinity of the surface (magnetic shell), while the non-magnetic singlet is the ground state in the bulk material (non-magnetic core). Cao et al. [189] have studied the vacancy induced magnetism in BTO (001) thin films based on density functional theory.

Recently, Shimada et al. [190] have investigated the possible origin of ferromagnetism in PTO containing vacancies by performing first-principles calculations. Previously,

the static and dynamic properties of KDP-type and BTO-type ferroelectric nanoparticles is reviewed [157]. Another interesting aspect is the recent observation that typical ferroelectric materials such as BTO and PTO become multiferroic when they are prepared at the nanoscale. However, apart from a density functional calculation for BTO, STO, and PTO [174, 189, 190] a well accepted theoretical description of the ferroic properties of nanocrystalline ABO₃ is of interest. We propose an alternative approach, a microscopic treatment using spin Hamiltonians.

It is suitable to predict measurable properties prior to experiments, and comparing with powerful many body calculations such as first principles density functional theory or Monte Carlo simulations. Our aim is explaining the origin of ferroelectric perovskite ABO₃ (A = K, Li; B = Ta, Nb or A = Ba, Sr, Pb; B = Ti) nanoparticles analytically. We put emphasis on the surface and bulk contributions to the polarization and magnetic saturation after considering O-octahedral vacancies surrounding the B sites in ABO₃ systems, which in the case of spins Hamiltonian are easily modeled by changing the local spin and pseudospins as a consequence of the new considered valences of the nonstoichiometric compounds.

4.5.1. Extended Heisenberg model for materials with different valence states

Due to the oxygen stoichiometry, i.e., the appearance of oxygen vacancies at the surface of the nanoparticles, we include into our model (a) resulting valences (of A or B site) and their corresponding stable spin states; (b) the mixture of different of such spin states, which are defined by the different orbital occupancies; (c) resulting interactions coupling the stabilized spins and therefore defining specific ordering and microscopic order parameters. Since the ferroelectricity in ABO₃ is originated from the off-centering of the Ti (or Ta) ions with respect to the cubic perovskite crystal we assume as the simplest model that there are two positions of the Ti (or Ta) atoms in a double-well potential. These two states are mapped on the B_z-component of a pseudospin operator in TIM.

The magnetic properties of ABO₃ nanoparticles are analyzed using the Heisenberg model for the resulting different valence states on the surface composed of the ions on the B site. Therefore, we have two magnetic subsystems which can interact. Then, terms must be included to describe the interaction between the equal spin ions and a third for the interaction between the different valence ions, with different spin values

$$
\begin{aligned}
H_m \;=\; & -\frac{1}{2}\sum_{i,j} J_1(i,j)\mathbf{S}_i^{Ti^{3+}}.\mathbf{S}_j^{Ti^{3+}} - \frac{1}{2}\sum_{i,j} J_2(i,j)\mathbf{S}_i^{Ti^{2+}}.\mathbf{S}_j^{Ti^{2+}} \\
& -\frac{1}{2}\sum_{i,j} J_3(i,j)\mathbf{S}_i^{Ti^{3+}}.\mathbf{S}_j^{Ti^{2+}} - \sum_i D_i(S_i^z)^2,
\end{aligned}
\tag{4.42}
$$

J_{ij} is the exchange integral between the nearest neighbors of the ions at the site B, for instance the Ti³⁺ and/or Ti²⁺ (Ta⁴⁺ and/or Ta³⁺) ions, D ($D < 0$) is the single-site anisotropy parameter, $\mid D \mid < J$.

In principle, the coexistence of spontaneous electric polarization and a finite saturation magnetization could give rise to a multiferroic behavior such in the ferroelectric

ABO$_3$ nanoparticles. The full Hamiltonian must include a magnetoelectric coupling term in analogy to other multiferroic systems.

4.5.2. Size effects on magnetization and polarization in spherical ferroelectric nanoparticles

Using the Green's function technique we have calculated the size dependence of the polarization P in KTO nanoparticles based on Eq. (4.39). E_n^f are the transverse pseudospin excitations of the n-th shell which are given in Eq. (4.35). The average magnetization for arbitrary magnitude of S is given by Eq. (3.35).

Now we will present our numerical results. First we consider the polarization P in spherical KTO nanoparticles. Due to the changed number of next neighbors on the surface and the reduced symmetry, the exchange interaction constant for the ABO$_3$ nanoparticles can take different values on the surface compared to the bulk. We assume $J'_s < J'_b$ for the exchange interaction constant [156]. It can be seen (Fig. 4.7, black curve) that P decreases with a decreasing particle size N and vanishes at a critical value $N_c = 3$.

Figure 4.7. – Size dependence of the polarization P (black) and magnetization M (red) of a KTO nanoparticle for $T = 50$ K and different exchange interactions: (black) $J'_s = 0.5 J'_b$, $\Omega_s = \Omega_b$, (red) $J_s = 2J_b$, $D_s = D_b$.

The distance between the shells is approximated by the lattice parameter a in KTO ($a = 3.94 \ \mathring{A}$) according to Hao et al. [191] the critical size is $N_c \approx 12$ nm. This is in qualitative agreement with many experimental data for ferroelectric ABO$_3$ nanoparticles [157]. In principle various critical sizes of phase transitions in the range from 4.5-25 nm [157] have been reported. The inconsistency of N_c can be ascribed to the difficulty in measurements, moreover to factors such as defects, impurities and more. N_c depends also on the shape of the nanoparticle.

We will consider the differences in the properties of bulk and nanosized ferroelectric ABO$_3$ materials, the origin of ferroelectricity and ferromagnetism, for example

in KTO. In usual perovskite-based ferroelectrics, the ferroelectric distortion occurs due to the displacement of B-site cation (Ta^{5+}) with respect to the oxygen octahedral cage. Here the transition metal ion (Ta^{5+} in KTO) requires an empty d shell since the ferroelectric displacement occurs due to the hopping of electrons between Ta d and O p atoms. This normally excludes any net magnetic moment because magnetism requires partially filled d shells of a transition metal. Practically, all ferroelectric perovskites contain transition metal ions with an empty d shell, such as Ti^{4+}, Ta^{5+}, W^{6+}. Ferroelectricity in these systems is caused by the off-center shifts of the transition metal ion, which forms strong covalent bonds with one (or three) oxygens, using their empty d states. The presence of real d electrons in d^n configurations of magnetic transition metals suppresses this process, preventing ferroelectricity in magnetic perovskites. This so-called 'd^0 versus d^n problem' was one of the first to be studied theoretically at the beginning of the recent revival of multiferroics [52, 192]. Each oxygen vacancy on the surface is expected to donate two electrons to the empty d state of a single Ta^{5+}($3d^0$) ion to produce a Ta^{3+}($5d^2$) ion with $S = 1$ or one electron each to two Ta^{4+} ions, probably situated on either side of the oxygen vacancy, to make them Ta^{4+}($5d^1$) ions with $S = 1/2$.

In order to obtain the magnetic properties in KTO nanopartilces and in accordance with the experimental data, we have assumed that the oxygen vacancies which appear in the surface shell, lead to the appearance of Ta^{3+} ($S = 1$). In the other shells there are the non-magnetic Ta^{5+} ions, i.e. we also assume that ferromagnetism is arising from the oxygen vacancies at the surface and ferroelectricity from the core. Nanoparticles have a much greater surface to volume ratio than bulk materials. The increased surface to volume ratio with decreasing nanoparticle size means surface atoms have a much greater effect on chemical and physical properties of a nanoparticle. With decreasing the particle size the number of the oxygen vacancies at the surface increases and therefore the Ta^{3+} ions in the surface shell increase, too, whereas the number of the non-magnetic core shells with the non-magnetic Ta^{5+} ions decreases. We have calculated the magnetization M of KTO nanoparticles. The results for a surface exchange interaction constant which are greater than the bulk value, ($J_s > J_b$) are shown in Fig. 4.7, red curve. The anisotropies play an important role in nanostructures which are considered in [148].

We assume that the value of the surface anisotropy D_s is equal to that in the bulk D_b. For a quantitative agreement with the experimental data, $D_s \neq D_b$ must be taken into account. We obtain that with decreasing particle size, below a critical size $N_c = 7$ a small ferromagnetism appears, which increases with decreasing particle size, whereas the polarization decreases (black curve), i.e. in an intermediate size interval KTO nanoparticles demonstrate multiferroic properties - coexistence of ferroelectricity and ferromagnetism. The appearance of the ferromagnetism, of a stable ferromagnetic ground state requires a minimum of oxygen vacancies or a minimum of Ta ions with $S \neq 0$. This leads to this critical size $N_c = 7$. In analogy to the critical size $N_c = 3$ where the polarization vanishes and depends on the substance we assume that the critical size is also different for the different materials and depends on the model parameters. It seems that the Ta^{4+}-ions in LTO are stable only at temperature T near or smaller than 77 K. Therefore, the contribution of the Ta^{3+} to the appearance of the magnetism in LTO and KTO is probably more important than that of Ta^{4+}.
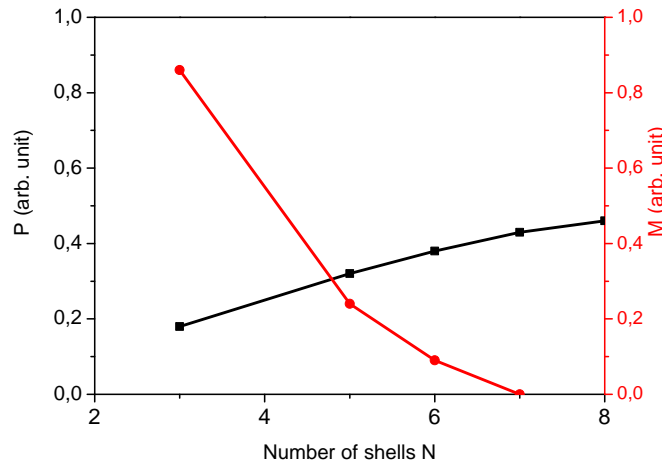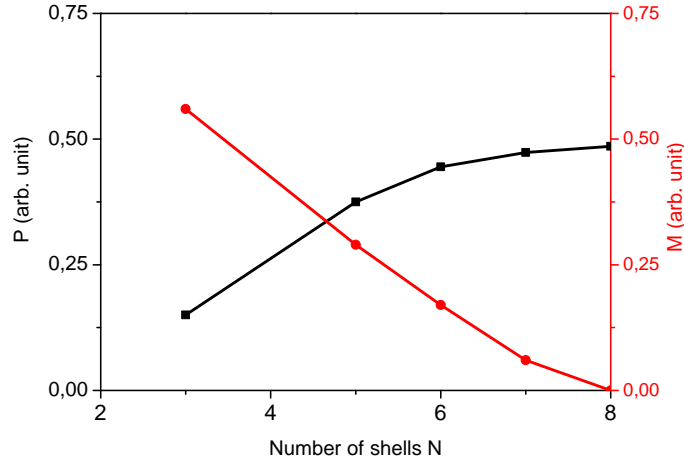
Figure 4.8. – Size dependence of the polarization P (black) and magnetization M (red) of a STO nanoparticle for $T = 95$ K and different exchange interactions: (black) $J'_s = 0.5J'_b$, $\Omega_s = \Omega_b$, (red) $J_s = 2J_b$, $D_s = D_b$.

We conclude that the observed ferromagnetism is intrinsic to the nanoparticles and is not due to any magnetic impurity phase or any other artefact.

Recently, Diaz-Moreno et al. [193] have observed the multiferroic response of nanocrystalline lithium niobate $LiNbO_3$ (LNO) also due to oxygen vacancies. They have measured ferroelectric and ferromagnetic hysteresis loops. Nb^{5+} is a non-magnetic ion. Based on our microscopic approach in this case such vacancies lead to the appearance of different valence states composed of Nb^{4+} and/or Nb^{3+} which are paramagnetic (electron configuration $4d^1$, electron spin S = 1/2). They cause a nonzero magnetization in an external magnetic field which decreases with increasing particle size.

Further, we have considered STO nanoparticles and have calculated the size dependence of the polarization P for $J_s < J_b$ [148]. It is observed that P decreases with decreasing particle size N to vanish at a critical value $N_c = 3$ (Fig. 4.8, black curve). This is in agreement with many experimental data [148, 188, 194]. We will now consider the origin of magnetism in STO nanoparticles. The oxygen vacancies at the surface cause the formation of $Ti^{3+}(d^1)$ or $Ti^{2+}(d^2)$ ions with nonzero net spin ($S = 1/2$ and $S = 1$, respectively [195, 196]). We assume that with decreasing particle size where the number of oxygen vacancies at the surface increases, the number of Ti^{2+} and T^{3+} ions on the surface is also increased leading to small ferromagnetism. The presence of the mixed valence state of the Ti-ions due to point defects could also be the origin of the observed room temperature ferromagnetism in TiO_2 nanoparticles [177].

The results for the magnetization in STO nanoparticles taking into account the interactions between the Ti^{2+} ions on the surface with $J_s > J_b$ are shown in Fig. 4.8, red curve. The magnetization decreases with increasing the particle size and vanishes at a critical size. The critical size should be enhanced by increasing external magnetic

field. Comparing the two curves, for the polarization and the magnetization, we can conclude that with increasing particle size P increases and for bulk STO there exists only the ferroelectricity. But with decreasing particle size, below a critical size $N_c = 8$, a weak ferromagnetism appears. The smaller the particle size is the higher is the saturation magnetization. The effect that larger particles lead to a lower magnetization is consistent with the suggestion that surface defects decrease with increasing particle size. Again we obtain that ferroelectricity and ferromagnetism coexist in an intermediate size interval in STO nanoparticles. This is in agreement with the obtained multiferroic properties in STO nanoparticles [174, 184]. The origin of the observed multiferroism in BTO and PTO nanoparticles [176–179, 195] is of the same nature as discussed above for STO nanoparticles.

The magnetic properties of BTO are analyzed for the resulting different valence states on the surface composed of Ti^{3+} or Ti^{2+}. Different to many oxides the exchange coupling is positive as it was explained previously by [176, 195]. Contrary to the ferroelectric case, the surface exchange interaction J_s is assumed to be larger as the related bulk coupling J_b. The result for M depending on the NP size N is depicted as red curve in Fig. 4.10 in case of Ti^{3+} on the surface with $S = 1/2$. The temperature is

Figure 4.9. – Size dependence of the polarization P (black) and magnetization M (red) of a BTO-NP for $T = 300$K, $J_b' = 700$K, $\Omega_b = \Omega_s = 10$K, $J_b = 344$K, $S = 1$ (Ti^{2+}), and different exchange interactions: (black) $J_s' = 0.5J_b'$, (red) $J_s = 2J_b$.

assumed to be T = 300 K. The magnetization increases with decreasing particle size above a critical size N_c, which is in qualitative agreement with the experimental data presented in [176]. The critical size depends on the model parameters. Comparing the two curves for the polarization (black curve) and the magnetization (red curve) we argue that ferroelectricity exists also for bulk material whereas the magnetization disappears. However, with decreasing size a weak ferromagnetic behavior is observed below a critical size of $N_c \simeq 8$. The magnetization increases with decreasing particle size, while the polarization decreases. In an intermediate size interval the BTO-NP offer multiferroic properties characterized by the coexistence of a finite polarization and magnetization. Fig. 4.9 shows the magnetization for $S = 1$, i.e. originated

from magnetic Ti^{2+} ions on the surface. The result is quite similar to Fig. 4.10, indicating that the mechanism for the appearance is the same as for Ti^{3+} ions. The ferromagnetism is stronger compared to the case of Ti^{2+}. Because in that case the shells are smaller the magnetization disappears for a lower critical size N_c and as a consequence the polarization becomes higher. For a further clarification of the situation we suggest to study experimentally the influence of an external electrical field on the magnetic properties or vice versa the influence of a magnetic field on the electric properties which is one of the important features of multiferroics compounds. Such a measurement should give more evidence of the magnetoelectric coupling in BTO or PTO nanoparticles. The result for the polarization is shown as black curve in Fig. 4.10.
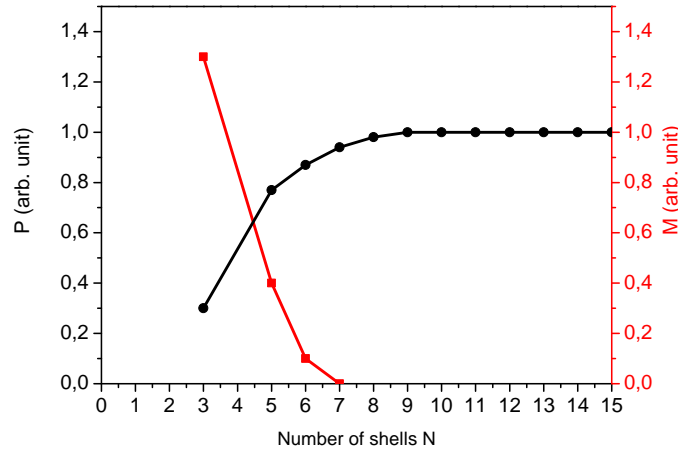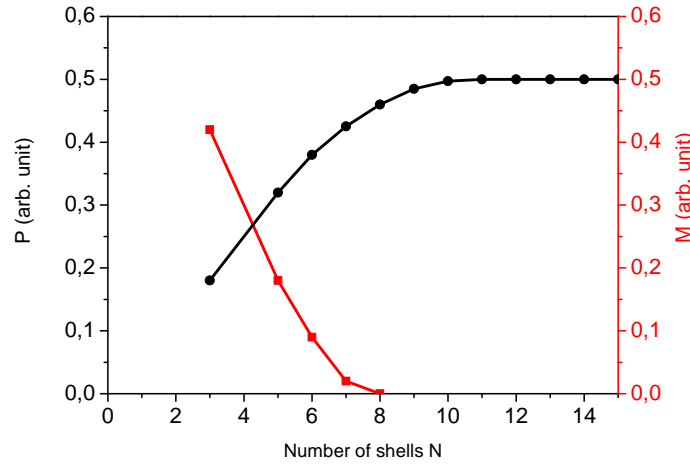

Figure 4.10. – Size dependence of the polarization P (black) and magnetization M (red) of a BTO-NP for $T = 300\,\text{K}$, $J_b = 700\,\text{K}$, $\Omega_b = \Omega_s = 10\,\text{K}$, $J_b = 250\,\text{K}$, $S = 1/2$ (Ti^{3+}), and different exchange interactions: (black) $J'_s = 0.5 J'_b$, (red) $J_s = 2 J_b$.

The polarization is enhanced with increasing shell number N and becomes saturated for large NP-size. The observation is in agreement with experimental data presented in [157, 187, 188]. Mangalam et al. [195] have carried out magnetic measurements of BTO samples with 60 nm, 100 nm and 2 μm. While the sample on the nanometer scale reveals clearly ferromagnetism at room temperature the sample of μm scale shows a diamagnetic behavior as it is also expected for the bulk BTO material. The smaller the particle size is the higher is the saturation magnetization. The effect that larger particles lead to a lower magnetization is consistent with the suggestion that surface defects decrease with increasing particle size. As argued in [195] the observed ferromagnetism in such BTO-NP can be correlated with the presence of oxygen vacancies at the surface of the NP. So positron annihilation studies in BTO-NP reveal a lower annihilation rate of positrons with the 2p electrons of oxygen in the sample of 100 nm and 60 nm in comparison to the bulk system. This observation indicates the presence of oxygen vacancies [195]. Each oxygen vacancy is expected to donate two electrons to the empty d-state of a single $Ti^{4+}(d^0)$ ion in order to produce a Ti^{2+} (d^2) ion with spin $S = 1$.
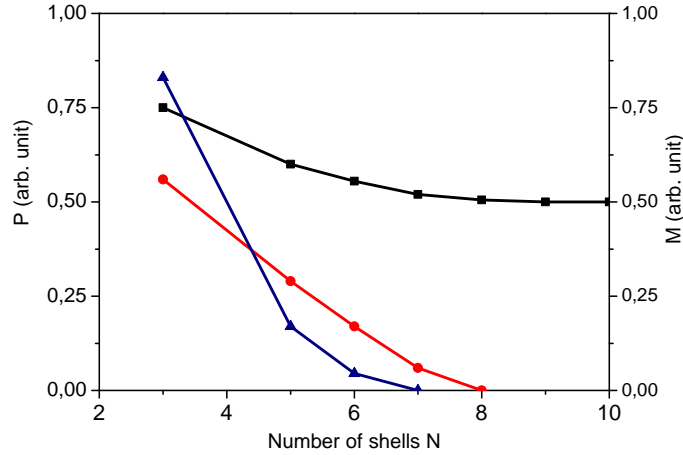
Figure 4.11. – Size dependence of the polarization P (black) and magnetization M (red, blue) of a ferroelectric ABO nanoparticle for $T = 95$ K and different exchange interactions: (black) $J'_s = 2J'_b$, $\Omega_s = \Omega_b$, (red) $J_s = 2J_b$, $D_s = D_b$, (blue) $J_s = 4J_b$, $D_s = D_b$.

An alternative mechanism is that each oxygen electron goes to different Ti^{4+} ions and generate two Ti^{3+} ions in state d^1 with spin $S = 1/2$ [195, 196]. With decreasing particle size the number of oxygen vacancies increases and hence the number of Ti^{2+} or Ti^{3+} ions is also enlarged. This enhancement of Ti ions with nonzero spin give rise to a weak ferromagnetism. Probably there is also the creation of a mixed valence state composed of an superposition of both states d^2 and d^1. The presence of the mixed valence state of the Ti-ions due to point defects could be also the origin for the observed room temperature ferromagnetism in TiO$_2$ NP suggested in [177, 197].

Finally, we have proved the stability of the ferromagnetic and antiferromagnetic states in the presence of oxygen vacancies in the STO nanoparticle. We have calculated the magnetic energy from Eq. (4.31) for ferromagnetic and antiferromagnetic exchange interaction constants J and have found that the ferromagnetic state is lower in energy both in the bulk and at surface. A similar result is reported and discussed by Mangalam et al. [195].

In some ferroelectric nanostructures, such as KNO$_3$ thin films [198, 199] or triglycine-sulphate (TGS) films [200, 201], it is observed that the Curie temperature and the polarization increases with decreasing thickness. In this case we use $J_s > J_b$ [148, 202] and obtain the results shown in Fig. 4.11. The polarization and the magnetization decrease with increasing particle size. Below N_c the nanoparticle is multiferroic. Above a critical N_c the magnetization vanishes and the nanoparticle remains only ferroelectric. Experimental data does not exist for these materials.

Theoretical investigations based on density functional theory [174, 175, 189, 190] have discussed mainly the density and energies of states of BTO, STO, and PTO nanostructures. The magnetization hysteresis M(H) is obtained by Zhang et al. [175] and Mangalam et al. [195] whereas the polarization hysteresis loop P(E) and the

temperature dependence of the dielectric constant $\epsilon(T)$ are reported in [194]. Some of the authors [174, 175, 189, 190] have reported that not only O vacancy but also Ti vacancy induces ferromagnetism but by different mechanisms [174, 175, 189, 190]. Using first-principles simulations, a strong coupling between a surface polar phonon and spin in nanocrystalline $BaTiO_3$ is shown, result in a magnetocapacitance effect observed at room temperature, which can open up possibilities of new electromagneto-mechanical devices at the nanoscale [195].

5. Conclusions and perspectives

5.1. Conclusions

The thesis is focused on a theoretical investigation of materials possessing two or more kinds of ferroic orders in a single phase. Such multiferroic systems are under permanent debate both experimentally and theoretically. In particular, we analyzed systems in which ferromagnetic or antiferromagnetic phases coexist with a ferroelectric phase. In an analytical approach, the system consists of two subsystems which are interconnected by symmetry allowed coupling terms. The main classes of models representing the related subsystems are different realizations of the Heisenberg model and the Ising model in a transverse field. Furthermore, additional phonon degrees of freedom are included. In this thesis we have proposed microscopic models in order to explain the origins of the ME effect in the different multiferroic compounds. To this aim, two strategies were investigated; the ME coupling is taken to be either biquadratic or linear in P and quadratic in M. The biquadratic coupling between the pseudospins and magnetic moments implies that the magnetic and ferroelectric ordering have independent mechanism. In particular, this generally leads to different transition temperatures for the two subsystems. The model can be applied to multiferroic substances where $T_C >> T_N$, for example, hexagonal $RMnO_3$ and BNMO. For the other multiferroic compounds, like $MnWO_4$ or RMn_2O_5 where ferroelectricity exists only in a magnetically ordered state and T_C is lower but close to T_N, the multiferroic nature arises from the magnetically induced ferroelectricity. Thus, in these materials ferroelectric polarization is induced by striction through exchange interaction between different magnetic ions. Considering the appropriate coupling, the analytical calculations were done in the framework of double-time Green's function technique for different multiferroics. Let us summarize the main results obtained in this work.

- In section 3.3 the investigation was concentrated on type-II multiferroics observed in rare-earth components. Such systems exhibit a linear magnetoelectric coupling and both ferroic phases offers well separated phase transition temperatures. The aim was to study the influence of the MEC on the multiferroic behavior. The presented quantum model is based on the Heisenberg spin model with competing ferromagnetic and antiferromagnetic order. The interplay between these two couplings mechanisms leads to a collinear magnetic structure which is frustrated. The ferroelectric subsystem is characterized by the Ising model in a transverse field. The magnetoelectric coupling is quadratic in the magnetization and linear in the polarization. For $T_C < T < T_N$ the system offers conventional Goldstone modes, i.e., gapless spin-wave excitations. The MEC breaks the continuous symmetry of the Heisenberg model and hence the

dispersion relation is altered and shows a gap for zero wave vector. The effect is the stronger the higher the MEC is. The appearance of ferroelectricity at T_C is induced by the MEC, where the ferroelectric phase is manifested by a kink in the dispersion relation. Likewise the magnetization is changed in the vicinity of T_C. The effect can be observed for different strengths of the MEC. Finally, the multiferroic system is subjected to external electric and magnetic fields. We find that the polarization increases with growing magnetic field, i.e., the ferroelectric subsystem can be influenced by a magnetic field. In the same manner the magnetization alters due to an external electric field. Our results suggest that for sufficient high electric fields the phase transition temperature T_C is shifted to higher values. This effect should be observed in experiments.

- A further goal was to identify the role of phonons in magnetoelectric effects in RMn_2O_5. Here, the ferroelectric subsystem is characterized by both displacive-like couplings manifested by lattice distortions and order-disorder-like elements expressed in terms of pseudospins. As a consequence of the detailed characterization of both subsystems, the coupling between the ferroic phases is not only given by a direct magnetoelectric coupling but additionally by spin-phonon couplings. To be specific, we have introduced two kinds of spin-phonon couplings, the magnetic dominated as well as the ferroelectric dominated ones. We focused on the influence of the various couplings on the phonon spectrum of the multiferroic system. Due to the magnetoelectric coupling the harmonic phonon mode is renormalized and becomes temperature-dependent. Both phase transitions are manifested by a kink in the phonon spectrum at the corresponding transition temperatures.

  The behavior of the modified phonon mode is strongly influenced by the spin-phonon coupling. For positive couplings the mode becomes harder whereas for negative coupling the mode becomes softer. In the latter case we showed that the phonon spectrum is very sensitive to a change of the magnetic spin-phonon coupling, while for different couplings the kink in the dispersion relation is maintained. In the same manner, the ferroelectric pseudospin-phonon coupling, relevant for $T < T_C$, alters the phonon spectrum. The phonon mode is affected by an external magnetic field, i.e. the phonon frequency can be triggered by a magnetic field. We also found that the magnetization is influenced by the spin-phonon coupling in such a manner that an increase of the coupling leads to a decrease of the magnetization.

- Materials like RMn_2O_5 offers a very complicated magnetic zigzag structure which had been up to now resisted to an analytical description based on a reasonable Hamiltonian. In this thesis (section 3.5) the conventional Heisenberg-model is significantly extended to incorporate the complex magnetic structure at least approximately. Such an approach is to the best of our knowledge a first attempt in this field and should be developed further. The main mechanism for the appearance of a nonzero polarization P in those materials has been attributed to exchange-striction among frustrated Mn spin networks [81]. Building upon experimental facts and the space group symmetry, we have generalized

the Heisenberg-model to study the properties of such asymmetric antiferromagnetic zigzag spin chains of two different Mn^{4+} and Mn^{3+} magnetic ions. The ferroelectric subsystem was considered by defining polarization operators. The polar system is given by a Hamiltonian which does not reveal a separate phase transition (improper ferroelectricity). Instead of that the ferroelectric phase is triggered exclusively by the coupling to the magnetic part. In particular, the polarization is given by spin-spin correlation functions.

- As experimentally observed, the multiferroic properties of various components can be changed by chemical substitutions. Therefore, we have investigated the doping effects of non-magnetic and magnetic substitution at the Mn site on the phase transition temperatures of $MnWO_4$. We conclude that depending on the ionic radius of the doping ions, i.e., on the exchange interaction constants in the defect sites, the magnetic phase transition temperature can be smaller (for non-magnetic Zn or Mg ions) or larger (for transition metal Fe or Co ions) compared to the case without defects. The differences in the Fe- and Co-doping concentration dependence of T_1, the temperature in which the phase transition to a frustrated commensurate AF1 phase occurs, is due to the different sign of the single-ion anisotropy.

- Multiferroic thin films and nanostructures also attract lots of attention since their properties differ from bulk materials. In this thesis (section 4.4) the physical properties of double-perovskite BNMO thin film multiferroic were studied based on a microscopic model. In particular, the phonon frequency and its damping were analyzed. The phonon spectrum reveals a kink at the magnetic phase transition temperature indicating a strong evidence for a magnetoelectric coupling. Furthermore, the phonon mode is controlled by an external magnetic field. To our understanding, the model proposed is also applicable to other materials like $Bi_2M(1)M(2)O_6$ ($T_c >> T_N$), where the two magnetic ions M(1)M(2) can be Fe-Mn, Co-Mn, Fe-Cr. We expect the efficiency of our model, in case the Yttrium atoms in the compound Y_2MNO are subjected to a distortion similar to the Bi in BMNO. As far as we know, an experimental verification for Y_2MNO is still missing. Therefore we would suggest to test the predictions of our model for Y_2MNO.

- Another related problem in the field of multiferroics is the oxygen vacancy induced ferromagnetism in ferroelectric perovskite ABO_3. Using an analytical approach we find the size dependence of the polarization and magnetization. We have shown that ferromagnetic properties which lead to multiferroic properties in KTO and LTO nanoparticles could be due to the oxygen vacancies at the surface and to the appearance of mixed valence state of Ta^{4+} and/or Ta^{3+} ions on the surface with nonzero net spin. This leads to a week ferromagentism which is an intrinsic effect to the nanoparticles and does not arise from any magnetic impurity phases or any other artefact.

  The polarization decreases with decreasing particle size, whereas the magnetization increases below a critical particle size. We obtained that in an intermediate size interval the ferroelectric nanoparticles are multiferroic where the

bulk material is only ferroelectric. A similar discussion explains the origin of ferromagnetism in BTO, STO and LNO nanoparticles. These results suggest the possibility of implementing magnetoelectric coupling in conventional ferroelectric materials.

It will be of interest to observe experimentally the influence of an external electrical field on the magnetic properties or the influence of a magnetic field on the electric properties which is one of the important characteristics of multiferroic compounds. This would be the evidence of the magnetoelectric coupling and will contribute to the clarification of its mechanism in perovskite ABO_3 nanoparticles. Let us remark that our approach can be also used to analyze ferroelectric ABO_3 nanoparticles doped with transition metal ions like Fe, Mn, Co or Ni. There are recent experimental studies in order to obtain multiferroic properties in these substances, for example see [202, 203].

5.2. Perspectives

As a future aspect, one can investigate the complete phase diagram of the multiferroic materials to picture a more realistic theoretical understanding of their behavior. For instance, in the RMn_2O_5 series of multiferroics, the significance of the exchangestriction model in the commensurate phase has been made clear. Nevertheless, the exact mechanism behind the low temperature magnetoelectric phenomena remains a subject of debate. Besides, the appearance of Dzyaloshinskii-Moriya interaction at low temperature as well as the magnetic ordering of the R^{3+} moments which occurs below 10 K should be considered in this temperature interval.

Furthermore, we consider a uniform domain in our calculations. However, formation of domains is the feature of any ferroic order. Domain walls may play an important role towards the application of multiferroics to practical devices according to their small size as well as the fact that their location can be controlled [204]. The net magnetic moments at ferroelectric domain walls may potentially be manipulated by applied electric fields, indicating a magnetoelectric coupling at domain walls in single-phase multiferroics [205]. This aspect which stimulate new correlation phenomena can be considered as well. Additionally, exploring analytically the mechanism of the functional charge transport properties in multiferroics, as well as the use of semiconducting multiferroic oxides for thermoelectric generation , will arouse considerable interest and development.

A. Appendix

● Following the Eq. (3.66), we expand H_{ph} in terns of ladder operators, a and $a^\dagger$

$$H_{ph} = \sum_k w_k(a_k^\dagger a_k + 1) + \frac{1}{3!}\sum_{kk_1} B(k,k_1)(2\omega_k)^{-\frac{1}{2}}(2\omega_{-k_1})^{-\frac{1}{2}}(2\omega_{k_1-k})^{-\frac{1}{2}}\left[a_k a_{-k_1} a_{k_1-k}\right.$$

$$+a_k a_{-k_1} a_{k-k_1}^\dagger + a_k a_{k_1}^\dagger a_{k_1-k} + a_k a_{k_1}^\dagger a_{k-k_1}^\dagger a_{-k}^\dagger + a_{-k_1} a_{k_1-k} + a_{-k}^\dagger a_{-k_1} a_{k-k_1}^\dagger$$

$$+a_{-k}^\dagger a_{k_1}^\dagger a_{k_1-k} + a_{-k}^\dagger a_{k_1}^\dagger a_{k-k_1}^\dagger\left.\right] + \frac{1}{4!}\sum_{kk_1k_2} A(k,k_1,k_2)(2\omega_{k_1})^{-\frac{1}{2}}(2\omega_{k_2})^{-\frac{1}{2}}\times$$

$$\times(2\omega_{-k-k_2})^{-\frac{1}{2}}(2\omega_{-k_1+k})^{-\frac{1}{2}}\left(a_{k_1}a_{k_2}a_{-k-k_2}a_{-k_1+k} + a_{k_1}a_{k_2}a_{-k-k_2}a_{k_1-k}^\dagger\right.$$

$$+a_{k_1}a_{k_2}a_{k+k_2}^\dagger a_{k-k_1} + a_{k_1}a_{k_2}a_{k+k_2}^\dagger a_{-k+k_1}^\dagger + a_{k_1}a_{-k_2}^\dagger a_{-k-k_2}a_{-k_1+k}$$

$$+a_{k_1}a_{-k_2}^\dagger a_{k+k_2}^\dagger a_{-k_1+k} + a_{k_1}a_{-k_2}^\dagger a_{-k-k_2}a_{k_1-k}^\dagger + a_{k_1}a_{-k_2}^\dagger a_{k+k_2}^\dagger a_{k_1-k}^\dagger$$

$$+a_{-k_1}^\dagger a_{k_2}a_{-k-k_2}a_{-k_1+k} + a_{-k_1}^\dagger a_{k_2}a_{-k-k_2}a_{k_1-k}^\dagger + a_{-k_1}^\dagger a_{k_2}a_{k+k_2}^\dagger a_{-k_1+k}$$

$$+a_{-k_1}^\dagger a_{k_2}a_{k+k_2}^\dagger a_{k_1-k}^\dagger + a_{-k_1}^\dagger a_{-k_2}^\dagger a_{-k-k_2}a_{-k_1+k} + a_{-k_1}^\dagger a_{-k_2}^\dagger a_{-k-k_2}a_{k_1-k}^\dagger$$

$$+a_{-k_1}^\dagger a_{-k_2}^\dagger a_{k+k_2}^\dagger a_{-k_1+k} + a_{-k_1}^\dagger a_{-k_2}^\dagger a_{k+k_2}^\dagger a_{k_1-k}^\dagger\left.\right).$$

$$\text{(A.1)}$$

Using the appropriate commutation relations

$$[a_q, a_{q'}^\dagger] = \delta_{q,q'} \quad ; \quad [a_q, a_{q'}] \equiv [a_q^\dagger, a_{q'}^\dagger] = 0, \tag{A.2}$$

we have

$$[a_q, H_{ph}] = \omega_q a_q + \frac{1}{2}\sum_k B(k,q)(2\omega_q)^{-\frac{1}{2}}(2\omega_k)^{-\frac{1}{2}}(2\omega_{q-k})^{-\frac{1}{2}}\left[(a_k + a_{-k}^\dagger)\times\right.$$

$$\times(a_{q-k} + a_{k-q}^\dagger)\left.\right] + \frac{1}{4!}\sum_{kk_1} A(k,k_1,q)(2\omega_{k_1})^{-\frac{1}{2}}(2\omega_q)^{-\frac{1}{2}}(2\omega_{q-k})^{-\frac{1}{2}}\times$$

$$\times(2\omega_{-k_1+k})^{-\frac{1}{2}}\left(\left[\{a_{q-k},a_{k_1}\} + \{a_{q-k},a_{-k_1}^\dagger\} + \{a_{k-q}^\dagger,a_{k_1}\}\right.\right.$$

$$+ \{a_{k-q}^\dagger,a_{-k_1}^\dagger\}\left]\right.(a_{k-k_1} + a_{k_1-k}^\dagger) + (a_{k_1} + a_{-k_1}^\dagger)\left[\{a_{q-k},a_{k-k_1}\}\right.$$

$$+ \{a_{q-k},a_{k_1-k}^\dagger\} + \{a_{k-q}^\dagger,a_{k-k_1}\} + \{a_{k-q}^\dagger,a_{k_1-k}^\dagger\}\left]\left.\right)\right..$$

$$\text{(A.3)}$$

$$[a_q^\dagger, H_{ph}] = -\omega_q a_q^\dagger - \frac{1}{2}\sum_k B(k,q)(2\omega_q)^{-\frac{1}{2}}(2\omega_k)^{-\frac{1}{2}}(2\omega_{q+k})^{-\frac{1}{2}}\big[(a_k + a_{-k}^\dagger)\times$$

$$\times(a_{-q-k} + a_{k+q}^\dagger)\big] - \frac{1}{4!}\sum_{kk_1} A(k,k_1,q)(2\omega_{k_1})^{-\frac{1}{2}}(2\omega_q)^{-\frac{1}{2}}(2\omega_{q-k})^{-\frac{1}{2}}\times$$

$$\times(2\omega_{k_1+k})^{-\frac{1}{2}}\bigg((a_{k_1}+a_{-k_1}^\dagger)\big[\{a_{-k-k_1},a_{k-q}\} + \{a_{-k-k_1}, a_{q-k}^\dagger\}$$

$$+\{a_{k+k_1}^\dagger, a_{k-q}\} + \{a_{k+k_1}^\dagger, a_{q-k}^\dagger\}\big] + \big[\{a_{k_1}, a_{k-q}\} + \{a_{k_1}, a_{q-k}^\dagger\}$$

$$+\{a_{k-q}, a_{-k_1}^\dagger\} + \{a_{k+k_1}^\dagger, a_{q-k}^\dagger\}\big](a_{-k-k_1} + a_{k+k_1}^\dagger)\bigg). \tag{A.4}$$

$$[a_q, H_{mph}] = -F_M(q)(2\omega_q^0)^{-1/2}s_q^z - \frac{1}{2}\sum_k R_M(q,k)(2\omega_q^0)^{-1/2}(2\omega_k^0)^{-1/2}\big[(a_k + a_{-k}^\dagger)s_{q-k}^z$$

$$+(a_{-k} + a_k^\dagger)s_{k+q}^z\big],$$

$$[a_q^\dagger, H_{mph}] = F_M(q)(2\omega_q)^{-1/2}s_{-q}^z + \frac{1}{2}\sum_k R_M(q,k)(2\omega_q^0)^{-1/2}(2\omega_k^0)^{-1/2}\big[(a_{-k} + a_k^\dagger)s_{k-q}^z$$

$$+(a_k + a_{-k}^\dagger)s_{-k-q}^z\big],$$

$$[a_q, H_{fph}] = -F_F(q)(2\omega_q^0)^{-1/2}\big[(\frac{1}{2} - \rho_q)\cos\nu - \frac{1}{2}(b_{-q}^\dagger + b_q)\sin\nu\big]$$

$$-\frac{1}{2}R_F(q)(2\omega_q)^{-1}(a_q + a_{-q}^\dagger)\cos\nu + \frac{1}{2}\sum_k R_F(q,k)(2\omega_k)^{-1/2}(2\omega_q)^{-1/2}\times$$

$$\times\big((a_k + a_{-k}^\dagger)\frac{1}{2}(b_{q-k}^\dagger + b_{k-q})\sin\nu) + (a_{-k} + a_k^\dagger)(\rho_{-k-q}\cos\nu$$

$$+\frac{1}{2}(b_{q+k}^\dagger + b_{-k-q})\sin\nu)\big),$$

$$[a_q^\dagger, H_{fph}] = F_F(q)(2\omega_q^0)^{-1/2}\big[(\frac{1}{2} - \rho_{-q})\cos\nu - \frac{1}{2}(b_q^\dagger + b_{-q})\sin\nu\big]$$

$$+\frac{1}{2}R_F(q)(2\omega_q)^{-1}(a_{-q} + a_q^\dagger)\cos\nu + \frac{1}{2}\sum_k R_F(q,k)(2\omega_k)^{-1/2}(2\omega_q)^{-1/2}\times$$

$$\times\big((a_{-k} + a_k^\dagger)(\rho_{q-k}\cos\nu + \frac{1}{2}(b_{-q+k}^\dagger + b_{-k+q})\sin\nu) + (a_k + a_{-k}^\dagger)(\rho_{k+q}\cos\nu$$

$$+\frac{1}{2}(b_{-q-k}^\dagger + b_{k+q})\sin\nu)\big). \tag{A.5}$$

- Solving determinant of Eq. (3.5.2), we end with

$$\omega^4 - b\omega^2 + c = 0, \tag{A.6}$$

where

$$b = \varepsilon_{11}^2 + \varepsilon_{33}^2 + \varepsilon_{31}^2 + 2\varepsilon_{31}\varepsilon_{13} - 2\varepsilon_{14}\varepsilon_{32} - \varepsilon_{12}^2,$$

$$c = (\varepsilon_{11}\varepsilon_{33} - \varepsilon_{13}\varepsilon_{31})^2 - (\varepsilon_{12}\varepsilon_{33} + \varepsilon_{13}\varepsilon_{32})^2 - 2\varepsilon_{12}\varepsilon_{14}\varepsilon_{31}\varepsilon_{33} - 2\varepsilon_{11}\varepsilon_{14}\varepsilon_{32}\varepsilon_{33}$$

$$-2\big(\varepsilon_{11}\varepsilon_{14}\varepsilon_{34}\varepsilon_{31} + \varepsilon_{11}\varepsilon_{13}\varepsilon_{32}\varepsilon_{34} + \varepsilon_{12}\varepsilon_{13}\varepsilon_{34}\varepsilon_{31} + \varepsilon_{12}\varepsilon_{14}\varepsilon_{34}\varepsilon_{32}\big) - \varepsilon_{14}^2\varepsilon_{31}^2$$

$$-\varepsilon_{14}^2\varepsilon_{31}^2 - \varepsilon_{11}^2\varepsilon_{31}^2 + \varepsilon_{12}^2\varepsilon_{34}^2, \tag{A.7}$$

which give us the excitation energies, $\pm\omega_1$ and $\pm\omega_2$.

• The constant in Eq. (3.77) are

$$
\begin{aligned}
A =& \varepsilon_{11}, \\
B =& -\left(\varepsilon_{33}^2 - \varepsilon_{34}^2 + \varepsilon_{14}\varepsilon_{32} + \varepsilon_{13}\varepsilon_{31}\right), \\
C =& -\left(\varepsilon_{14}\varepsilon_{32} + \varepsilon_{11}\varepsilon_{33} - \varepsilon_{13}\varepsilon_{31}\right)\varepsilon_{33} + \varepsilon_{14}\varepsilon_{34}\varepsilon_{31} + \varepsilon_{13}\varepsilon_{32}\varepsilon_{34} + \varepsilon_{11}\varepsilon_{34}^2.
\end{aligned}
\tag{A.8}
$$

Γ's coefficients are

$$
\begin{aligned}
\Gamma_1 =& \frac{A_1 + B_1}{detT}, \quad \Gamma_2 = \frac{A_1 - B_1}{detT}, \\
\Gamma_3 =& \frac{A_2 + B_2}{detT}, \quad \Gamma_4 = \frac{A_2 - B_2}{detT}.
\end{aligned}
\tag{A.9}
$$

Where

$$
\begin{aligned}
A_1 =& 2\omega_1^5\omega_2 + 2\omega_1^3\omega_2^3 - 2B\omega_1\omega_2^3 + 2B\omega_1^3\omega_2, \\
B_1 =& 2A\omega_1^4\omega_2 + 2C\omega_1^2\omega_2 - 2A\omega_1^2\omega_2^3 - 2C\omega_2^3, \\
A_2 =& -2B\omega_1^3\omega_2 + 2B\omega_1\omega_2^3 - 2\omega_1^3\omega_2^3 + 2\omega_1\omega_2^5, \\
B_2 =& -2A\omega_1^3\omega_2^2 - 2C\omega_1^3 - 2C\omega_1\omega_2^2 + 2A\omega_1\omega_2^4, \\
detT =& 4\left(\omega_1^5\omega_2 + 2\omega_1\omega_2^5 - 8\omega_1^3\omega_2^3\right).
\end{aligned}
\tag{A.10}
$$

Bibliography

[1] S. W. Cheong and M. Mostovoy. Multiferroics: a magnetic twist for ferroelectricity. *Nat. Mater.*, 6:13–20, 2007.

[2] R. Ramesh and N. A. Spaldin. Multiferroics: progress and prospects in thin films. *Nat. Mater.*, 6:21–29, 2007.

[3] URL `http://apps.webofknowledge.com/`.

[4] J. Valasek. Piezoelectric and allied phenomena in rochelle salt. *Phys. Rev.*, 17: 475–481, 1921.

[5] G. Busch and P. Scherrer. Eine neue seignette-elektrische substanz. *Naturwissenschaften*, 23:737–737, 1935.

[6] H. Mueller. Properties of rochelle salt. *Phys. Rev.*, 47:175–191, 1935.

[7] H. Mueller. Properties of rochelle salt ii. *Phys. Rev.*, 57:829–839, 1940.

[8] H. Mueller. Properties of rochelle salt. iii. *Phys. Rev.*, 58:565–573, 1940.

[9] H. Mueller. Properties of rochelle salt. iv. *Phys. Rev.*, 58:805–811, 1940.

[10] J. C. Slater. Theory of the transition of KH_2PO_4. *J. Chem. Phys.*, 9:16–33, 1941.

[11] B. M. Wul and I. M. Goldman. Dielectric constants of titanates of metals of the second group. *Dokl. Akad. Nauk SSSR*, 46:154–157, 1945.

[12] A. F. Devonshire. Theory of banum titanate. *Philosophical Magazine*, 40:1040–1063, 1949.

[13] W. Cochran. Crystal stability and the theory of ferroelectricity. *Phys. Rev. Lett.*, 3:412–414, 1959.

[14] P. W. Anderson. Proceedings of the conference on the physics of dielectric. *Academy of Science, USSR, Moscow*, page 290, 1958.

[15] N. Setter, D. Damjanovic, L. Eng, G. Fox, S. Gevorgian, S. Hong, A. Kingon, H. Kohlstedt, N. Y. Park, G. B. Stephenson, I. Stolitchnov, A. K. Taganstev, D. V. Taylorv, T. Yamada, and S. Streiffer. Ferroelectric thin films: Review of materials, properties, and applications. *J. Appl. Phys.*, 100:051606, 2006.

[16] M. E. Lines and A. Glass. *Principles and Applications of Ferroelectrics and Related Materials*. Clarendon Press, Oxford, 2004.

[17] D. Damjanovic. Ferroelectric, dielectric and piezoelectric properties of ferro-electric thin films and ceramics. *Rep. Prog. Phys.*, 61:1267–1324, 1998.

[18] Y. Xu. *Ferroelectric Materials and Their Applications (Amsterdam: North-Holland).* North Holland, 1991.

[19] K. Uchino. *Ferroelectric devices.* New York : Marcel Dekker, 2000.

[20] B. A. Strukov and A. P. Levanyuk. *Ferroelectric Phenomena in Crystals: Physical Foundations.* Springer, 1998.

[21] K.M. Nair, H. Yanagida, and I. K. Lloyd. *Ferroic Materials: Design, Preparation, and Characteristics.* Amer Ceramic Society, 1994.

[22] G. Shirane, J. D. Axe, L. Harada, and J. P. Remeika. Soft ferroelectric modes in lead titanate. *Phys. Rev. B*, 2:155–159, Jul 1970.

[23] I. S. Zheludev. *Physics of crystalline dielectrics.* Plenum Press (New York), 1971.

[24] W. Zhong, X. Yu, H. Luo, Z. Cheng, and S. Hua. Growth units and forming mechanism of KDP crystals. *Science in China Series E: Technological Sciences*, 41:586–591, 1998.

[25] P. G. de Gennes. Collective motions of hydrogen bonds. *Solid State Commun*, 1:132–137, 1963.

[26] R. Blinc and B. Zeks. Dynamics of order-disorder-type ferroelectrics and anti-ferroelectrics. *Adv. Phys.*, 21:693–757, 1972.

[27] R. Pirc and R. Blinc. Off-center Ti model of barium titanate. *Phys. Rev. B*, 70:134107, 2004.

[28] H. X. Cao and Z. Y. Li. Thermodynamic properties of temperature graded ferroelectric film. *J. Phys.: Condens. Matter*, 15(36):6301, 2003.

[29] R. Blinc and B. Zeks. *Soft Modes in Ferroelectrics and Antiferroelectrics.* North-Holland, Amsterdam, 1974.

[30] J. M. Wesselinowa and M. S. Marinov. On the theory of first-order phase transition in order-disorder ferroelectrics. *Int. J. Mod. Phys. B*, 6:1181–1192, 1992.

[31] J. M. Wesselinowa. Properties of ferroelectric thin films with a first-order phase transitions. *Solid State Commun.*, 121:89–92, 2002.

[32] R. B. Stinchcombe. Ising model in a transverse field : I. basic theory. *J. Phys. C: Solid State Phys.*, 6:2459–2483, 1973.

[33] L. Onsager. Crystal statistics. i. a two-dimensional model with an order-disorder transition. *Phys. Rev.*, 65:117–149, 1944.

[34] St. Ducharme, V. M. Fridkin, A. V. Bune, S. P. Palto, L. M. Blinov, N. N. Petukhova, and S. G. Yudin. Intrinsic ferroelectric coercive field. *Phys. Rev. Lett.*, 84:175–178, 2000.

[35] A. Gruverman and A. Kholkin. Nanoscale ferroelectrics: processing, characterization and future trends. *Rep. Prog. Phys*, 69:2443–2474, 2006.

[36] M. Nakamura, Y. Tokunaga, M. Kawasaki, and Y. Tokura. Multiferroicity in an orthorhombic YMnO$_3$ single-crystal film. *Appl. Phys. Lett*, 98:082902, 2011.

[37] H. Kramers. Linteraction entre les atomes magntognes dans un cristal paramagntique. *Physica*, 1:182–192, 1934.

[38] J. Kanamori. Superexchange interaction and symmetry properties of electron orbitals. *J. Phys. Chem. Solids*, 10:87–98, 1959.

[39] J. B. Goodenough and A. L. Loeb. Theory of ionic ordering, crystal distortion, and magnetic exchange due to covalent forces in spinels. *Phys. Rev.*, 98:391–408, 1955.

[40] M. Fechner. *Magnetoelectric coupling at multiferroic interfaces.* PhD thesis, Martin-Luther-University Halle-Wittenberg, 2010.

[41] C. Zener. Interaction between the d-shells in the transition metals ii. ferromagnetic compounds of manganese with perovskite structure. *Phys. Rev.*, 82: 403–405, 1951.

[42] R. Skomski. *Simple Models of Magnetism.* Oxford University Press, 2008.

[43] S. V. Tyablikov. *Methods in the quantum theory of magnetism.* plenum press. Newyork, 1967.

[44] W. Nolting. *Fundamentals of Many-body Physics: Principles and Methods.* Springer, 2009.

[45] I. A. Sergienko and E. Dagotto. Role of the dzyaloshinskii-moriya interaction in multiferroic perovskites. *Phys. Rev. B*, 73:094434–094439, Mar 2006.

[46] C. Jia and J. Berakdar. Dynamical magnetoelectric effects induced by the dzyaloshinskii-moriya interaction in multiferroics. *EPL*, 85:57004 (pp 5), 2009.

[47] J. Stöhr and H.C. Siegmann. *Magnetism From Fundamentals to Nanoscale Dynamics.* Springer-Verlag Berlin Heidelberg, 2006.

[48] P. Curie. First consideration of an intrinsic correlation of magnetic and electric properties in a solid. *J. de Physique(3rd series)*, 3:393–415, 1894.

[49] G. A. Srnolensky and V. A. Ioffe. Colloque international de magnitisme de grenoble. In *Abstract Book, Contribution No. 71*, 2-6 July 1958.

[50] G. A. Smolensky, A. I. Agranovskaya, and V. A. Isupov. New ferroelectrics of complex composition. iii Pb_2MgWO_6, $Pb_3Fe_2WO_9$ and Pb_2FeTaO_6. *Sov.Phys.-Solid State*, 1:907–908, 1959.

[51] E. Ascher, H. Schmid H. Rieder, and H. Stossel. Some properties of ferromagnetoelectric nickel iodine boracite $Ni_3B_7O_{13}$. *J. Appl. Phys.*, 37:1404–1405, 1966.

[52] N. A. Hill. Why are there so few magnetic ferroelectrics. *J. Phys. Chem. B*, 104:6694–6709, 2000.

[53] T. Kimura, T. Goto, H. Shintani, K. Ishizaka, T. Arima, and Y. Tokura. Magnetic control of ferroelectric polarization. *Nature*, 426:55–58, 2003.

[54] B. B. van Aken, T. T. M. Palstra, A. Filippetti, and N. A. Spaldin. The origin of ferroelectricity in magnetoelectric $YMnO_3$. *Nat. Mater.*, 3:164–170, 2004.

[55] N. Hur, S. Park, P. A. Sharma, J. S. Ahn, S. Guha, and S. W. Cheong. Electric polarization reversal and memory in a multiferroic material induced by magnetic fields. *Nature*, 429:392–395, 2004.

[56] G. Lawes, A. B. Harris, and T. Kimura et al. Magnetically driven ferroelectric order in $Ni_3V_2O_8$. *Phys. Rev. Lett.*, 95:1–4, 2005.

[57] L. W. Martin, S. P. Crane, Y. H Chu, M. B Holcomb, M. Gajek, M. Huijben, C. H Yang, N. Balke, and R. Ramesh. Multiferroics and magnetoelectrics: thin films and nanostructures. *J. Phys.: Condens. Matter*, 20:434220–434233, 2008.

[58] H. Schmid. Multiferroic magnetoelectrics. *Ferroelecrrics*, 162:317–338, 1994.

[59] K. F. Wang, J. M. Liu, and Z. F. Ren. Multiferroicity: the coupling between magnetic and polarization orders. *Advances in Physics*, 58:321–448, 2009.

[60] I. E. Dzyaloshinskii. On the magneto-electrical effect in antiferromagnets [english transl.: Sov. phys. jetp 10 (1960) 628–629]. *J. Exptl. Theoret. Phys. (USSR)*, 37:881–882, 1959.

[61] D. N. Astrov. The magnetoelectric effect in antiferromagnetics. *Sov. Phys. Jetp*, 11:708–709, 1960.

[62] W. Eerenstein, N. D. Mathur, and J. Scott. Multiferroic and magnetoelectric materials. *Nature*, 44:759–765, 2006.

[63] H. Schmid. On a magnetoelectric classification of materials. *Int. J. Magn.*, 4: 337–361, 1974.

[64] H. Schmid. Some symmetry aspects of ferroics and single phase multiferroic. *J. Phys.: Condens. Matter*, 20:434201, 2008.

[65] D. Khomskii. Classifying multiferroics: Mechanisms and effects. *Physics*, 2:20, 2009.

[66] J. Van Den Brink and D. Khomskii. Multiferroicity due to charge ordering. *J. Phys.: Condens. Matter*, 20:434217, 2008.

[67] H. Katsura, N. Nagaosa, and A. V. Balatsky. Spin current and magnetoelectric effect in noncollinear magnets. *Phys. Rev. Lett.*, 95:057205–057209, 2005.

[68] M. Mostovoy. Ferroelectricity in spiral magnets. *Phys. Rev. Lett.*, 96:067601–067605, 2006.

[69] V. G. Baryachtar, V. A Lvov, and D. A. Jablonskii. Theory of inhomogeneous magnetoelectric effect. *JETP Lett.*, 37:673, 1983.

[70] S. V. Tjablikov. *Methods in the Quantum Theory of Magnetism*. Plenum Press, New York, 1967.

[71] D. N. Zubarev. Double-time green functions in statistical physics. *Usp. Fiz. Nauk*, 71:71–116, 1960.

[72] T. Kimura, S. Kawamoto, I. Yamada, M. Azuma, M. Takano, and Y. Tokura. Magnetocapacitance effect in multiferroic $BiMnO_3$. *Phys. Rev. B*, 67:180401, 2003.

[73] T.-J. Park, G. C. Papaefthymiou, A. J. Viescas, A. R. Moodenbaugh, and S. S. Wong. Size-dependent magnetic properties of single-crystalline multiferroic $BiFeO_3$ nanoparticles. *Nano Lett.*, 7:766772, 2007.

[74] T. Katsufuji, S. Mori, M. Masaki, Y. Moritomo, N. Yamamoto, and H. Takagi. Dielectric and magnetic anomalies and spin frustration in hexagonal $RMnO_3$, $(R = Y, Yb, Lu)$. *Phys. Rev. B*, 64:104419, 2001.

[75] Yu. Tserkovnikov. Decoupling of chains of equations for two-time green's functions. *Theor. Math. Phys.*, 7:250, 1971.

[76] W. Nolting and A. Ramakanth. *Quantum Theory of Magnetism*. Springer, 2009.

[77] H. B. Callen. Green's function theory of ferromagnetism. *Phys. Rev.*, 130:890–898, 1963.

[78] K. Taniguchi, N. Abe, T. Takenobu, Y. Iwasa, and T. Arima. Ferroelectric polarization flop in a frustrated magnet $MnWO_4$ induced by a magnetic field. *Phys. Rev. Lett.*, 97:097203, 2006.

[79] C. Wang, G.-C. Guo, and L. He. Ferroelectricity driven by the noncentrosymmetric magnetic ordering in multiferroic $TbMn_2O_5$: A first-principles study. *Phys. Rev. Lett.*, 99:177202, 2007.

[80] G. R. Blake, L. C. Chapon, P. G. Radaelli, S. Park, N. Hur, S-W. Cheong, and J. Rodriguez-Carvajal. Spin structure and magnetic frustration in multiferroic RMn_2O_5, $(R=Tb, Ho, Dy)$. *Phys. Rev. B*, 71:214402–214411, 2005.

[81] L. C. Chapon, G. R. Blake, M. J. Gutmann, S. Park, N. Hur, P. G. Radaelli, and S-W. Cheong. Structural anomalies and multiferroic behavior in magnetically frustrated TbMn$_2$O$_5$. *Phys. Rev. Lett.*, 93:177402, 2004.

[82] E.F. Bertaut, G. Buisson, A. Durif, J. Mareshal, M. C. Montmory, and S. Quezel-Ambrunaz. Combinaisons des oxydes de terres rares avec les oxydes des metaux de transition. *Bull. Soc. Chim. Fr.*, 65:132–1137, 1965.

[83] S. C. Abrahams and J. L. Bernstein. Crystal structure of paramagnetic DyMn$_2$O$_5$ at 298 K. *J. Chem. Phys.*, 46:3776–3783, 1967.

[84] A. Alonso, M. T. Casais, M. J. Martinez-Lope, J.L. Martinez, and M.T. Fernandez-Diaz. A structural study from neutron diffraction data and magnetic properties of RMn$_2$O$_5$ (R=La, rare earth). *J. Phys.: Condens. Matter*, 9: 8515–8526, 1997.

[85] Y. Noda, H. Kimura, Y. Kamada, T. Osawa, Y. Fukuda, Y. Ishikawa, S. Kobayashi, Y. Wakabayashi, H. Sawa, N. Ikeda, and K. Kohn. Relation between ferroelectric and antiferromagnetic order in RMn$_2$O$_5$. *Physica B: Condensed Matter*, 385-386:119–122, 2006.

[86] H. Kimura, S. Kobayashi, Y. Fukuda, T. Osawa, Y. Kamada, Y. Noda, I. Kagomiya, and K. Kohn. Spiral spin structure in the commensurate magnetic phase of multiferroic RMn$_2$O$_5$. *J. Phys. Soc. Jpn.*, 76(7):074706–074715, 2007.

[87] T. C. Ozawa and Sung J. Kang. Balls & sticks: Easy-to-use structure visualization and animation creating program. 37:679, 2004.

[88] J.-H. Kim, M. A. van der Vegte, A. Scaramucci, S. Artyukhin, J.-H. Chung, S. Park, S-W. Cheong, M. Mostovoy, and S.-H. Lee. Magnetic excitations in the low-temperature ferroelectric phase of multiferroic YMn$_2$O$_5$ using inelastic neutron scattering. *Phys. Rev. Lett.*, 107:097401, 2011.

[89] M. Mostovoy, A. Scaramucci, N. A. Spaldin, and K. T. Delaney. Temperature-dependent magnetoelectric effect from first principles. *Phys. Rev. Lett.*, 105: 087202, 2010.

[90] L. J. Chang, Y. Su, W. Schweika, Th. Brueckel, Y. Y. Chen, D. S. Jang, and R. S. Liu. Neutron polarization analysis on the multiferroic TbMn$_2$O$_5$. *Physica B*, 404:2517, 2009.

[91] T. Kimura, S. Ishihara, H. Shintani, T. Arima, K. T. Takahashi, K. Ishizaka, and Y. Tokura. Distorted perovskite with e_g^1 configuration as a frustrated spin system. *Phys. Rev. B*, 68:060403, 2003.

[92] J. Hemberger, F. Schrettle, A. Pimenov, P. Lunkenheimer, V. Yu. Ivanov, A. A. Mukhin, A. M. Balbashov, and A. Loidl. Multiferroic phases of Eu$_{1-x}$Y$_x$MnO$_3$. *Phys. Rev. B*, 75:035118, 2007.

[93] C. L. Lu, J. Fan, H. M. Liu, K. Xia, K. F. Wang, P. W. Wang, Q. Y. He, D. P. Yu, and J.-M. Liu. An investigation on magnetism, spin-phonon coupling, and ferroelectricity in multiferroic $GdMn_2O_5$. *Appl. Phys. A*, 96:991, 2009.

[94] N. Hur, S. Park, P. A. Sharma, S. Guha, and S-W. Cheong. Colossal magnetodielectric effects in $DyMn_2O_5$. *Phys. Rev. Lett.*, 93:107207, 2004.

[95] M. Fukunaga, Y. Sakamoto, H. Kimura, Y. Noda, N. Abe, K. Taniguchi, T. Arima, S. Wakimoto, M. Takeda, K. Kakurai, and K. Kohn. Magnetic-field-induced polarization flop in multiferroic $TmMn_2O_5$. *Phys. Rev. Lett.*, 103: 077204, 2009.

[96] R. P. Chaudhury, B. Lorenz, Y. Q. Wang, Y. Y. Sun, and C. W. Chu. Suppression and recovery of the ferroelectric phase in multiferroic $MnWO_4$. *Phys. Rev. B*, 77:104406, Mar 2008.

[97] I. Fina, L. Fabrega, F. Marti, X. abd Sanchez, and J. Fontcuberta. Magnetic switch of polarization in epitaxial orthorhombic $YMnO_3$ thin films. *Appl. Phys. Lett.*, 97:232905, 2010.

[98] C. Wang, G.-C. Guo, and L. He. First-principles study of the lattice and electronic structure of $TbMn_2O_5$. *Phys. Rev. B*, 77:134113, 2008.

[99] C. R. dela Cruz, R. Yen, B. Lorenz, S. Park, S.-W. Cheong, M. M. Gospodinov, W. Ratcliff, J. W. Lynn, and C. W. Chu. Evidence for strong spin-lattice coupling in multiferroic RMn_2O_5 via thermal expansion anomalies. *J. Appl. Phys.*, 99:08R103, 2006.

[100] B. Mihailova, M. M. Gospodinov, B. Güttler, F. Yen, A. P. Litvinchuk, and M. N. Iliev. Temperature-dependent Raman spectra of $HoMn_2O_5$ and $TbMn_2O_5$. *Phys. Rev. B*, 71:172301, 2005.

[101] R. Valdes Aguilar, A. B. Sushkov, S. Park, S.-W. Cheong, and H. D. Drew. Infrared phonon signatures of multiferroicity in $TbMn_2O_5$. *Phys. Rev. B*, 74: 184404, 2006.

[102] A. F. Garcia-Flores, E. Granado, H. Martinho, R. R. Urbano, C. Rettori, E. I. Golovenchits, V. A. Sanina, S. B. Oseroff, S. Park, and S.-W Cheong. Anomalous phonon shifts in the paramagnetic phase of multiferroic RMn_2O_5 (R = Bi, Dy, Eu): Possible manifestations of unconventional magnetic correlations. *Phys. Rev. B*, 73:104411, 2006.

[103] E. Garcia-Flores, A. F. Granado, H. Martinho, C. Rettori, E. I. Golovenchits, V. A. Sanina, S. B. Oseroff, S. Park, and S.-W. Cheong. Magnetically frustrated behavior in multiferroics RMn_2O_5 (R = Bi, Dy, Eu): A Raman scattering study. *J. Appl. Phys.*, 101:09M106, 2007.

[104] J. Cao, L. I. Vergara, J. L. Musfeldt, A. P. Litvinchuk, Y. J. Wang, S. Park, and S.-W. Cheong. Magnetoelastic coupling in $DyMn_2O_5$ via infrared spectroscopy. *Phys. Rev. B*, 78:064307, 2008.

[105] L. Martin-Carron, A. de Andres, M. J. Martinez-Lopez, M. T. Casais, and J. A. Alonso. Raman phonons and light scattering in $RMnO_3$ (R = La, Pr, Nd, Ho, Er, Tb and Y) orthorhombic and hexagonal manganites. *J. Alloys Compounds*, 323/324:494–497, 2001.

[106] A. B. Sushkov, R. Valdés Aguilar, S. Park, S-W. Cheong, and H. D. Drew. Electromagnons in multiferroic YMn_2O_5 and $TbMn_2O_5$. *Phys. Rev. Lett.*, 98: 027202, 2007.

[107] K. Cao, G.-C. Guo, and L. He. Molecular-spin dynamics study of electromagnons in multiferroic RMn_2O_5. *J. Phys.: Condens. Matter*, 24:206001, 2012.

[108] A. P. Litvinchuk. Lattice dynamics and spin-phonon interactions in multiferroic : Shell model calculations. *J. Magn. Magn. Mater.*, 321:2373–2377, 2009.

[109] J. Chenglong and J. Berakdar. Coupled spin-phonon excitations in helical multiferroics. *phys. stat. sol. (b)*, 247:662, 2010.

[110] M. Mochizuki, N. Furukawa, and N. Nagaosa. Theory of spin-phonon coupling in multiferroic manganese perovskites $RMnO_3$. *Phys. Rev. B*, 84:144409, 2011.

[111] J. M. Wesselinowa and St. Kovachev. Hardening and softening of soft phonon modes in ferroelectric thin films. *Phys. Rev. B*, 75:045411, 2007.

[112] I. Apostolova, A. T. Apostolov, and J. M. Wesselinowa. Theoretical study of the phonon spectra of multiferroic $BiFeO_3$ nanoparticles. *J. Phys.: Condens. Matter*, 21:036002, 2009.

[113] D. H Kim, N. Lee, M. Varela, and H. M. Christen. Antiferroelectricity in multiferroic $BiCrO_3$ epitaxial films. *Appl. Phys. Lett.*, 89:162904, 2006.

[114] S. G. Bahoosh, J. M. Wesselinowa, and S Trimper. Microscopic approach to the magnetoelectric effect in RMn_2O_5. *phys. stat. sol. (b)*, 2013.

[115] P. A. Sharma, J. S. Ahn, N. Hur, S. Park, Sung Baek Kim, Seongsu Lee, J.-G. Park, S. Guha, and S-W. Cheong. Thermal conductivity of geometrically frustrated, ferroelectric $YMnO_3$: Extraordinary spin-phonon interactions. *Phys. Rev. Lett.*, 93:177202, 2004.

[116] I. A. Sergienko, S. Cengiz, and E. Dagotto. Ferroelectricity in the magnetic E-phase of orthorhombic perovskites. *Phys. Rev. Lett.*, 97:227204, 2006.

[117] I. Kagomiya, S. Matsumoto, K. Kohn, Y. Fukuda, T. Shoubu, H. Kimura, Y. Noda, and N. Ikeda. Lattice distortion at ferroelectric transition of YMn_2O_5. *Ferroelectrics*, 286:167, 2003.

[118] H. Barath, M. Kim, S. L. Cooper, P. Abbamonte, E. Fradkin, I. Mahns, M. Rübhausen, N. Aliouane, and D. N. Argyriou. Domain fluctuations near the field-induced incommensurate-commensurate phase transition of $TbMnO_3$. *Phys. Rev. B*, 78:134407, 2008.

[119] S.-W. Cheong. Ferroelectricity by a magnetic twist. *Proceedings LEES06 Tallinn*, page 62, 2006.

[120] S M. Feng, Y. S. Chai, J. L. Zhu, N. Manivannan, Y. S. Oh, L. J. Wang, Y. S. Yang, C. Q. Jin, and H. K. Kee. Determination of the intrinsic ferroelectric polarization in orthorhombic $HoMnO_3$. *New J. Phys.*, 12:0730006, 2010.

[121] Y. Noda, H. Kimura, M. Fukunaga, S. Kobayashi, I. Kagomiya, and K. Kohn. Magnetic and ferroelectric properties of multiferroic RMn_2O_5. *J. Phys.: Condens. Matter*, 20:434206, 2008.

[122] C. R. dela Cruz, B. Lorenz, Y. Y. Sun, Y. Wang, S. Park, S.-W. Cheong, M. M. Gospodinov, and C. W. Chu. Pressure-induced enhancement of ferroelectricity in multiferroic RMn_2O_5 (R = Tb, Dy, Ho). *Phys. Rev. B.*, 76:174106, 2007.

[123] C. R. dela Cruz, F. Yen, B. Lorenz, M. M. Gospodinov, C. W. Chu, W. Ratcliff, J. W. Lynn, S. Park, and S.-W. Cheong. Structural anomalies at the magnetic and ferroelectric transitions in RMn_2O_5 (R = Tb, Dy, Ho). *Phys. Rev. B*, 73: 100406, 2006.

[124] C. C. Chou, S. Taran, J. L. Her, C. P. Sun, C. L. Huang, H. Sakurai, A. A. Belik, E. Takayama-Muromachi, and H. D. Yang. Anomalous pressure effect on the magnetic ordering in multiferroic $BiMnO_3$. *Phys. Rev. B*, 78:092404, 2008.

[125] X. Shen, C. H. Xu, C. H. Li, Y. Zhang, Q. Zhao, H. X. Yang, Y Sun, J. Q. Li, C. Q. Jin, and R. C. Yu. Pressure effects on multiferroic $Lufe_2o_4$. *Appl. Phys. Lett.*, 96:102909, 2010.

[126] C. Wilkinson, F. Sinclair, P. Gardner, J. B. Forsyth, and B. M. R. Wanklyn. The antiferromagnetic structure of $DyMn_2O_5$ at 4.2k. *Journal of Physics C: Solid State Physics*, 14(11):1671, 1981.

[127] P. P. Gardner, C. Wilkinson, J. B. Forsyth, and B. M. Wanklyn. The magnetic structures of the rare-earth manganates$ErMn_2O_5$ and $TbMn_2O_5$. *Journal of Physics C: Solid State Physics*, 21(33):5653–5661, 1988.

[128] J. B. Goodenough. Theory of the role of covalence in the perovskite-type manganites $(La, M(II))MnO_3$. *Phys. Rev.*, 100:564–573, Oct 1955.

[129] D. Higashiyama, S. Miyasaka, N. Kida, T. Arima, and Y. Tokura. Control of the ferroelectric properties of $DyMn_2O_5$ by magnetic fields. *Phys. Rev. B*, 70: 174405–174412, 2004.

[130] S. Seki, Y. Yamasaki, M. Soda, M.Matsuura, K. Hirota, and Y. Tokura. Correlation between spin helicity and an electrical polarization vector in quantum-spin chain magnet $LiCu_2O_2$. *Phys. Rev. Lett.*, 100:127201 (pp 4), 2008.

[131] R. P. Chaudhury, C. R. dela Cruz, B. Lorenz, Y. Y. Sun, C. W. Chu, S. Park, and S-W. Cheong. Pressure-induced polarization reversal in multiferroic YMn_2O_5. *Phys. Rev. B*, 77:220104–220108, 2008.

[132] R. P. Chaudhury, F. Yen, C. R. dela Cruz, B. Lorenz, Y. Q. Wang, Y. Y. Sun, and C. W. Chu. Pressure-temperature phase diagram of multiferroic $Ni_3V_2O_8$. *Phys. Rev. B*, 75:012407–012411, 2007.

[133] S. Seki, Y. Yamasaki, Y. Shiomi, S. Iguchi, Y. Onose, and Y. Tokura. Impurity-doping-induced ferroelectricity in the frustrated antiferromagnet $CuFeO_2$. *Phys. Rev. B*, 75:100403, 2007.

[134] S. Kanetsuki, S. Mitsuda, T. Nakajima, D. Anazawa, H. A. Katori, and K. Prokes. Field-induced ferroelectric state in frustrated magnet $CuFe_{1-x}Al_xO_2$. *J. Phys: Condens Matter.*, 19:145244, 2007.

[135] Y. S. Song, J. H. Chung, J. M. S. Park, and Y. N-Choi. Stabilization of the elliptical spiral phase and the spin-flop transition in multiferroic $Mn_{1-x}Co_xWO_3$. *Phys. Rev. B*, 79:224415, Jun 2009.

[136] R. P. Chaudhury, F. Ye, J. A. Fernandez-Baca, B. Lorenz, Y. Q. Wang, Y.Y Sun, H. A. Mook, and C. W. Chu. Robust ferroelectric state in multiferroic $Mn_{1-x}Zn_xWO_4$. *Phys. Rev. B*, 83:014401–014407, Jan 2011.

[137] H. Sagayama, K. Taniguchi, N. Abe, T.-h. Arima, M. Soda, M. Matsuura, and K. Hirota. Correlation between ferroelectric polarization and sense of helical spin order in multiferroic $MnWO_4$. *Phys. Rev. B*, 77:220407, Jun 2008.

[138] G. Lautenschlaeger, H. Weitzel, T. Vogt, R. Hock, A. Boehm, M. Bonnet, and H. Fuess. Magnetic phase transitions of $MnWO_4$ studied by the use of neutron diffraction. *Phys. Rev. B*, 48:6087–6098, Sep 1993.

[139] L. Meddar, M. Josse, P. Deniard, C. La Gilles Andre, F. Damay, V. Petricek, S. Jobic, M. Whangbo, M. Maglione, and C. Payen. Effect of nonmagnetic substituentsMg and Zn on the phase competition in the multiferroic antiferromagnet $MnWO_4$. *Chem. Mater.*, 21:52035214, 2009.

[140] H. Kleykamp. Zur thermodynamik in den systemen $Fe-W, Fe-W-O$ und $Fe-W-C$. *J. Less-Common Metals*, 71:127–134, 1980.

[141] H. Weitzel. Magnetische struktur von $CoWO_4$, $NiWO_4$ und $CuWO_4$. *Solid State Commun.*, 8:2071–2072, 1970.

[142] K. Takagi, T. Oi, and T. Fukazawa. Growth of high purity $ZnWO_4$ single crystals. *J. Crystal Growth.*, 52:580–583, 1981.

[143] K. C. Liang, R. P. Chaudhury, B. Lorenz, Y. Q. Wang, Y. Y. Sun, and C. W. Chu. Multiferroic phase control in $MnWO_4$ doped with Fe, Co, and Zn: A comparative study. *Integrated Ferroelectrics: An International Journal*, 131:1: 47–55, 2011.

[144] C. Tian, C. Lee, H. Xiang, Y. Zhang, C. Payen, S. Jobic, and M.-H. Whangbo. Magnetic structure and ferroelectric polarization of $MnWO_4$ investigated by density functional calculations and classical spin analysis. *Phys. Rev. B*, 80: 104426, Sep 2009.

[145] I. V. Solovyev. Origin of multiferroicity in MnWO$_4$. *arXiv:1210.7879*, 2012.

[146] J. M. Wesselinowa and I. Georgiev. Theoretical study of static and dynamic properties of orthorhombic multiferroic substances. *phys. stat. sol. (b)*, 245: 16531660, 2008.

[147] Nicole A. Benedek and Craig J. Fennie. Hybrid improper ferroelectricity: A mechanism for controllable polarization-magnetization coupling. *Phys. Rev. Lett.*, 106:107204, Mar 2011.

[148] J. M. Wesselinowa and I. Apostolova. Size and anisotropy effects on static and dynamic properties of ferromagnetic nanoparticles. *J. Phys: Condens Matter*, 19(21):216208, 2007.

[149] N. P. Thuy and J. J. M. Franse. The magneto crystalline anisotropy of Y$_2$(Co$_x$Fe$_{1-x}$)$_{17}$. *J. Magn. Magn. Mater.*, 915:54–57, 1986.

[150] I. S. Tereshina, A. P. Tulyakov, S. A. Nikitin, G. A. Politova, and K. P. Skokov. Increase in the magnetostrictive susceptibility of Tb$_{0.3}$Dy$_{0.67}$Ho$_{0.03}$Fe$_{2-x}$Co$_x$ alloys upon substitution of cobalt for iron. *Phys. Solid State*, 49:315–319, 2007.

[151] M. Maczka, M. Ptak, K. Hermanowicz, A. Majchrowski, A. Pikul, and J. Hanuza. Lattice dynamics and temperature-dependent Raman and Infrared studies of multiferroic Mn$_{0.85}$Co$_{0.15}$WO$_4$ and Mn$_{0.97}$Fe$_{0.03}$WO$_4$ crystals. *Phys. Rev. B*, 83:174439, May 2011.

[152] M. Ptak, M. Maczka, K. Hermanowicz, A. Pikul, and J. Hanuza. Temperature-dependent Raman and IR studies of multiferroic MnWO$_4$ doped with Ni^{2+} ions. *Spectrochim. Acta A 86, 85 (2012).*, 86:8592, 2012.

[153] N. Fujimura, T. Ishida, T. Yoshimura, and T. Ito. Epitaxially grown YMnO$_3$ film: new candidate for nonvolatile memory devices. *Appl. Phys. Lett.*, 69: 1011–1013, 1996.

[154] J. Wang, J. B. Neaton, H. Zheng, V. Nagarajan, S. B. Ogale, B. Liu, D. Viehland, V. Vaithyanathan, D. G. Schlom, U. V. Waghmare, N. A. Spaldin, K. M. Rabe, M. Wuttig, and R. Ramesh. Epitaxial BiFeO$_3$ multiferroic thin film heterostructures. *Science*, 299:1719–1722, 2003.

[155] F. Zavaliche, H. Zheng, L. Mohaddes-Ardabili, SY. Yang, Q. Zhan, P. Shafer, E. Reilly, R. Chopdekar, Y. Jia, P. Wright, DG. Schlom, Y. Suzuki, and R. Ramesh. Electric field-induced magnetization switching in epitaxial columnar nanostructures. *Nano Lett.*, 5:1793–1796, 2005.

[156] J. M. Wesselinowa. On the theory of thin ferroelectric films. *phys. stat. sol. (b)*, 223:737–743, 2001.

[157] J. M. Wesselinowa, Th. Michael, and St. Trimper. *Handbook of Nanophysics, Vol.4. Nanoparticles and Quantum Dots*. Taylor&Francis, 2010.

[158] Th. Michael. *Analytical description of ferroelectric nanostructures and bulk systems with non-collinear magnetic order.* PhD thesis, Martin-Luther-University Halle-Wittenberg, 2010.

[159] M. Azuma, K. Takata, T. Saito, S. Ishwata, and M. Takano. Designed ferromagnetic, ferrolelectric Bi_2NiMnO_6. *J. Am. Chem. Soc.*, 127:8889, 2005.

[160] M. Sakai, A. Masumo, D. Kan, M. Hashisaka, K. Takata, M. Azuma, M. Takano, and Y. Shimakawa. Multiferroic thin film of Bi_2NiMnO_6 with ordered double-perovskite structure. *Appl. Phys. Lett.*, 90:072903, 2007.

[161] Y. Shimakawa, D. Kan, M. Kawai, M. Sakai, S. Inoue, M Azuma, S Kimura, and Osami Sakata. Direct observation of the b-site ordering multiferroic $BiNiMnO_6$. *Jpn. J. Appl. Phys.*, 46:L845, 2007.

[162] P. Padhan, P. LeClair, A. Gupta, and G. Srinivasan. Magnetodielectric response in epitaxial thin films of multiferroic Bi_2NiMnO_6. *J. Phys.: Condens. Matter*, 20:355003, 2008.

[163] R. Nechache, C. Harnagea, L.-P. Carignan, D. Menard, and A. Pignolet. Structure and properties of epitaxial thin films of Bi_2FeCrO_6: a multiferoic material postulated by ab-initio computaion. *Ferroelectrics*, 101:152–163, 2008.

[164] R. Nechache, C. Harnagea, L.-P. Carignan, D. Menard, and A. Pignolet. Epitaxial Bi_2FeCrO_6 multiferroic thin film. *Phil. Mag. Lett.*, 87:231–240, 2007.

[165] R. Nechache, L.-P. Carignan, L. Gunawana, G.A. Harnagea, C.and Botton, D. Menard, and A. Pignolet. Epitaxial thin films of multiferroic $Bi_2FeCrO_6$with b-site cationic order. *J. of Mater. Res.*, 22:2102–2110, 2007.

[166] M. Azuma Y. Shimakawa and N. Ichikawa. Multiferroic compounds with double-perovskite structures. *Materials*, 4:153–168, 2011.

[167] A. Ciucivara, B. Sahu, and L. Kleinman. Density functional study of multiferroic Bi_2NiMnO_6. *Phys. Rev. B*, 76:064412, 2007.

[168] S. Kumar, G. Giovannetti, J. van den Brink, and S. Picozzi. Theoretical prediction of multiferroicity in double perovskite Y_2NiMnO_6. *Phys. Rev. B*, 82: 134429, 2010.

[169] M. N. Iliev, P. Padhan, and A. Gupta. Temperature-dependent Raman study of multiferroic Bi_2NiMnO_6 thin films. *Phys. Rev. B*, 77:172303, 2008.

[170] S. Kamba, D. Nuzhnyy, R. Nechache, K. Závěta, D. Nižňanský, E. Šantavá, C. Harnagea, and A. Pignolet. Infrared and magnetic characterization of multiferroic Bi_2FeCrO_6 thin films over a broad temperature range. *Phys. Rev. B*, 77:104111, 2008.

[171] J. M. Wesselinowa and I. Apostolova. Theoretical study of multiferroic $BiFeO_3$ nanoparticles. *J. Appl. Phys.*, 104:084108, 2008.

[172] A. Bhattacharjee, O. Erikson, and B. Sanyal. Dielectric properties and spin-phonon coupling in multiferroic double perovskite Bi_2CoMnO_6. *arXiv:1001.0128v2*, 2010.

[173] Y. Du, Z. X. Cheng, X. L. Wang, P. Liu, and S. X. Dou. Magnetic and ferroelectric properties of multiferroic Bi_2NiMnO_6 nanoparticles. *J. Appl. Phys.*, 109:07B507, 2011.

[174] E. A. Eliseev, A. N. Morozovska, M. D. Glinchuk, and R. Blinc. Anion vacancy-driven magnetism in incipient ferroelectric $SrTiO_3$ and $KTaO_3$ nanoparticles. *J. Appl. Phys.*, 109:094105, 2011.

[175] Y. Zhang, J. Hu, E. Cao, L. Sun, and H. Qin. Vacancy induced magnetism in $SrTiO_3$. *J. Magn. Magn. Mater.*, 324:1770–1775, 2012.

[176] R. V. K. Mangalam, M. Chakrabrati, D. Sanyal, A. Chakrabati, and A. Sundaresan. Identifying defects in multiferroic nanocrystalline $BaTiO_3$ by positron annihilation techniques. *J. Phys.: Condens. Matter*, 21:445902, 2009.

[177] A. Sundaresan and C. N. R. Rao. Ferromagnetism as a universal feature of inorganic nanoparticles. *Nano Today*, 4:96–106, 2009.

[178] M. Wang, G. L. Tan, and Q. Zhang. Multiferroic properties of nanacrystalline $PbTiO_3$ ceramics. *J. Amer. Ceram. Soc.*, 93:2151, 2010.

[179] S. G. Bahoosh, S. Trimper, and J. M. Wesselinowa. Origin of ferromagnetism in $BiTiO_3$ nanoparticles. *Phys. Status Solidi (RRL)*, 5:382, 2011.

[180] V. Skoromets, S. Glinsek, V. Bovtun, M. Kempa, J. Petzelt, S. Kamba, B. Malic, M. Kosec, and P. Kuze. Ferroelectric phase transition in polycrystalline $KTaO_3$ thin film revealed by terahertz spectroscopy. *Appl. Phys. Lett.*, 99:052908, 2011.

[181] Y. Zhou, Y. Hu, H. Gu, and Y. Wang. Optical properties of octahedral $KTaO_3$ nanocrystalline. *Mater. Chem. Phys.*, 115:151, 2009.

[182] L. A. Kappers, K. L. Sweeney, L. E. Halliburton, and J. H. W. Liaw. Oxygen vacancies in lithium tantalate. *Phys. Rev. B*, 31:6792–6794, 1985.

[183] K. L. Sweeney and L. E. Halliburton. Oxygen vacancies in lithium niobate. *Appl. Phys. Lett.*, 43:336, 1983.

[184] P. Moetakef, J. R. Williams, D. G. Ouellette, A. Kajdos, D. Goldhaber-Gordon, S. J. Allen, and S. Stemmer. Carrier-controlled ferromagnetism in $SrTiO_3$. *arXiv: 1204.1081*, 2012.

[185] I. R. Shein and A. L. Ivanovskii. First principle prediction of vacancy-induced magnetism in non-magnetic perovskite $SrTiO_3$. *Phys. Lett. A*, 371:155, 2007.

[186] W. F. Zhang, Z. Yin, M. S. Zhang, Z. L. Du, and W. C. Chen. Roles of defects and grain sizes in photoluminescence of nanocrystalline SrTiO$_3$. *J. Phys.: Condens. Matter*, 11:5655, 1999.

[187] J. Junquera and P. Ghosez. Critical thickness for ferroelectricity in perovskite ultrathin films. *Nature*, 422:506–509, 2003.

[188] C. H. Ahn, K. M. Rabe, and J. M. Triscone. Ferroelectricity at the nanoscale: Local polarization in oxide thin films and heterostructures. *Science*, 303:488–491, 2004.

[189] D. Cao, M.-Q. Cai, W.-Y. Hung, P. Yu, and H.-T. Huang. Vacancy-induced magnetism in BaTiO$_3$(001) thin films based on density functional theory. *Phys. Chem. Chem. Phys.*, 13:4738, 2011.

[190] T. Shimada, Y. Uratani, and T. Kitamura. Vacancy-driven ferromagnetism in ferroelectric PbTiO$_3$. *Appl. Phys. Lett.*, 100:162901, 2012.

[191] S. Hao, G. Zhou, X. Wang, J. Wu, W. Duan, and B.-L. Gu. Spontaneous polarizations of ultrashort-period epitaxial KNbO$_3$/(KTaO$_3$)$_m$ superlattices: An ab initio investigation. *Appl. Phys. Lett.*, 86:232903, 2005.

[192] D. I. Khomskii. Multiferroics: Different ways to combine magnetism and ferroelectricity. *J. Magn. Magn. Mater.*, 306:1, 2006.

[193] C. Diaz-Moreno, R. Farias, A. Hurtado-Macias, J. Elizalde-Galindo, and J. Hernandez-Paz. Multiferroic response of nanocrystalline lithium niobate. *J. Appl. Phys.*, 111:07D907, 2012.

[194] I. W. Chen and X. H. Wang. Sintering dense nanocrystalline ceramics without final-stage grain growth. *Nature (London)*, 404:168, 2001.

[195] R. V. K. Mangalam, N. Ray, U. V. Waghmare, A. Sundarasan, and C. N. R. Rao. Multiferroic properties of nanocrystalline BaTiO$_3$. *Solid State Commun.*, 149:1, 2009.

[196] A. M. Stoneham, J. Gavartin, A. L. Shluger, A. V. Kimmel, R. D. Muoz, H. M. Ronnow, G. Aeppli, and J. Renner. Trapping, self-trapping and the polaron family. *J. Phys.: Condens. Matter*, 19:255208, 2007.

[197] A. Sundaresan and C. N. R. Rao. Implications and consequences of ferromagnetism universally exhibited by inorganic nanoparticles. *Solid State Commun.*, 149:1197–1200, 2009.

[198] A. Hadni and A. Thomas. High electric fields and surface layers in very thin single crystal plates of triglycine sulfate. *Ferroelectrics*, 59:221, 1984.

[199] A. Hadni and A. Thomas. The use of a regular distribution of minute pinholes for the epitaxial growth of an oriented thin film. *Thin Solid Films*, 81:247, 1981.

[200] J. F. Scott, H. M. Duiker, P. D. Belae, B. Pouligny, K. Dimmler, M. Darris, D. Butler, and S. Eaton. Properties of ceramic KNO$_3$ thin-film memories. *Physica B*, 150:160, 1988.

[201] J. F. Scott, Ming-sheng Zhang, R. Bruce Godfrey, C. Araujo, and L. McMillan. Raman spectroscopy of submicron KNO$_3$ films. *Phys. Rev. B*, 35:4044–4051, 1987.

[202] H. Liu, B. Cao, and C. O' Connor. Intrinsic magnetism in BaTiO$_3$ with magnetic transition element dopants (Co, Cr, Fe) synthesized by sol-precipitation method. *J. Appl. Phys.*, 109:07B516, 2011.

[203] N. V. Minh and D. T. T. Phuong. SrTi$_{1-x}$Fe$_x$O$_3$ nanoparticle: a study of structural, optical, impedance and magnetic properties. *J. Exp. Nanosc.*, 6: 226–237, 2011.

[204] J. Seidel, L. W. Martin, Q. He, Q. Zhan, Y.-H. Chu, A. Rother, M. E. Hawkridge, P. Maksymovych, P. Yu, M. Gajek, N. Balke, S. V. Kalinin, S. Gemming, F. Wang, G. Catalan, J. F. Scott, N. A. Spaldin, J. Orenstein, and R. Ramesh. Conduction at domain walls in oxide multiferroics. *Nat. Mater*, 2373:229–234, 2009.

[205] Y. Geng, N. Lee, Y. J. Choi, S.-W. Cheong, and W. Wu. Collective magnetism at multiferroic vortex domain walls. *Nano Lett.*, 12:6055–6059, 2012.

List of publications

1. Safa Golrokh Bahoosh, Steffen Trimper, and Julia M. Wesselinowa. *Origin of ferromagnetism in $BaTiO_3$ nanoparticles.* Physica Status Solidi RRL **5**, 382-384 (2011).

2. J. M. Wesselinowa, A. T. Apostolov, I. N. Apostolova and S. G. Bahoosh. *Critical exponents of multiferroic hexagonal $RMnO_3$.* Bulg. J. Phys. **38**, 420-425 (2011).

3. Safa Golrokh Bahoosh, Steffen Trimper, and Julia M. Wesselinowa. *The magnetoelectric effect and double-perovskite structure.* Physica Status Solidi B **249**, 1602-1606 (2012).

4. S. Trimper, S. G. Bahoosh and J. M. Wesselinowa. *Multiferroic Behavior of BTO Nanoparticles.* in Magnetic Particle Imaging, SPPHY 140, pp. 273-277, Eds. T. M. Buzug and J. Borgert, Springer-Verlag Berlin, Heidelberg (2012).

5. S. G. Bahoosh and J. M. Wesselinowa. *Ion doping effects in multiferroic $MnWO_4$.* J. Appl. Phys. **111**, 083906 (2012).

6. S. G. Bahoosh a, A. T. Apostolov, I. N. Apostolova, J. M. Wesselinowa. *Theory of phonon properties in doped and undoped CuO nanoparticles.* Physics Letters A **376**, 2252-2255 (2012).

7. S. G. Bahoosh and J. M. Wesselinowa. *The origin of magnetism in perovskite ferroelectric ABO_3 nanoparticles($A = K$, Li; $B = Ta$, Nb or $A = Ba$, Sr, Pb; $B = Ti$).* J. Appl. Phys. **112**, 053907 (2012).

8. Safa Golrokh Bahoosh, Steffen Trimper, and Julia M. Wesselinowa. *Critical behavior of multiferroic hexagonal $RMnO_3$.* Physica Status Solidi B **249**, 2227-2230 (2012).

9. S. G. Bahoosh and J. M. Wesselinowa. *Origin of the different multiferroism in $BiFeO_3$ and $GaFeO_3$* J. Appl. Phys. **113**, 063905 (2013).

10. Safa Golrokh Bahoosh, Julia M. Wesselinowa, and Steffen Trimper . *Phonon excitations and magnetoelectric coupling in multiferroic RMn_2O_5.* Eur. Phys. J. B **86**, 201 (2013).

11. Safa Golrokh Bahoosh, Julia M. Wesselinowa, and Steffen Trimper . *Microscopic approach to the magnetoelectric effect in RMn_2O_5.* Physica Status Solidi B **250**, 1816 (2013).

12. I. N. Apostolova, A. T. Apostolov, S. G. Bahoosh and J. M. Wesselinowa *Origin of ferromagnetism in transition metal doped $BaTiO_3$.* J. Appl. Phys. **113**, 203904 (2013).

13. I. N. Apostolova, A. T. Apostolov, S. G. Bahoosh and J. M. Wesselinowa *Multiferroism in the dielectric function of CuO.* Physica Status Solidi RRL **7**, 1001-1004 (2013).

14. I. N. Apostolova, A. T. Apostolov, S. G. Bahoosh and J. M. Wesselinowa *Room temperature ferromagnetism and phonon properties of TiO_2 nanoparticles.* J. Magn. Magn. Mater **353**, 99104 (2014).

15. S. G. Bahoosh, A. T. Apostolov , I. N. Apostolova , S. Trimper, Julia M. Wesselinowa *Theoretical study of the multiferroic properties in M-doped (M = Co, Cr, Mg) ZnO thin films.* Submitted to J. Magn. Magn. Mater.

Presentations and participation

Presentations:

1. DPG Spring Meeting, (13-18 March 2011): *Spin-Phonon Excitations in Multiferroics.* (Poster), Dresden, Germany.

2. DPG Spring Meeting, (25-30 March 2012): *Theoretical study of Magnetoelectric effects in Multiferroic RMn_2O_5.* (Talk), Berlin, Germany.

3. 505. WE-Heraeus-Seminar New Routes to Single-Phase Multiferroics, (23-25 April 2012):*Magnetoelectric effects in Manganese Oxide Multiferroics.* (Poster), Physikzentrum Bad Honnef, Germany.

4. DPG Spring Meeting, (10 - 15 March 2013): *The effect of ion doping on multiferroic $MnWO_4$.* (Talk), Regensburg, Germany.

5. 6th European School on Multiferroics (ESMF6), (21-26 July 2013):*The origin of magnetism in perovskite ferroelectric ABO_3 nanoparticles (A = K, Li; B = Ta, Nb or A = Ba, Sr, Pb; B = Ti).* (Poster), Wittenberg, Germany.

6. Hands-On Workshop: Density functional theory and beyond, (6-15 August 2013): *The magnetoelectric effect and phonon properties in double-perovskite structure.*,(Poster), (ICTP) Trieste, Italy.

7. Joint European Magnetic Symposia (JEMS 2013), (25-30 August 2013): *Multiferroicity in doped and undoped $BaTiO_3$ nanoparticles.*,(Poster), Rhodes, Greece

8. International Conference on Nanoscale Magnetism (ICNM-2013) (2-6 September 2013): *The theoretical study of multiferroism in $Zn_{1-x}M_xO$ thin films (M = Mg, Co, Cr)* . (Poster), Istanbul, Turkey.

9. Joint IMPRS/SFB Workshop on Nanoscience and -technology (30 September-2 October 2013): *Extended Heisenberg model for asymmetric zigzag structures, more realistic model for RMn_2O_5 multiferroics.* (Talk), Halle, Germany.

Participation:

1. European School on Multiferroics (ESMF2010),(26 September-1 October 2010) , L'Aquila-Italy.

Eidesstattliche Erklärung

Hiermit erkläre ich gemäß §5 Abs. 2b der Promotionsordnung der Naturwissenschaftlichen Fakultät II der Martin-Luther-Universität Halle-Wittenberg vom 13.06.2012, dass ich die vorliegende Arbeit selbständig und ohne fremde Hilfe verfasst, sowie keine anderen als die von mir angegebenen Quellen und Hilfsmittel verwendet und die den verwendeten Werken wörtlich oder inhaltlich entnommenen Stellen als solche kenntlich gemacht habe.

Weiterhin erkläre ich die Angaben wahrheitsgemäß gemacht und die vorliegende Dissertation in gleicher oder ähnlicher Form bisher bei keiner anderen wissenschaftlichen Einrichtung zur Erlangung des Doktorgrades eingereicht sowie keine vorherigen Promotionsversuche unternommen zu haben.

Halle(Saale), den 2. Juli 2013

Safa Golrokh Bahoosh

Acknowledgments

This dissertation would not have been possible without the guidance and the help of several individuals who in one way or another contributed and extended their valuable assistance in the preparation and completion of this study.

First and foremost, my sincere appreciation to my supervisor, Prof. Dr. Steffen Trimper, for continual guidance and assistance throughout my Ph.D duration. I owe my deepest gratitude to Prof. Dr. Julia Wesselinowa for her great help, invaluable advices, suggestions and encouragements I will never forget. I am extremely grateful to my colleagues Dr. Thomas Michael for the useful discussions and hints and Dr. Thomas Bose for much help with technical issues.

I am especially indebted to my parents, for their constant encouragement and unfailing support throughout my studies. I wish to express my gratitude to my adored family; brothers and sisters, for their understanding and endless love. Last but not the least, an honorable mention goes to all my friends who have made the last three years so enjoyable and people who have willingly helped me out with their abilities and along with god, have been 'my footprints in the sand'.

Curriculum Vitae

Personal information:

Last name:	Golrokh Bahoosh
First name:	Safa
Date of birth:	13.06.1983
Place of birth:	Sabzevar-Iran
Nationality:	Iranian
Gender:	Female
Address:	Max Planck Institute of Microstructure Physics, Weinberg 2, 06120-Halle, Germany
Telefone:	0049 345 5525437
Fax:	0049 345 5511223
Email:	sgolrokh@mpi-halle.mpg.de

Education:

1997-2001:	High School Diploma in Mathematics and Physics, Andishe Heighschool, Mashhad, Iran
2001-2005:	Bachelor of Science, Physics, Ferdowsi University of Mashhad, Mashhad, Iran
2006-2009:	Master of Science, Solid State Physics, Ferdowsi University of Mashhad, Mashhad, Iran
2010-2013:	Doctor rerum naturalium (Expected degree), International Max Planck Research School for Science and Technology of Nanostructures and Martin-Luther Universität Halle-Wittenberg, Halle, Germany

Halle (Saale), 2. July 2013